Improving the Performance of Halide Perovskite Thin Film through Pb(II)-Coordination Chemistry

利用铅(II)的配位化学原理改善钙钛矿薄膜的性能

Thesis submitted in accordance with the requirements of the University of Liverpool for the degree of Doctor in Philosophy

By

Tianhao YAN

Department of Chemistry

Xi'an Jiaotong-Liverpool University & University of Liverpool

August 2020

Abstract

Recently, organo-lead-halide perovskite solar cells have attracted growing and wide attention due to their remarkable photoelectric properties, low cost and ease of fabrication. However, the development of perovskite solar cells is still limited by several factors, such as strict fabrication conditions, low stability, small active area and poor reproducibility etc. The nature of perovskite film formation is argued as a process of a series of chemical reactions and crystallization processes, where the Pb(II) coordination chemistry involves in. We thus set out to improve the performance of perovskite films from the point of Pb(II) coordination chemistry.

By using the solvent engineering strategy, a series of inverted perovskite solar cells (PSCs) with a device structure as ITO/PEDOT: PSS/$CH_3NH_3PbI_{3-x}Cl_x$/PCBM/Al via one-step coating were fabricated had been successfully fabricated using simple one-step method from the solutions of chloric precursors in the mixtures of N, N-dimethylformamide (DMF) and γ-butyrolactone (GBL) at different ratios. The highest average PCE (power conversion efficiency) of 11.251 % was achieved when the solvent with DMF : GBL = 3.5 : 6.5 (v : v) was used for precursor preparation, while the average PCEs for the devices from precursors with pure GBL and DMF as the solvent were 8.600 % and 8.082 %, respectively. The detailed SEM (scanning electron microscope), XRD (X-ray Diffraction) and UV-Vis (UV-Visible spectroscopy) studies showed that the great increase of the PCE of the PSC was led by the apparent quality improvement of the perovskite film, owing to the fast nucleation and the slow crystal growth introduced by the dual solvent system. Plausible formation mechanisms of perovskite films from different solvents were proposed.

The film formation processes from different precursors were also studied, and several intermediates in the perovskite film formation processes were isolated and structurally

characterized. The single crystals were successfully grew and the crystal structures of $MAPbI_3 \cdot DMF$, $MAPbI_2Cl \cdot DMF$ and $MAPb_{1.5}I_3Br \cdot DMF$ were solved. The crystal structures of $MAPbI_2Cl \cdot DMF$ and $MAPb_{1.5}I_3Br \cdot DMF$ were identified for the first time. Meanwhile, the recrystallization process of $MAPbI_2Cl \cdot DMF$ were founded that happened before spin-coating or at the early stage of annealing was the key to produce the perovskite film with high crystallinity and high orientation from chloride precursors. Based on the structures and chemical properties of the intermediates, the version of chemical reactions and mechanisms for perovskite film formation with different precursors were proposed.

In addition, several groups of PSCs from lead acetate trihydrate-based precursors were constructed by varying hydrate number, finely tuning spin-coating method, and applying DMSO as additive. It was found that the H_2O molecules in precursors can greatly improve the film coverage, and the pre-heating method can avoid the low crystallinity while ensuring the high coverage of perovskite thin films. In addition, the adding of DMSO as additive influenced the formation kinetics of perovskite films and improved the reproducibility of devices. As a result, PSCs with PCE of 15.714 % had been achieved.

Keywords: solar cell, perovskite, coordination chemistry, lead (II), perovskite thin-films, perovskite solar cell, chloride precursors, solvent engineering, perovskite formation mechanisms, X-ray single crystal structure analysis

摘　　要

近年来，有机铅卤钙钛矿电池由于其优异的光电转换性能、低廉的成本、简单的生产工艺等优势受到世界范围内的广泛的关注。虽然钙钛矿电池发展迅速，但是其发展依然受到生产条件严格、稳定性差、电池尺寸小、以及可重复性低等因素的制约。我们认为，钙钛矿薄膜形成的本质是铅配位化合物的结晶与化学反应，对这一过程的了解与调控对提高钙钛矿太阳能电池的光电性能有决定性作用。因此，我们从配位化学原理与晶体工程入手，通过对钙钛矿活性层的结构以及形成机理的研究来寻找制备高效廉价钙钛矿太阳能电池的方法。我们的工作结果包括：

（1）利用 N，N-二甲基甲酰胺（DMF）及γ-丁内酯（GBL）两种常用溶剂的结构，极性，溶解性及对金属铅（II）配位能力的差异，从最简单的一步旋涂法入手，采用平面倒装的电池结构，通过溶剂工程改善钙钛矿电池的效率及可重复性。实验发现，使用的混合溶剂可使电池平均效率达到 11.556 %，相比于纯的 DMF 或 GBL 作溶剂（平均效率分别为 8.082 %和 8.600 %），溶剂工程显著地提高了电池效率，此外电池的重复性也有显著提高。

（2）在研究不同卤素钙钛矿的成膜过程中，通过晶体工程方法发现了 4 个个铅卤钙钛矿成膜过程中间体，并得到了其晶体结构和分子结构，其中 2 个化合物及结构属于首次发现。根据这些发现以及我们对成膜过程的深入观察和研究，在前人工作的基础上，我们提出了铅卤钙钛矿成膜过程的化学反应及结晶过程新机理。这些发现对提高钙钛矿成膜质量，改善电池的性能具有重要意义。

（3）使用乙酸铅三水合物作为前驱体溶液原料，采用平面倒装的电池结构，通过预热旋涂法及二甲亚砜（DMSO）的添加剂工程显著提高了钙钛矿电池的效率及可重复性。电池效率从传统一步法的 10.636 %提高到 14.816 %。

关键词：太阳能电池，钙钛矿，机理，中间体，溶剂工程，X 光单晶衍射，添加剂

Acknowledgements

First of all, I would like to express my heartfelt gratitude to my supervisor, Dr. Ruiyao Wang, for his kind and selfless supervision during my research career in XJTLU. Since the first day I joined Dr. Wang's group in 2013, Dr. Wang has kept leading me move forward to the right direction in both study and life. The professional knowledge and research skills that were taught by Dr. Wang will benefit me throughout my life.

Then, I would like to thank Dr. Changqi Ma, Dr. Qun Luo, Ms. Lianping Zhang, Mr. Jie Wang and other members from SINANO for their great help and support in my device fabrication and characterization works.

I also would like to give thanks to Dr. Haifei Zhang, Dr. Lifeng Ding, Dr. Li Yang, Dr. Yi Li, Dr. Yi Lin, Dr. Graham Dawson, Mr. Kun Zhan, Ms. Ruixue Zhou, Mr. Hao Zhou, Ms. Shuhui Tao and other staffs in department of chemistry for their great help.

At last, I would like to give thanks to my family members, especially my wife, for their strong and selfless support during my doctoral career.

List of publications

CONFERENCE PROCEEDINGS：

1. **Tianhao Yan** and Ruiyao Wang. Improving the Quality of Perovskite Thin Film, a Coordination Chemistry Approach. 2019 Forum on Marine Materials Chemistry, Zhuhai, Guangdong, China, December 08-10 2019.
2. **Tianhao Yan** and Ruiyao Wang. Study of Organolead Halide Perovskite Film Formation Mechanism from the View of Coordination Chemistry. *2018 Asia-Pacific Hybrid and Organic Photovoltaics Conference (AP-HOPV 2018)*, Kitakyushu, Japan, January 28-30, 2018.
3. **Tianhao Yan** and Ruiyao Wang, Application of Coordination Chemistry in the Study of Perovskite solar cells, The Third New Energy Forum, Wuhan, China, September 2017.
4. **Tianhao Yan**, Lianping Zhang, Qun Luo, Changqi Ma and Ruiyao Wang, Improving the Performance of Inorganic-Organic Hybrid Perovskite Solar Cells by Solvent Engineering, SPINS16, Berlin, Germany, September 2016.

PATENTS:

1. **Tianhao Yan** and Ruiyao Wang, Solvent and method and application for preparing high-performance metal halide perovskite film. Faming Zhuanli Shenqing (2019), CN 109920939 A 20190621.

List of figures

List of tables

List of acronyms

Terms	Initial components of the terms
1D	One-dimensional
2D	Two-dimensional
3D	Three-dimensional
DSSC	Dye-sensitized solar cell
J_{SC}	Short circuit current density
V_{oc}	Open circuit voltage
FF	Fill factor
PCE	Power conversion efficiency
PVSK	Perovskite
PSC	Perovskite solar cell
PEDOT : PSS	Poly(3,4-ethyl-enedioxythiophene) : poly(styrene sulfonate)
PCBM	[6,6]-phenyl-C61-butyric acid methyl ester
DMF	N,N-dimethylformamide
DMSO	Dimethyl sulfoxide
GBL	Gamma-butyrolactone
MAI	Methylamine iodide
$MAPbI_3$	Methylamine lead iodide
AFM	Atomic-force microscopy
NMR	Nuclear magnetic resonance
SEM	Scanning electron microscopy
HR-TEM	High-resolution transmission electron microscopy
FT-IR	Fourier transform infrared spectroscopy
UV-Vis	Ultraviolet and visible spectrophotometer
TGA	Thermogravimetric analysis
DTA	Differential thermal analysis
XPS	X-ray photoelectron spectroscopy
XRD	X-ray diffraction
XAS	X-ray absorption spectroscopy
XANES	X-ray absorption near edge structure

Table of contents

1 Research background

Energy shortage and environmental pollution have become major challenges to modern society. Fossil fuels provide more than 85% of global energy currently, and will continue to dominate global energy demand till 2030.[1, 2] However, fossil fuels such as coal and oil were limited and generated emissions that not only accelerate global warming, but also produced severe environment contamination.[1, 3] The unsustainable nature of fossil fuels determines the necessity of discovering the alternative energy sources. Therefore, people have arrived at a consensus on developing and utilizing cost-effective, environment-friendly, and sustainable energy sources. Sustainable energy is commonly defined as a type of resources that can be naturally replenished after consumption and exhaust no or few pollutants, such as hydraulic power, solar energy, wind power, and geothermal heat, etc. Solar energy is a type of prospective sustainable energy source that has been widely used by human beings since a long time ago. Generally, the radiant power of the sun is up to 3.6×10^{20} MW/s, and the amount of solar energy that deposits on the earth surface is approximately 1.05×10^{18} kWh per year, which is equivalent to 1.3×10^{15} tons of coal. In this context, the conversion of sunlight energy into chemical or electrical energy is currently viewed as one practical option.[2, 3]

Up to now, various strategies have been explored in an attempt to harvest solar energy, including photovoltaics, photoelectrochemical cells, and solar water splitting, etc.[4] Among these strategies, photovoltaics or solar cells have been considered as one of the most potential technology that can effectively generate electricity from sunlight, and meet the requirement of adequately utilizing solar energy.[5] Photovoltaics are the techniques that can convert solar light into a flow of electrons using semiconductors exhibiting photovoltaic effect. The photovoltaic effect was first demonstrated by French physicist Edmond Becquerel as early as 1839.[5] The first practical solar cells

were manufactured in 1954 at Bell Laboratories by Daryl Chapin, Calvin Fuller and Gerald Pearson.[5] These cells were constructed based on p-n junction of monocrystalline silicon, of which the efficiencies were about 6 %. Since then, significant development in photovoltaics has been made and large-scale manufacture of high efficiency solar cell with power conversion efficiency (PCE) of over 32.9 % has been realized.[6] Now the research of solar cells has been moving towards to diversification, high efficiency, low cost, and high stability.[2]

1.1 Fundamentals of solar cells

Solar cells, also known as photovoltaic devices, are a type of electrical devices that directly convert solar energy into electricity by the photovoltaic effect. When the heterogeneous semiconductors which are the combinations of p-type and n-type semiconductors absorb photons with suitable wavelengths, electric potential difference can be generated. This physical phenomenon is defined as photovoltaic effect.[7] The p-n junction is the basic working component that converts solar energy to electric energy of solar cells.[8, 9] A junction is an interface between different types of semiconductors. The closely contact of semiconductors can cause band bending due to the difference between Fermi levels, thus generates the junction.[9] According to the contacts between different types of semiconductor materials, p-n homojunction, p-n heterojunction, p-p homojunction, and n-n homojunction can be constructed.[7, 10] Today, the working principle of perovskite solar cells is widely accepted as the n-i-p and p-i-n types. Between p-type and n-type semiconductors, perovskite acts as an intrinsic absorber to generate electron-hole pairs when absorbing solar light. The working principle of perovskite solar cells is similar to those of solid-state p-n junction solar cells, which will be mainly discussed below.[1]

1.1.1 Principle of p-n junction

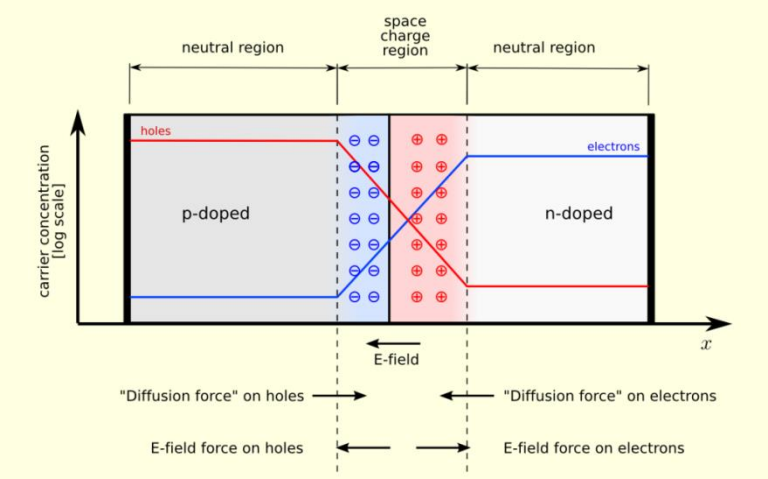

Figure 1.1.1. Schematic diagram of a p-n junction. https://commons.wikimedia.org/wiki/File:Pn-junction-equilibrium.png, (accessed November 2019).

The general working principle of p-n junction is indicated below, and the schematic diagram is shown in Figure 1.1.1:

i. Briefly, the p-n junction consists of three regions, neutral p-region (p-doped semiconductor), space charge region, and neutral n-region (n-doped semiconductor). In the p-region holes are in the majority, while in the n-region the dominating carriers are electrons. Thus, p-region has high electron concentration, and n-region has high hole concentration.
ii. Because the carrier concentrations are different, when the contact of atomic level happens between two types of semiconductors, charge carriers will diffuse. Specifically, electrons of n-region diffuse into p-region, while holes of p-region diffuse into n-region. As a result, nearby the p-n junction p-region and n-region will be negatively and positively charged respectively, which produces an inside electrical field with direction from n-region to p-region.
iii. Meanwhile, the electrical field will drive the carriers drift towards the opposite direction of diffusion. When the diffusion and drifting reach dynamic equilibrium, the value of electrostatic current via p-n junction equals to zero. In this state, in the space charge region holes from the p-region recombine with electrons of the n-region, and vice versa. Thus, few conducting carriers exist in this region, which is also known as depletion layer.[7]

The p-n junction in solar cells has no external applied voltage, but convert solar energy into electric energy and transport to external load. In the dark condition, the solar cell can be treated as an ideal diode, and the current inside can be described by the function:

$$I = I_s \left[e^{\frac{eV}{kT}} - 1 \right] \qquad \text{(Func. 1.1.1-1)}$$

Inside, e is electron charge, which equals to 1.6×10^{-19} C; k is Boltzmann constant,

which equals to 1.38×10^{-23} J/K; T is thermodynamic temperature; I_s is the reverse saturation current in ideal diode under dark condition, the function of which is:

$$I_s = AeN_C N_V \left[\frac{1}{N_A} \left(\frac{D_n}{\tau_n} \right)^{\frac{1}{2}} + \frac{1}{N_D} \left(\frac{D_p}{\tau_p} \right)^{\frac{1}{2}} \right] e^{-\frac{E_g}{kT}} \qquad \text{(Func. 1.1.1-2)}$$

Inside, A is the area of p-n junction; N_C and N_V is the state density of conduction band and valence band, respectively; N_A and N_D is the doping concentration of acceptor material and donor material, respectively; D_n and D_p is diffusion coefficient of electron and hole, respectively; τ_n and τ_p is the minority carrier lifetime of electron and hole, respectively; E_g is the bandgap of semiconductor.

Photovoltaic effects can be created from semiconductor-semiconductor junction, based on which junction solar cells can be constructed. When the solar cell based on p-n junction is exposed to sunlight, parts of electrons are excited to generate electron-hole pairs inside the junction. In the depletion layer, the inside electrical field drives electrons and holes moving towards to n-region and p-region, respectively. As a result, the light current I_L is produced in the reverse area. When the light current I_L flows through the external load, voltage drop will happen. The voltage drop here can make the p-n junction forward, and produces a forward current I_F whose direction is opposite with the light current I_L. Therefore, in the reverse condition, combining with the ideal diode function the net current through p-n junction can be expressed as:

$$\mathrm{I} = I_L - I_F = I_L - I_S \left[e^{\frac{eV}{kT}} - 1 \right] \qquad \text{(Func. 1.1.1-3)}$$

Generally, there are two extreme conditions in the working state of solar cells: one is short-circuit of p-n junction, and the other is open-circuit of p-n junction. When the p-n junction is short-circuited, the external load $R = 0$, thus the voltage drop $V = 0$ and the related $I_F = 0$. Now the current through p-n junction is called short-circuit current

I_{SC}, according to function 1.1.1-1:

$$I = I_{SC} = I_L \qquad \text{(Func. 1.1.1-4)}$$

Here, the current through the p-n junction equals to the light current I_L.

On the other side, when the p-n junction is open-circuited, through which the overall current is 0, the external load can be treated as infinity. The voltage here is called open-circuit voltage V_{OC}, which produces the forward current I_F and just offsets the light current I_L, so the function 1.1.1-1 changes to:

$$\mathrm{I} = 0 = I_L - I_s\left[e^{\frac{eV}{kT}} - 1\right] \qquad \text{(Func. 1.1.1-5)}$$

Transform the function 1.1.1-3 can get the function of V_{OC}:

$$V_{OC} = \frac{kT}{e}\ln\left(1 + \frac{I_L}{I_S}\right) \qquad \text{(Func. 1.1.1-6)}$$

1.1.2 Performance parameters of solar cells

The function 1.1.1-2 expresses the volt-ampere relationship of solar cells, of which the curve is called volt-ampere characteristic curve or *J*-*V* curve, which is used to characterize the performance of solar cells (shown in Figure 1.1.2).

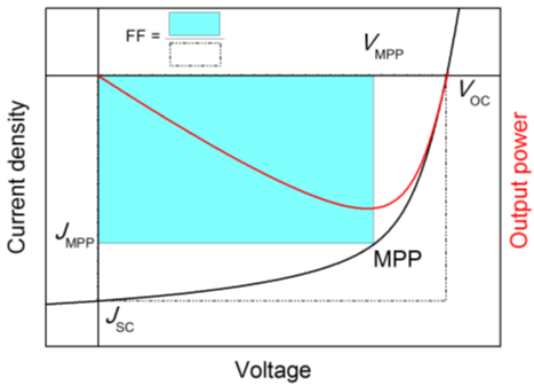

Figure 1.1.2. A diagram of a typical *J*-*V* curve.[11]

(1) Short circuit current density (J_{SC})

When short current happens between two electrodes of the solar cell, the voltage equals to zero, during which the current is named as I_{sc}. The I_{sc} is generated due to the creation and collection of photon-generated carriers, which equals to the light current I_L, and is the largest value that current can reach during the solar cell works. In the *J-V* curve, short circuit current density (J_{SC}) is always used instead of I_{SC}. The determinant of J_{SC} can be expressed as:

$$J_{SC} = q\int_{\lambda_{min}}^{\lambda_{max}} \phi_{in} EQE(E_g) dE_g \qquad \text{(Func. 1.1.2-1)}$$

where E_g is the bandgap of active layer material; *EQE*, also called as *IPCE* (monochromatic incident photon-to-electron conversion efficiency), is the external quantum efficiency; ϕ_{in} is the number of incident photons at a specific wavelength. According to the equation 1.1.2-1, the light-absorbing parameters of semiconductor can influence the value of J_{SC}, especially the bandgap and absorption coefficient. In addition, the value of J_{SC} is also influenced by incident light intensity, carrier generation rate, carrier diffusion length. A high J_{SC} represents efficient generation and transportation of carriers in the active layer.

(2) Open circuit voltage (V_{oc})

When no load is connected to a solar cell, the current of circuit is zero, in this moment the voltage between the two electrodes is defined as V_{oc}. The unit of V_{oc} is volt (V), and the value equals to the forward bias produced by photo-current between two sides of the solar cell. Based on the function 1.1.1-6, the value of V_{OC} is determined by the light current I_L and reverse saturation current I_S. Generally, the volatility of I_L is very small, while that of I_S is very large. The value of I_S is related with the recombination process in the solar cell, so the value of V_{OC} can represent the inside recombination condition of solar cell to a certain extent. Similar with J_{SC}, V_{OC} is also a function of bandgap:

$$V_{OC} = \frac{q}{k}\frac{15\sigma}{\pi^4}T^3\int_{\frac{E_g}{kT}}^{\infty}\frac{x^2}{e^x-1}dx \qquad \text{(Func. 1.1.2-2)}$$

Inside, k is Boltzmann constant; σ is Stefan-Boltzmann constant; T is thermodynamic temperature. Clearly, I_S can produce huge volatility with the variation of E_g, thus significantly influence the value of V_{OC}. Therefore, a high V_{oc} indicates the band structures of each layers in solar cell are compatible and the interlayers have few recombination.

(3) Series resistance (R_s) and shunt resistance (R_{sh})

In solar cell R_s is the sum of mainly volume resistance and surface resistance, and R_{sh} is a fictitious resistance caused by the internal defects. R_s and R_{sh} are typically calculated from the *J-V* characteristics. Briefly, large R_s reduces J_{SC}, while small R_{sh} reduces V_{OC}.

(4) Fill factor (FF)

FF is an important parameter that represents the output characteristic of solar cell. The value equals to the ratio of P_{max} (MPP) of solar cell to the product of J_{SC} and V_{OC}. The efficiency density of solar cell can be expressed as:

$$\mathrm{P}(V) = J(V) \times V \qquad \text{(Func. 1.1.2-3)}$$

When the first derivative of function 1.1.2-3 equals to 0, the theoretical FF reaches to the highest value. A high FF indicates the ability of solar cell that can output actual power closed to the theoretically value.

(5) Power conversion efficiency (PCE)

During the measurement of *J-V* characteristics, P_{in} is the incident light power, and P_{max} is the actual peak power of solar cell from measurement. PCE is defined as the

maximum power conversion efficiency of solar cell when the optimal load is connected to external circuit. The value equals to the percentage ratio of P_{max} (MPP) to P_{in}:

$$\mathrm{PCE} = \frac{P_{max}}{P_{in}} = \frac{J_{SC} \times V_{OC} \times FF}{P_{in}} \qquad \text{(Func. 1.1.2-4)}$$

PCE is a comprehensive assessment of photovoltaic devices in terms of performance and quality.

(6) Quantum efficiency (QE)

QE is the abbreviation of monochromatic incident photon-to-electron conversion efficiency of solar cell. QE equals to the ratio of excited electron-hole pairs to incident photons inside the solar cell under monochromatic light. External quantum efficiency (EQE) is the ratio of excited carriers generated in the solar cell to the photons of a particular wavelength that irradiate on the solar cell from outside. Internal quantum efficiency (IQE) means the ratio of excited carriers generated in the solar cell to the photons of a particular wavelength that irradiate on the solar cell from outside and are absorbed by the cell. The IQE of a solar device is inferred by combining its EQE with transmission and reflection data, which is always larger than the EQE. The EQE is always measured over a range of different wavelengths to indicate the condition of charge carrier recombination.

1.2 Major types of solar cells

1.2.1 Silicon-based solar cells

Among all the silicon-based solar cells, monocrystalline (mono-Si) silicon solar cell has the highest PCE (~ 15%) and the most mature producing technology. Such high performance is depended on the mono-Si of high quality and sophisticated hot-working treatment. The high efficiency of mono-Si solar cell is undoubted, which still dominates the large-scale production and application. However, due to the high price of mono-Si and the complex producing process, the cost of mono-Si solar cell is high steadily. Thus, thin film solar cells are developed as substitutes of mono-Si solar cell, which mainly include multicrystalline silicon (multi-Si) and amorphous silicon (a-Si) thin film solar cells.[4-6]

The a-Si thin film solar cell is low cost and mass produced, which has received attention and been developed rapidly. The PCE of a-Si thin film solar cell has reached 8-10 %. Nevertheless, the bandgap of a-Si material is 1.7 eV, which limits the absorption range and the PCE. Moreover, the PCE of a-Si solar cell will decrease with illumination time gradually because of the light-induced degeneration, which makes the cell unstable. Multi-Si thin film solar cell is the next-generation cell with advantages of high PCE (10-12 %), long lifetime, and relatively simple producing technology. Thin film crystalline silicon is applied as active layer in the multi-Si solar cell. Furthermore, the multi-Si solar cell consumes much fewer silicon materials than the mono-Si solar cell, has no light-induced degeneration, and can be constructed on substrate material. Therefore, the multi-Si thin film solar cell has not only higher efficiency and stability than a-Si thin film solar cell, but also lower producing cost than mono-Si solar cell.[4-6]

1.2.2 Hetero-inorganic semiconductor solar cells

Multiple-inorganic semiconductor materials mainly includes III-V groups compounds such as gallium arsenide (GaAs), II-VI groups compounds like cadmium sulfide (CdS)

and cadmium telluride (CdTe), copper indium diselenide (CIS), and copper indium gallium selenide (CIGS). GaAs material has suitable bandgap (1.43 eV), high PCE (28.8%), and strong antiradiation damaging feature. The GaAs solar cell can work normally at 250 ^{o}C. The limitation of GaAs is the fancy price, which is mainly used for solar panels on spacecrafts. CdS and CdTe thin film solar cells have high PCEs (~ 16%) and lower costs than crystalline silicon cells. However, Cd is highly toxic and Te is extremely rare in the Earth's crust. Therefore, CdS and CdTe are not ideal substitutes of Si-based solar cells. The CIS thin film solar cell was first reported by Bell Laboratory in 1974. CIGS thin film solar cell is developed using Ga to partly replace Se in CIS, which has the highest PCE (~ 20.5 %) among all commercially significant thin film materials. The CIGS thin film solar cell has lower cost (about 1/3 of crystalline silicon solar cells) and pollution. However, Im and Se are relatively rare elements, which consequentially limits the development of CIGS.[4-6]

1.2.3 Organic thin film solar cells

Organic or polymer solar cells are fabricated from organic semiconductor thin films. Such materials are solution-processable, flexible, and inexpensive, which are suitable for massive production, such as roll-to-roll printing. In addition, the optical absorption coefficient of organic molecules is high, which provides an opportunity of cheap and large-scale utilization of solar energy. Up to now, the organic thin film solar cells are still limited by low PCEs (~17 %), poor stability, and short lifetime.[4-6]

1.2.4 Dye-sensitized solar cells (DSSCs)

DSSCs are a type of solar cells developed by imitating the principle of photosynthesis. A DSSC is mainly consisted of conducting substrate, nanocrystalline TiO_2 thin film, sensitizer molecules, electrolyte, and counter electrode. The dye-sensitized TiO_2 thin film is the key component of DSSC, which serves as light absorbing and charge transporting layer. The DSSC has advantages of low cost and concise process. Meanwhile all the materials are non-toxic and pollution free, and part of them can be recycled adequately. Presently, the PCE of DSSC is steadily above 10% and the

lifetime is 5~10 years, while the production cost is only about 1/5~1/10 of silicon-based solar cells. However, small organic molecules are typically employed as liquid electrolyte, which are highly volatile and diffluent. The leakage problem of liquid electrolyte limits the application and development of DSSCs.[4-6]

1.2.5 Perovskite solar cells (PSCs)

Perovskite solar cells (PSCs) contain an active layer, which is composed of perovskite-structured organolead halides. PSCs have opened up a new world in the photovoltaic field due to the outstanding optical, electrical and charge transporting properties the organolead halides.[12-14] Among types of perovskites, methylamine lead halide perovskites ($MAPbX_3$) have received the most extensive attention and been widely used as active layer in solar cells. Since the first application of $MAPbX_3$ in photovoltaic devices was reported by Miyasaka *et al.* in 2009,[15] the power conversion efficiency (PCE) of methylamine lead halide perovskite solar cells (PSCs) has rapidly grown from 3.8% to over 25.2% in 2020.[16]

Commonly, the $MAPbX_3$ perovskites are constructed through solution deposition, such as the "one-step" or "two-step" spin-coating methods.[17] Currently, the one-step spin-coating method is not only the simplest but also the most widely used approach for constructing hybrid perovskite films. In the one-step spin-coating method, the lead (II) salt (PbX_2) and methylamine halide (MAX) is dissolved in an aprotic polar solvent, such as *N*,*N*-dimethylformamide (DMF) or gamma-butyrolactone (GBL), spin-coated on a substrate to form a wet film, and crystallized to perovskite under thermal annealing. Beyond that, a wide range of deposition techniques, such as thermal vapor deposition,[18] vapor-assisted solution process[19] and chemical vapor deposition,[20] have been developed to prepare perovskite films. Although the new developed deposition techniques made remarkable achievement in improving the performance of perovskite solar cells, solution deposition method is still the most popular method because of its advantages, including but not limited to low-cost, ease of processing and compatibility of massive manufacturing.[12]

2 Perovskite solar cells

During the past decay, halide perovskite-based materials have attracted enormous attentions due to their unique and intrinsic optical and electronic features of these ambipolar semiconductors, which combine the sharp optical band edge, the wide-range tunable band gap, high charge mobility and diffusion lengths, high absorption coefficients and panchromatic absorption resulting from *s-p* antibonding coupling, strong structural defect tolerance and shallow point defects, benign grain boundaries, as well as low non-radiative recombination losses, etc.[15, 17, 18, 21-25] A variety of optoelectronic devices based on perovskite thin-films have been developed including, but not limited to, solar cells,[1, 15, 17, 18, 21-24, 26-28] light-emitting devices (LEDs),[29-33] photo-/radiation-detectors,[34-37] laser,[38, 39] thin-film field-effect transistors,[40, 41] and nonlinear optics,[42, 43] etc., although most of the studies have focused on the development of highly efficient solar cells or photovoltaic devices. Halide perovskites have a general formula of ABX_3, in which A is an organic or inorganic monovalent cation (eg: methylammonium ($CH_3NH_3^+$ or MA^+), formamidinium ($CH(NH_2)_2^+$ or FA^+), rubidium (Rb^+) or cesium (Cs^+)), B is a divalent metallic cation (eg: Pb^{2+} or Sn^{2+}), and X is a halide anion (eg: Cl^- , Br^- or I^-).[8, 15, 25, 44-46] The seminal work on perovskite-based solar cells was reported by Miyasaka and co-workers in 2009, when $MAPbBr_3$ and $MAPbI_3$ were used as the semiconductor sensitizer in dye-sensitized liquid junction-type solar cell.[15] Since then, massive research efforts over the world have resulted in unprecedented growth in the power conversion efficiency (PCE) of PSCs, soaring from 3.81 % in 2009 to the certified PCEs of 23.7 % in 2018 and 25.2 % in 2019,[16] taking the advantages, such as the abundance of the precursor materials, superior structural defect tolerance and remarkable ease of fabrication.[15, 47-51] At the meantime, a spurt of growth in the external quantum efficiencies (EQEs) (> 20%) for perovskite-based light-emitting

diodes and tremendous progress on the optoelectronic devices have also been witnessed.[31, 33, 37, 39]

2.1 Background of perovskite materials

2.1.1 Perovskites and their crystal structures

Perovskite was first given to a mineral, calcium titanium oxide ($CaTiO_2$), by Gustav Rose, a German scientist, to honor Russian mineralogist, Lev von Perovski. Compounds with crystal structures conform to AMX_3 type belong to perovskites.[52] The chemical formula of hybrid perovskite is commonly written as AMX_3, where A is an organic or inorganic cation, such as methylamine (MA^+), formamidinium (FA^+), or caesium (Cs^+); M is a metal cation, like lead (Pb^{2+}) or tin (Sn^{2+}); X is chloride (Cl^-), bromide (Br^-) and/or iodide (I^-).[12, 14]

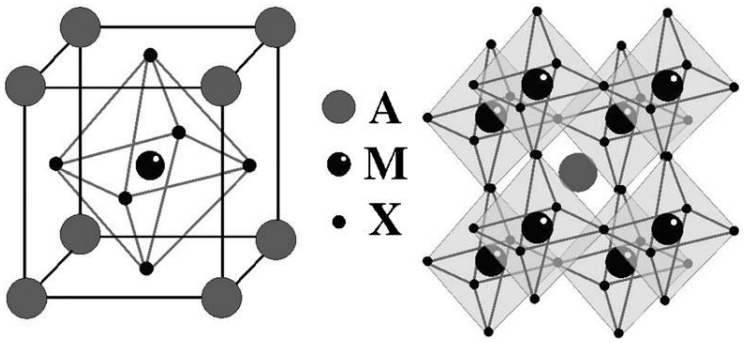

Figure 2.1.1. Left: Ball-and-stick model of the basic perovskite (AMX_3) structure. Right: Extended perovskite network structure connected through corner-shared octahedra.[4]

The general crystal structure of organometal halide pervoskite is shown in Figure 2.1.1, metal cation M and halide anion X constitute an octahedral configuration MX_6, in which one M cation locates in the center and six X anions occupy six vertices. One MX_6 octahedron connects to other six octahedra by sharing six X anions to form a three-dimensional (3D) network. In the network organic cation A locate in the spaces generated by the eight neighbouring octahedra to make the whole network

electroneutral. The A cation is encapsulated by twelve nearest X anions. If the A cations are too bulky, they cannot be ejected into the 3D network. Therefore, the size of A cation must be opportune to fit in the formed space, which is the precondition to form the perovskite.[4] At room temperature, perovskite materials have two types of crystal forms, tetragonal and orthorhombic crystals.[53]

2.1.2 Band structure of perovskites

The most common configuration of the pervoskite used for solar cells is $CH_3NH_3PbX_3$ (X = Cl, Br and I). As shown in Figure 2.1.2, the valence band maximum (VBM) of $CH_3NH_3PbI_3$ ($MAPbI_3$) is mainly determined by the σ-antibonding states of Pb 6s and I 5p orbitals, and the conduction band minimum (CBM) is principally confirmed by the σ-antibonding states of Pb 6p and I 5s orbitals.[7, 54] According to the evaluations from UV-Vis, UV photoelectron, and incident photon-to-electron efficiency (IPCE) spectra, the bandgap of $CH_3NH_3PbI_3$ is 1.50-1.55 eV.[55] The absorption wavelength range expanded to about 780nm is sufficient to support pervoskites responding to most of the sunlight.[5, 8, 9, 15, 52]

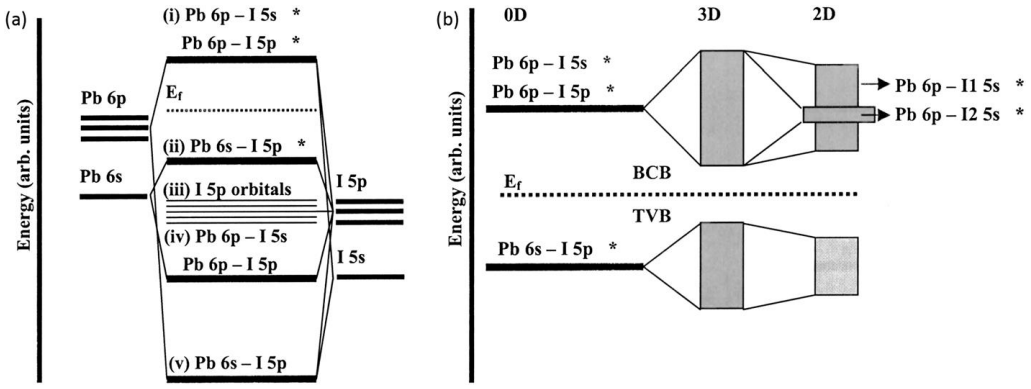

Figure 2.1.2. Bonding diagrams of (a) $[PbI_6]^{4-}$ cluster (0D), (b) $CH_3NH_3PbI_3$ (3D) and $(C_4H_9NH_3)_2PbI_4$ (2D).[7]

2.1.3 Properties of perovskites

Perovskites have high optical absorption coefficient and carrier mobility, which are excellent photovoltaic materials.[56] The low electron-hole recombination rate in

perovskite crystal ensures the long carrier diffusion length.[40, 57] The carrier diffusion length in $MAPbI_3$ is about 100 nm, and in $MAPbI_{3-x}Cl_x$ reaches 1 μm.[58] Thus, the charge carriers in perovskite have long lifetimes and strong transport properties. In addition, perovskite is both electron transporting and hole transporting material, which means it can form the heterojunction as either n-type or p-type semiconductor.[59] Therefore, perovskite can act as light absorbing layer and charge transporting layer simultaneously in PSCs.

2.2 Device structures of PSCs

Up to now, different types of device architectures have been developed, which mainly contain conventional structures and inverted planar structure.[1, 2]

2.2.1 Conventional structures

The conventional structures mainly contain mesoporous and planar structure.[1] The schematic device structures and charges transport of the two types are shown in Figure 2.2.1-1.

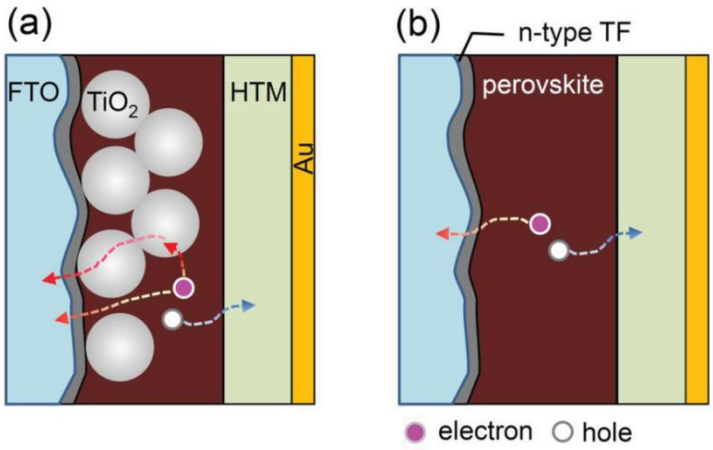

Figure 2.2.1-1. (a) Mesoporous perovskite solar cell with mesoporous TiO_2 layer and (b) planar structure with a planar TiO_2 layer.[8]

The planar structure is constructed with a typical inverted architecture, which contains substrate / anode / electron transporting material (ETM) / perovskite film / hole transporting material (HTM) / cathode. Indium tin oxide (ITO) or F-doped tin oxide (FTO) are usually used as anode materials; the ETM is a thin film of n-type semiconductor like TiO_2; p-type semiconductor materials are applied as HTM, 2,2',7,7'-Tetrakis[N,N-di(4-methoxyphenyl)amino]-9,9'-spirobifluorene (spiro-MeOT -AD) is one of the representative; cathode is common made by a metal material. In this case, the photoinduced electrons and holes are transported via perovskite layer to ETM / HTM film and finally the anode/ cathode, respectively. When the two electrodes are connected by wire, the discharge of perovskite solar cell will start. For

the mesoscopic nanostructure, the only difference is the perovskite layer, which is coated onto common a n-type oxide layer such as mesoporous TiO_2. Thus, the electrons can be transported to the ETM layer via perovskite or mesoporous particles of oxide.[8]

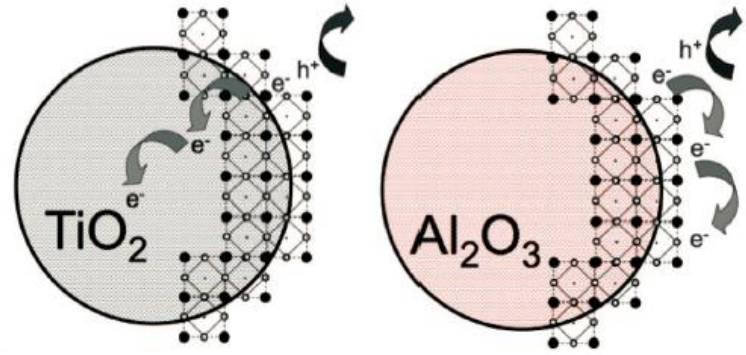

Figure 2.2.1-2. Schematic illustrating the charge transfer and charge transport in a perovskite-sensitized TiO_2 solar cell (left) and a noninjecting Al_2O_3-based solar cell (right).[60]

The objective of applying mesoporous oxide layer is to enhance the electron transporting ability of perovskite layer.[1] However, due to the fundamental energy losses, the mesoscopic nanostructure was found to have lower efficiency than the planar structure.[3] For perovskite solar cell, the fundamental energy losses are defined as the energy costed at the interface between perovskite and ETM. When the mesoporous TiO_2 was replaced by Al_2O_3 of the same size, the electrons were found to be collected only via perovskite layer, in theory the fundamental energy costs were minimized (Figure 2.2.1-2). This has been proved by the work done by H. J. Snaith *et al.*[60]

Actually, the devices that apply the conventional structures have two disadvantages. One is the energy-inefficient synthesis of TiO_2 materials, and the other is the limited candidates for cathode materials. To be specific, the synthesis of TiO_2 materials is complicated and an annealing process at 500 ^oC is involved, which deviates from the advantages offered by the solution processing of perovskite fabrication. Moreover, precious metals must be employed as cathode materials to avoid being oxidized, and a

more delicate metal evaporator is also needed to achieve this, which significantly increases the production expense.[1, 44]

2.2.2 Inverted planar structure

Comparatively, the inverted planar structure is constructed through the convenient and low-temperature solution processing, and cheap metals can be applied for the top electrode materials. The conventional structure usually uses poly (3,4-ethyl-enedioxythiophene) : poly(styrene sulfonate) (PEDOT : PSS) as HTM and [6,6]-phenyl-C61-butyric acid methyl ester (PCBM) as ETM. The inverted maintains efficient charge transferring ability between the interfaces of HTM, ETM and perovskite layer, and then ensures the dissociation and extraction of charges inside the perovskite layer happens adequately, which is the fundament of achieving high performance devices.[12, 61] A conventional heterojunction structure is shown in Figure 2.2.2-1, which is ITO (cathode) / PEDOT : PSS (HTM) / $CH_3NH_3PbI_{3-x}Cl_x$ (perovskite) / PCBM (ETM) / Al (anode).

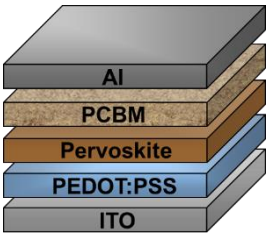

Figure 2.2.2-1. A conventional heterojunction structure of perovskite solar cell.

Comparing to conventional device structures, the inverted planar structure can be fabricated through convenient and low temperature processing. Additionally, the inverted planar structure also has other advantages over conventional device structures, such as compatibility to flexible substrates, suitability for massive roll to roll fabrication and negligible *J-V* hysteresis effects.[12, 61] Up to now, a high PCE of over 22 % was achieved for the inverted PSCs, which indicates their great potential in the future.[12]

2.3 Working principles of PSCs

Taking the inverted planar PSC (Figure 2.2.2-1) as an example, PCBM / perovskite / PEDOT : PSS layers can form a n-i-p junction inside the PSC. Firstly, the perovskite layer generates electron-hole pairs when absorbing solar light. The excited electron-hole pairs can be separated by the inside n-i-p junction, and then the electrons and holes are transported into PCBM and PEDOT : PSS layers, respectively. Because of the difference of energy levels, the carriers cannot return to perovskite layer but only be injected into electrodes by ETM or HTM. Finally, the transporting of electrons and holes creates the circuit. During the whole process the PSC will lose photoexcited carriers, for example, the recombination of electrons and holes in the perovskite layer, the ETM / perovskite interface, and the HTM / perovskite interface. Therefore, the loss of excited carriers should be reduced to increase the PSC performance. Specifically, the perovskite layer should be uniform and continuous, and the neighboring layers of PSC should adequately contact with each other. [1, 2, 4, 5, 8, 10, 14, 47, 61] A general diagram about working principles of a perovskite solar cell is shown in Figure 2.3. The cell is a 'p-i-n' type if it is illuminated from the p-side (HTL), but will be an 'n-i-p' type if illuminated from the n-side (ETL).

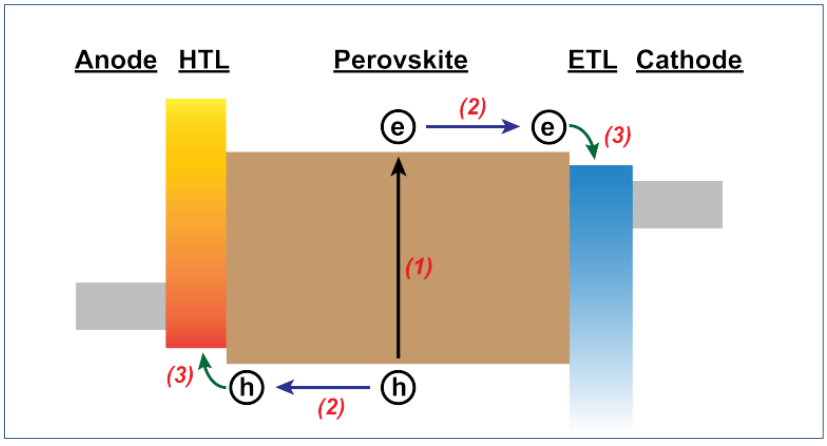

Figure 2.3. A schematic diagram of a perovskite solar cell. Step (1): Generation of electron-hole pairs upon light illumination. Step (2): Separation and transport of electron-hole pairs. Step (3): Charge carrier transfer to respective transport layers and eventual extraction at the electrodes.[11]

2.4 Fabrication methods of the perovskite layer

2.4.1 Conventional spin-coating methods

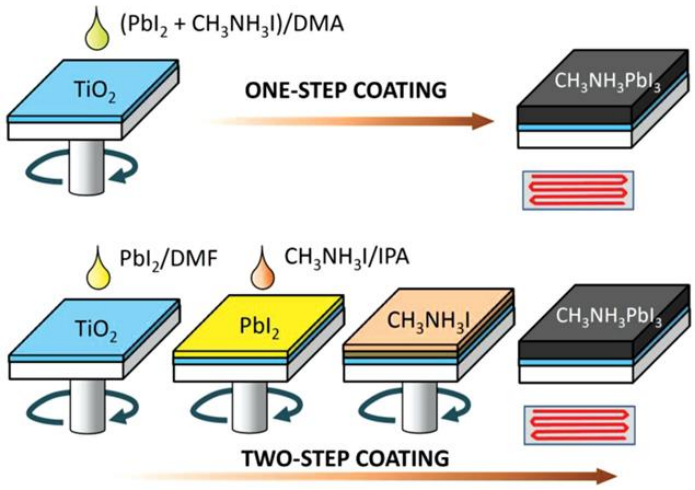

Figure 2.4.1-1. One-step and two-step coating procedures to deposit $MAPbI_3$ perovskite films.[8]

Currently, deposition perovskite layer on a substrate through spin-coating is a general approach for the fabrication. It is can be done in two ways, i.e. one-step coating and two-step coating (shown in Figure 2.4.1-1).[1, 2, 4, 5, 8, 10, 14, 47, 61] The one-step coating method is synthesizing perovskite by spin-coating a precursor solution and followed by the subsequent step of drying and annealing. The precursor solution is prepared by dissolving PbI_2/ $PbCl_2$ and methylammonium iodide (MAI) with an appropriate ratio in a polar aprotic solvent such as N,N-dimethylformamide (DMF), N,N-dimethylacetamide (DMA), and dimethyl sulfoxide (DMSO).[1, 2, 4, 5, 8, 10, 14, 47, 61] The two-step coating method is a little different from the one-step one, which deposits first a PbI_2 film and then a MAI film on the substrate by spin-coating a PbI_2 solution in DMF and a 2-propanol (IPA) solution of MAI respectively.[1, 2, 4, 5, 8, 10, 14, 47, 61] Drying and annealing steps are followed by each spin-coating process. Spinning rate, spinning time, and annealing temperature are important parameters that determine the quality of perovskite layer. In general, the two-step coating produces cuboid-like crystals of perovskite, while that synthesized by one-step method exhibits a shapeless

morphology.[1, 2, 4, 5, 8, 10, 14, 47, 61] Particularly, it was found that the perovskite film prepared by two-step coating method showed better photovoltaic properties, which demonstrates better morphology of perovskite layer is the key in improving performance of PSC.[1, 2, 4, 5, 8, 10, 14, 47, 61]

2.4.2 Modified deposition methods

The perovskite layer fabricated by conventional solution processed spin-coating methods still exist several disadvantages. In brief, the two-step spin-coating method always produces incompletely reacted perovskite layer, while the one-step method usually constructs the perovskite layer of poor morphology. Thus, types of strategies were developed to modify the deposition method.

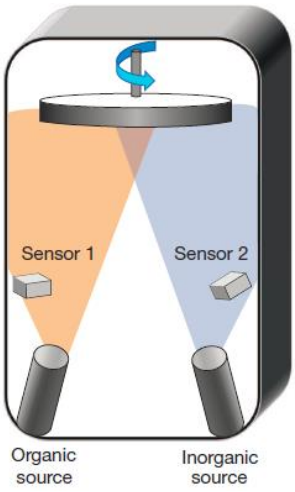

Figure 2.4.2-1. Dual-source thermal evaporation system for depositing the perovskite absorbers; the organic source was MAI and the inorganic source PbI_2.[18]

The dual-source thermal evaporation method (shown in Figure 2.4.2-1) was developed by Snaith *et al.*, which simultaneously evaporated the organic and inorganic materials upon the substrate under high vacuum. The completely reacted perovskite layer was extremely uniform and highly crystalline, and the PSCs based on such perovskite layer had PCEs of 15%. However, the delicate equipment and complicated process are unfavorable for cost control.[18]

Subsequently, a vapor-assisted solution process was demonstrated by Yang *et al*, of which the principle is shown in Figure 2.4.2-2. This process combined the conventional two-step method and the dual-source thermal evaporation method, which firstly spin-coated an inorganic layer upon the substrate, and then diffused the organic vapor into the inorganic layer to form perovskite. Through this process they synthesized perovskite layer in glovebox with high surface coverage, uniform surface, and large grains. Deservedly, the devices based on such perovskite layer of high quality achieved high PCE (12.1%).[19]

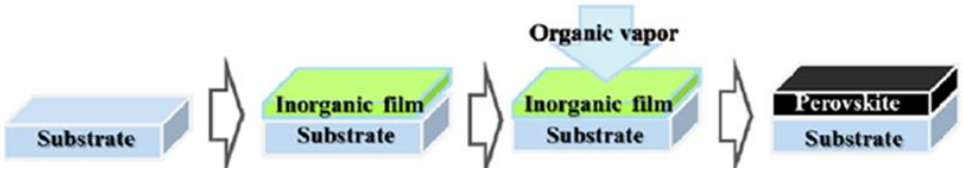

Figure 2.4.2-2. The principle of perovskite synthesis via vapor-assisted solution process.[19]

2.4.3 Fast deposition-crystallization methods

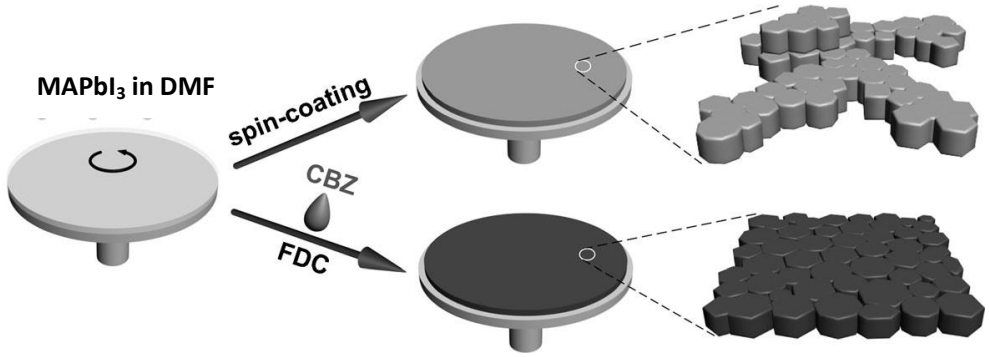

Figure 2.4.3-1. Schematic illustration of the FDC process and conventional spin-coating process for fabricating perovskite films.[62]

Spiccia *et al.* adopted a fast deposition-crystallization (FDC) method, also known as anti-solvent crystallization-assisted method, to construct highly efficient PSCs, and the schematic illustration is shown in Figure 2.4.3-1. They thought the conventional

spin-coating method would produce the perovskite layer consisted of non-uniform large crystals due to slow crystallization. For the FDC method, a mixed solvent of DMSO and GBL was always used, and a poor solvent like chlorobenzene or ether was introduced upon the wet film during the spin-coating, which can result in a fast crystallization of uniformly sized perovskite grains.[62] Until now the FDC method is still one of the most popular method in perovskite film fabrication, and the PSCs constructed by FDC had the highest recorded PCE of 25.2%.[1, 47]

2.4.4 Employment of additives

The employment of additives can also improve the crystalline degree of perovskite and get the perovskite layer with better morphology. Liang et al. applied a precursor solution with a bidentate halogenated additive 1,8-diiodooctane (DIO) to control the crystallization process of perovskite, which got a perovskite layer with high quality and increased the PCE by 31%. According to Lewis hard and soft acid-base theory, Pb^{2+} is a soft acid, which prefers to be coordinated by soft bases. They believed the chelating ligand DIO can replace I^- to provisionally coordinate with Pb^{2+} and form a more stable intermediate (shown in Figure 2.4.4-1). During the annealing process the slower removal of DIO can delay the formation of perovskite and improve its crystallinity.[63]

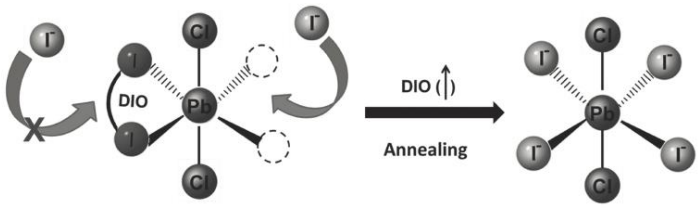

Figure 2.4.4-1. Schematic diagram for the transient chelation of Pb^{2+} with DIO.[63]

Ding *et al.* added CH_3NH_3Cl (MACl) or NH_4Cl into the precursor where the molar ratio of PbI_2 to MAI is 1:1, which decelerated the crystallization of $MAPbI_3$. The resulted perovskite layer had perfect crystallinity and uniformity, which enhanced the collection and transporting of charge carriers. The addition of NH_4Cl increased the FF

of PSCs to 80.11%.[64]

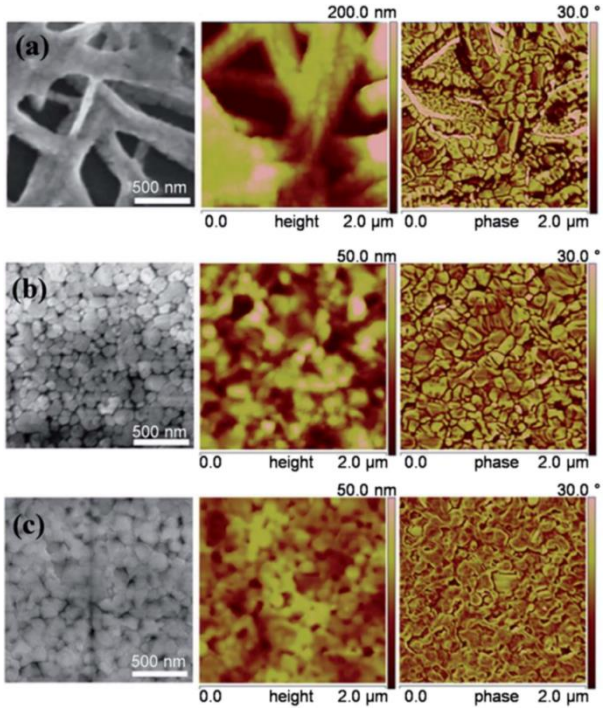

Figure 2.4.4-2. SEM (left), AFM height (middle) and phase (right) images for $MAPbI_3$ films fabricated using no additive (a), 17.5 mg mL^{-1} MACl (b), and 17.5 mg mL^{-1} NH_4Cl (c), respectively. [64]

2.5 Knowledge gap and main techniques used

2.5.1 The influences of Pb(II) coordination chemistry on the perovskite formation processes

In this project, the single crystals of different perovskite intermediates were designed and successfully grown according to the crystal engineering. The single crystals of $MAPbI_2Cl \cdot DMF$ and $MAPb_{1.5}I_3Br \cdot DMF$ were grown from the diluted precursor solutions through solvent-solvent diffusion method, and the structures of both were identified by the X-ray single crystal diffraction for the first time. The crystal structures were similar to typical organometallic complexes of Pb(II) cations, which contained 1-D lead-halogen chains and crystalline organic species. The structures of intermediates were found playing important roles in the perovskite formation processes through influencing the evaporation temperatures of crystalline DMF molecules and MAX gases. Therefore, the halogen species in precursors led to different crystal structures of intermediates, and further determined the formation mechanisms of perovskite thin films.

In fact, not only the anions in the lead salts, but also the solvents used in the precursor solutions were found had special influences in the perovskite formation processes. Briefly, the pure DMF-based precursor solution caused the limited nucleation and let the perovskite film came into being underwent a slow conversion from an intermediate phase. The pure GBL-based precursor solution produced perovskite film with high coverage according to the fast nucleation of the perovskite seeds. In this project, a series of PSCs were fabricated by using the dual-solvent strategy, and the highest performance device was achieved by using the mixed solvent of DMF and GBL with ratio of 35 %: 65 %. The formation of the best performance films was a result of the fast nucleation of the perovskite crystals and the slow conversion of the intermediate phase to perovskites, which led to good morphology and large grain sizes. Obviously, solvent engineering provided a simple approach to improve the

qualities of perovskite films by combining the advantageous properties like high crystallinity, large grain sizes, and high coverage.

By studying the perovskite formation from chloride-precursor solution, a recrystallization process of $MAPbI_2Cl \cdot DMF$ was found happened before spin-coating or at the early stage of annealing of precursor film. After the recrystallization process $MAPbI_2Cl \cdot DMF$ had much better orientation, which would then fast release the crystalline DMF and convert to the second intermediate $MAPbI_2Cl$. The second intermediate $MAPbI_2Cl$ did not undergo the pre-reported process where decomposed to MACl and PbI_2, but converted to $MAPbI_3$ and $MAPbCl_3$. The reaction between $MAPbCl_3$ and MAI was very slow, which limited the perovskite formation speed but helped to produce perovskite film with high crystallinity. This work was done for the first time that studied the formation mechanism of perovskite based on single crystals of intermediates, which reasonably indicates the chemical reactions happened during the formation process on molecular level.

$Pb(OAc)_2$ was a promising lead salt used for the massive fabrication of perovskite solar cells, because the ultra-fast formation of perovskite film from acetate-based precursor solutions. Several groups of PSCs from $Pb(OAc)_2$-based precursors were construted by changing hydrate number, changing spin-coating method, and applying DMSO as additive. The H_2O molecules in precursors were found to improve the film coverage. The pre-heating method avoided the low crystallinity when ensured the high coverage of perovskite thin films. In addition, the adding of DMSO as additive influenced the formation kinetics of perovskite films and improved the reproducibility of devices.

2.5.2 Main techniques used in the research

The top-viewed SEM images were used to observe the morphologies of perovskite thin films, like the film uniformity and grain sizes, while the cross-section one helped to check the connection between perovskite film and the other two charge transporting

films. The optical microscopy built the first step of observing the *in situ* crystallization and conversion of the precursor solutions, where the colour change indicated the chemical reaction happened. XRD analyses (both the powder and single-crystal) were the most important techniques used in the research, which clearly showed the crystallinities of perovskite thin films and the phase changes in the perovskite formation processes. In detail, the simulated annealing analyses of precursor solutions were achieved by comparing the XRD patterns with intermediates, and the initial XRD patterns intermediates were calculated from their single crystal structures. Besides, the fast XRD scan at narrow range of precursor annealing processes at different temperatures simulated the *in situ* condition and ensured the calculation of perovskite formation enthalpy. The HR-TEM provided high-quality electron diffusion patterns, where the d-spacing can be measured and compared with the lattice plains of components in the precursor films. In addition, some classical techniques, like HR-IR became useful method that determine the coordination condition of Pb(II) ions by measuring the vibration wavenumbers of ligands.

3 Promoting both fast nucleation and slow crystal growth to improve the quality of halide perovskite thin-films: a facial dual solvent approach

3.1 Introduction

Nowadays, people have arrived at a consensus on developing and utilizing cost-effective, environment-friendly, and sustainable energy sources.[1] Photovoltaics or solar cells have been considered as a potential technology that can effectively generate electricity from sunlight.[1, 10, 12, 47, 65] Recently, organo-lead-halide perovskite materials have attracted growing attentions due to their ideal light-harvesting capability, high charge carrier mobility, low carrier recombination rate, and low fabrication temperature (i. e. solution processing temperature below 300 ^{o}C). [4, 5, 8, 9, 15, 18, 52, 66] The organometal halide with formula AMX_3 (A = organic cation, M = metal cation, X = halide anion) is the key functional material in perovskite solar cells.[5, 8, 9, 15, 44, 52] The first application of perovskite in photovoltaics was reported by Miyasaka and co-workers in 2009, which was used as a semiconductor sensitizer in dye-sensitized liquid junction-type solar cell.[15] After only a few years of development, the power conversion efficiency (PCE) of PSCs has grown from 3.8 % to over 23.7 %.[15, 47]

Up to now, different types of device architectures have been developed, which mainly contain metal oxide based conventional mesoporous structure, metal oxide based conventional planar structure and poly (3,4-ethyl-enedioxythiophene: poly (sodium p-styrene sulfonate) (PEDOT : PSS) based the inverted planar structure or p-i-n planar structure, with p-type and n-type materials as bottom and top charge transport layers, respectively.[60, 67-70] Comparing to conventional device structures, the inverted planar structure, which is adopted from organic thin-film solar cells, can be fabricated

through convenient and low temperature processing. Additionally, the inverted planar structure also has other advantages over conventional device structures, such as compatibility to flexible substrates, suitability for massive roll to roll fabrication and negligible *J-V* hysteresis effects.[2, 3, 61, 69, 70] Up to now, a high PCE of 22% was achieved for the inverted PSCs, which indicates their great potential in the future.[1, 71]

Currently, depositing perovskite film onto substrate through spin-coating is a general approach. It can be done in two ways, one-step coating and two-step coating. One-step coating method has the advantages including ease of processing and possibility of massive manufacturing.[72-75] However, due to the fast and uncontrollable reaction between PbI_2 and methylamine iodide (MAI) during spin-coating and annealing, the morphology and the quality of the perovskite films produced are generally poor.[1, 62] Various methods were developed to improve the morphology, which can be divided into two different approaches: retarding or accelerating crystal growth. For the retarding strategy, usually some coordination ligands of Pb (II) are added as additives into the precursor solutions, which form intermediate species to slow down the crystallization process of the perovskite film and improve the film morphology.[63, 76, 77] In fact, the retarding approach can indeed produce perovskite films with large grain sizes and improved morphology, but it also has its drawbacks, such as long thermal annealing time and pinholes on the perovskite film, which limit the performance and reproducibility of solar cells.[78] Apparently, the long processing time and low reproducibility is not favorable for massive production.[79] $PbCl_2$ has been widely used to replace PbI_2 for perovskite film fabrication.[75, 80-84] The chloride can retard the crystallization and produce large grains, but the resulted films have pinholes and the annealing time is usually long.[85, 86] On the other hand, the accelerating strategy is characterized by adding anti-solvent such as chlorobenzene (CB) and dichlorobenzene (DCB) onto the perovskite wet films during spin-coating.[87, 88] This method only needs a very short annealing time and can produce compact and pinhole-free perovskite films with significantly improved the efficiency and reproducibility.[87, 88] However, the fast crystallization often produces perovskite films

with small grain sizes, which limits the performance and stability of the devices. Meanwhile, the accelerating methods greatly increases the complexity of the spin-coating process, which hinders its application for linear coating fabrication.[64]

Gamma-butyrolactone (GBL) and N,N-dimethylformamide (DMF) are the two common solvents used to prepare the perovskite precursors.[47] GBL is a non-coordination ligand to lead (II), in which PbI_2 or perovskite has limited solubility.[47] Generally, GBL-based precursors can produce compact and pinhole-free perovskite films, but the film is thin and the crystal grains are small.[89] On the contrary, DMF is a good coordination ligand to lead (II), which can dissolve lead halides at much better solubility. The perovskite films produced from DMF-based precursors usually have large grains, but morphologies are generally poorer.[62-64, 74, 76-79, 85-92] We believe the large grain size and better crystalinity of the film from pure DMF was led by slower crystal growth due to the formation of the intermediate, while the smooth morphology with a good coverage and a smaller grain size was caused by fast nucleation. We therefore hypothesized that the a dual solvent containing DMF and GBL would offer the characters of both fast nucleation and slow crystal growth, resulting in the peroovskite films with better mophology and solar cells with higher PCEs.

We thus prepared the precursors by using $PbCl_2$ as lead source and different GBL-DMF mixtures as solvents, and tried the precursors to construct devices. The devices using different DMF-GBL mixtures (DMF:GBL (v:v) = 0:10, 1:9, 2:8, 2.5:7.5, 3:7, 3.5:6.5, 4:6, 5:5, 6:4, 7:3, 8:2, 9:1 and 10:0) as the solvents were fabricated and characterized. The perovskite films were characterized by UV-Vis, XRD and SEM. In addition, the film formation process was studied and a possible mechanism was proposed. It was found that when pure GBL or DMF was used, the PCEs of devices are 8.600 % and 8.082 %, respectively, which are comparable to the literature values, 9.00 % for GBL and 7.90 % for DMF.[63, 76] Generally, the perovskite solar cells produced from the mixed solvents had better performance, expect at DMF:GBL = 5:5

(v:v), where the PCE reached its minimum of 6.944 %. The best device performance of PCE = 11.556 % was achieved when DMF:GBL = 3.5:6.5 (v:v). Clearly, solvent engineering was a simple but effective method to improve the performance of PSCs.

3.2 Results and discussion

3.2.1 Photovoltaic performances of PSCs

To study the influence of solvents with different volumetric ratio of GBL/DMF on PSC performances, the PSCs with the inverted planar structure of ITO / PEDOT : PSS / PVSK / $PC_{61}BM$ / Al were adopted (as shown in Figure 3.2.1-1).

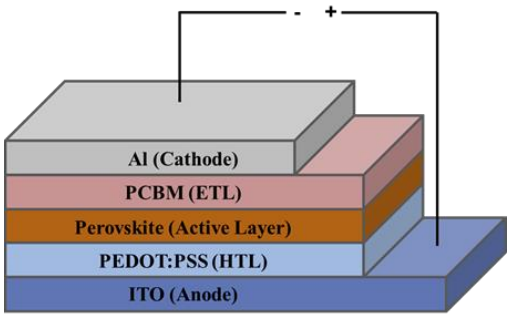

Figure 3.2.1-1. The inverted planar structure of PSCs.

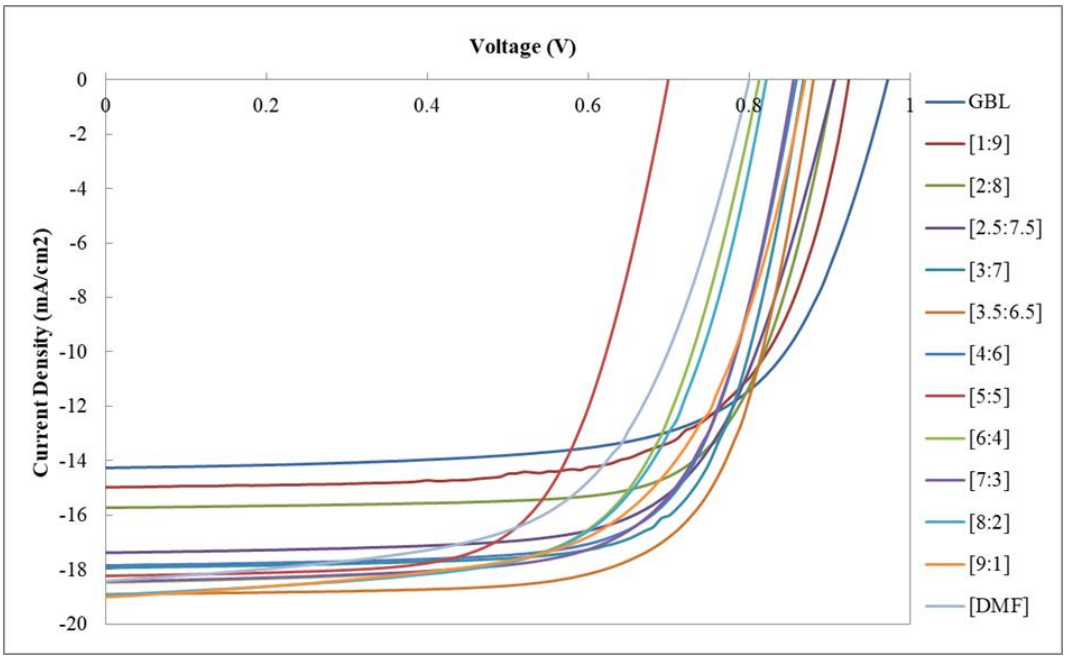

Figure 3.2.1-2. *J-V* curves of PSCs from different precursors. The devices are labeled as [DMF:GBL(v/v)].

The precursor solutions were prepared based on the solvents of mixed DMF and GBL at different volumetric ratios, and the related PSC devices were labeled as [volumetric ratio of DMF:GBL]. The results of current density-voltage measurement of PSCs based on different precursors were shown in Figure 3.2.1-2, and the related photovoltaic performances were summarized in Table 3.2.1.

Table 3.2.1 Photovoltaic performances of PSCs from different precursors. The average data of PCE is taken from 8 individual devices. The devices are labeled as [volumetric ratio of DMF:GBL].

Note	V_{OC} **(V)**	J_{SC} **(mA/cm^2)**	**FF**	**PCE (%)**	PCE_{MAX} **(%)**
DMF([10:0])	0.775±0.014	17.767±0.790	0.587±0.010	8.082±0.416	9.018
[9:1]	0.846±0.020	18.673±0.444	0.607±0.012	9.585±0.353	10.178
[8:2]	0.812±0.023	18.386±0.523	0.635±0.019	9.485±0.572	10.165
[7:3]	0.847±0.006	17.360±0.346	0.693±0.005	10.193±0.235	10.672
[6:4]	0.796±0.020	17.660±0.212	0.659±0.019	9.269±0.394	9.626
[5:5]	0.647±0.049	17.480±0.521	0.614±0.047	6.944±0.935	8.940
[4:6]	0.856±0.007	17.513±0.326	0.711±0.005	10.658±0.190	10.947
[3.5:6.5]	0.884±0.004	18.319±0.374	0.695±0.010	11.251±0.316	11.556
[3:7]	0.844±0.067	17.896±0.401	0.724±0.045	10.936±0.424	11.456
[2.5:7.5]	0.892±0.011	16.626±0.423	0.690±0.018	10.237±0.195	10.543
[2:8]	0.903±0.008	15.394±0.365	0.713±0.013	9.914±0.322	10.501
[1:9]	0.921±0.022	14.919±0.527	0.697±0.021	9.587±0.540	10.334
GBL([0:10])	0.940±0.029	13.272±0.683	0.690±0.024	8.600±0.561	9.551

Clearly, the precursor based on pure GBL solvent produced PSCs with an open-circuit voltage (V_{OC}) of 0.940 V, a short-circuit current density (J_{SC}) of 13.272 mA/cm^2, a fill factor (FF) of 0.690 and an overall PCE of 8.600 %, of which the J_{SC} was quite low. In comparison, the pure DMF-based precursor gave the PSCs with photovoltaic parameters including a V_{OC} of 0.775 V, a J_{SC} of 17.767 mA/cm^2, an FF of 0.587 and a similar PCE of 8.082 %. The PCEs of the two types of PSCs are comparable to the values reported earlier.[63, 76] Apparently, the device suffered from low J_{SC} when pure GBL was used as solvent, while a low V_{OC} and a poor FF were obtained for the device fabricated from pure DMF.

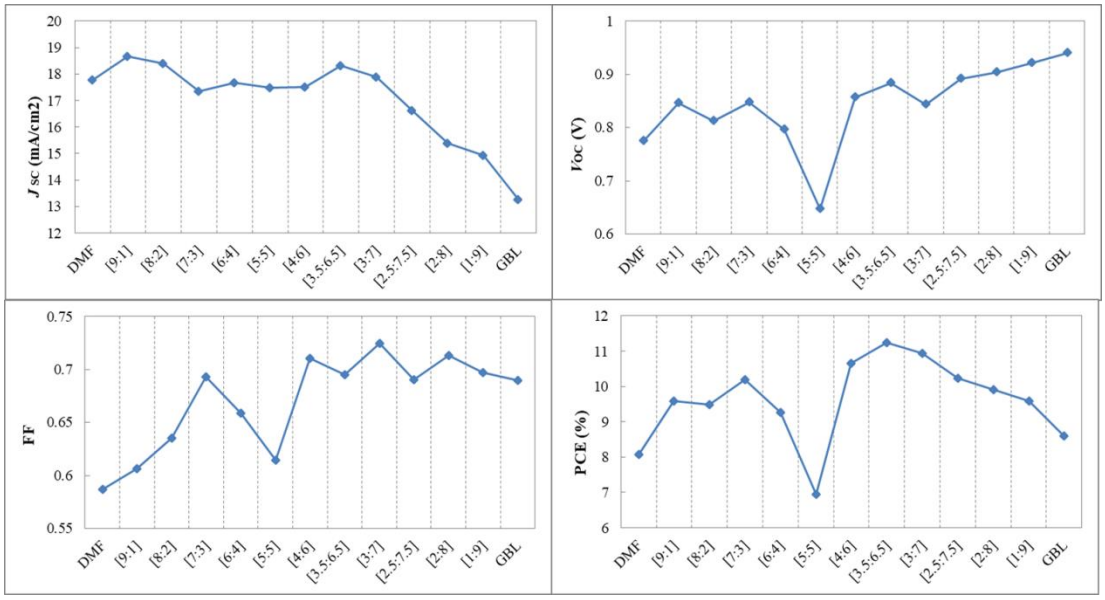

Figure 3.2.1-3. Statistics data of PSCs based on different precursors. The devices are labeled as [volumetric ratio of DMF:GBL].

Interestingly, when the volumetric ratio of DMF : GBL was tuned, the photovoltaic parameters change accordingly and the device PCEs show an maxima of 11.556% at DMF : GBL = 3.5:6.5 (v:v), and an minima of 6.944% at DMF : GBL = 5:5 (v:v). Figure 3.3.1-3 shows the statistics data of the PSCs. For the open-circuit voltage data, from left (pure DMF) to right (pure GBL) the V_{OC} presented an overall rising trend, except that it reached its minimum of 0.647 V when DMF : GBL = 5:5 (v:v). A maximum of 0.940 V was achieved when the pure GBL was used as the solvent. As for the short-circuit current data, J_{SC}, it remained as nearly a constant from pure DMF to DMF : GBL = 3.5:6.5 (v:v), and then started to decrease and reached its minimum of 13.272 mA/cm^2 for pure GBL. As a result, from pure DMF to pure GBL, the FF values initially raised and reached its maximum at DMF : GBL = 7:3 (v:v), and then went down to hit the minimum at the mixture of equal volumes of both solvents was used as the solvent. The FF value then increased to 0.724 and kept between 0.69 ~ 0.72 from DMF : GBL = 4:6 to 0:10 (v:v). The change of overall performance or the PCEs of the devices *vs* the solvent compositions followed a pattern very similar to that of V_{OC}. Thus, when the amounts of the two solvents were equal, the PSCs had the

poorest performance, of which the average PCE was only 6.944%. When DMF took more proportion in the solvent, the average PCE can go as high as 10.90% with DMF : GBL = 7:3 (v:v). If GBL took more proportion in the solvent, the device showed its best performance at DMF : GBL = 3.5:6.5 (v:v), with an average PCE of 10.936%, which was slightly higher than that when DMF dominates the solvent. Therefore, from the performance data, we can conclude that, for the binary system, the two solvents can complement each other and result in better device when one party is dominated in the solvent, but may become antagonistic to each other and lead to low performance devices when the two parties are at equal or closely equal amounts.

3.2.2 SEM study of the PSC thin films

As shown in Figure 3.2.2-1 and Table 3.2.4, the pure GBL based perovskite film had a compact and pinhole-free surface, where the uneven grains with sizes of 81.22 nm tightly packed. The pure DMF based perovskite film showed a typically continuous morphology with good coverage but obvious pin-holes and cracks, where the fiber-like perovskite crystals with sizes ranging from 160-300 nm unregularly arranged and tended to crystallized at plane direction.[63, 85, 93-99] According to Figure 3.2.2-2, obviously, the pure GBL based perovskite film was also dense as previously observed on top-viewed SEM images, where all the crystal grains packed tightly. Oppositely, the pure DMF based perovskite film was loose, where apparent tunnels and voids existed among the crystal grains. However, the pure GBL based film thickness was only 100 nm, while the pure DMF based one was 220 nm, which was more than two times thicker. Therefore, the dense and pine-hole free perovskite film from pure GBL resulted in the devices with high V_{OC}, but the thin thickness and small crystal grains with amounts of crystal boundaries also accelerated the carrier recombination, which limited the J_{SC} value. On the other hand, the larger grains and thicker perovskite films from the pure solvent of DMF enhanced the light absorption and carrier transportation, which led to the higher J_{SC} values, but the film defects, like pinholes and cracks, decreased the V_{OC} of devices.[100]

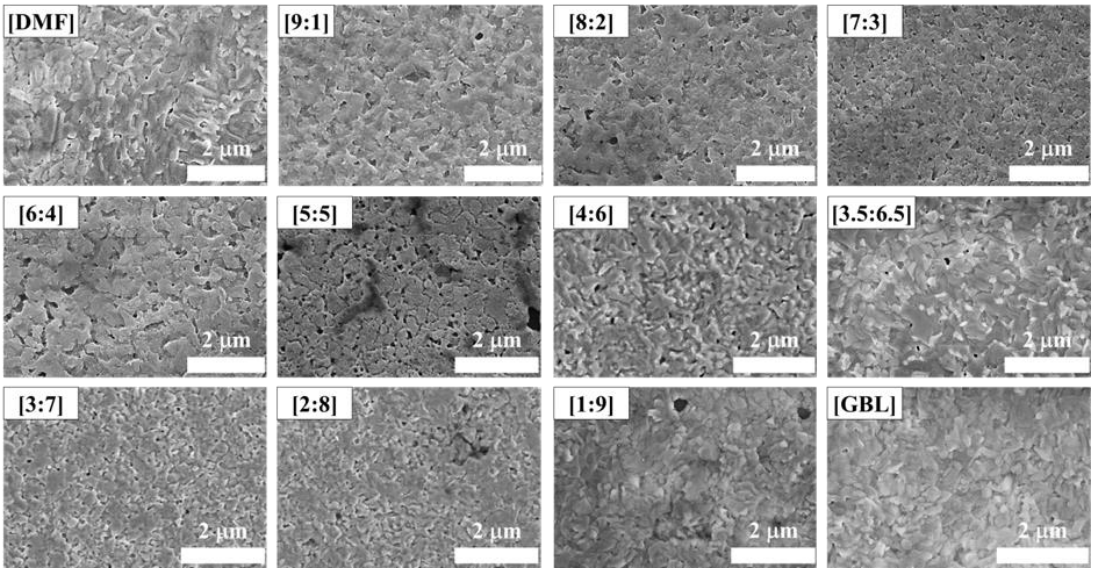

Figure 3.2.2-1. Top-view SEM images of perovskite films from different solvent combinations. The samples are labeled as [DMF:GBL(v/v)].

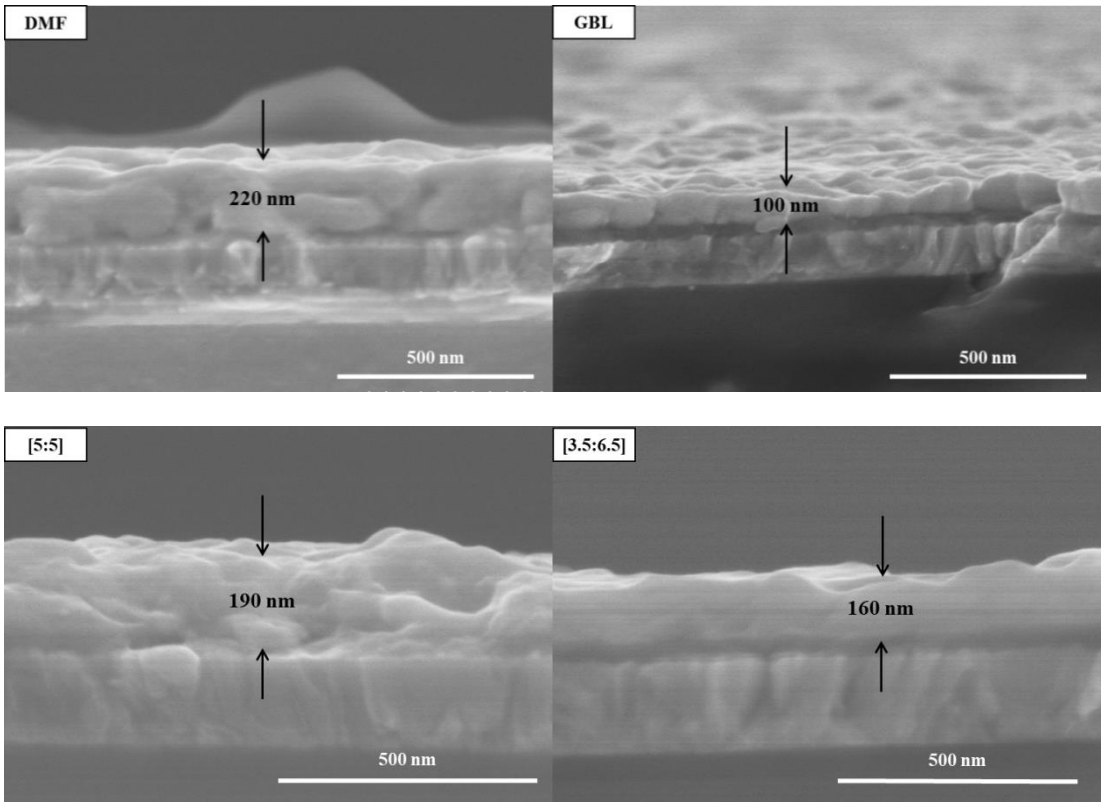

Figure 3.2.2-2. Cross-sectional SEM images of perovskite films from different solvent combinations. The samples are labeled as [DMF : GBL(v/v)].

Compared with the pure solvent-based perovskite film, the mixed solvent-based films were more uniform and continues, all of which owned a similar morphology with high coverage but uneven crystal alignment.[98] With increasing the ratio of DMF in the mixed solvents, the perovskite films tended to continuously crystallized at plane direction, which produced larger grains with fewer boundaries, but more pin-holes. Meanwhile, because of the improved solubility of the mixed solvents, the film thicknesses were also gradually increased. The best perovskite film was obtained from DMF : GBL = 3.5:6.5 (v:v), which had a uniform morphology with high coverage and few pin-holes. In addition, the micrometer-scaled crystals on the film showed obvious step-shaped structures, which indicated the high crystallinity.[101] Generally, the qualities of perovskite films from mixed solvents were improved, except for the film from DMF:GBL = 5:5 (v:v). The PSCs of DMF : GBL = 5:5 (v:v) showed the worst performance, whose perovskite film had a rugged morphology with numbers of conspicuous holes and voids. The poor morphology of perovskite film strongly influenced the light harvesting and charge transporting efficiencies, which limited the device performance at such a low level.

3.2.3 UV-Vis spectroscopic study of the PSC thin films

The UV-Vis spectra were used to measure the absorption properties of the perovskite films from the different solvents. Previous studies showed that the UV-Vis absorption spectra strongly depend on the morphology and thickness of perovskite films.[94, 101, 102] Generally, with a similar surface coverage degree, the absorption intensities of the perovskite films from 490 to 800 nm would increase significantly with the increase of film thickness. Meanwhile, a compact perovskite film with relatively small grain size and high surface coverage usually exhibit strong absorptions at 370 and 480 nm. In addition, the ratio of peak intensities at 370 and 480 nm can also represent the morphology of perovskite film. In detail, the higher ratio means the better morphology.[94, 101, 102] This phenomenon should be a result of complex scattering process inside the perovskite film, which enhanced the absorptions of shorter wavelengths.[102]

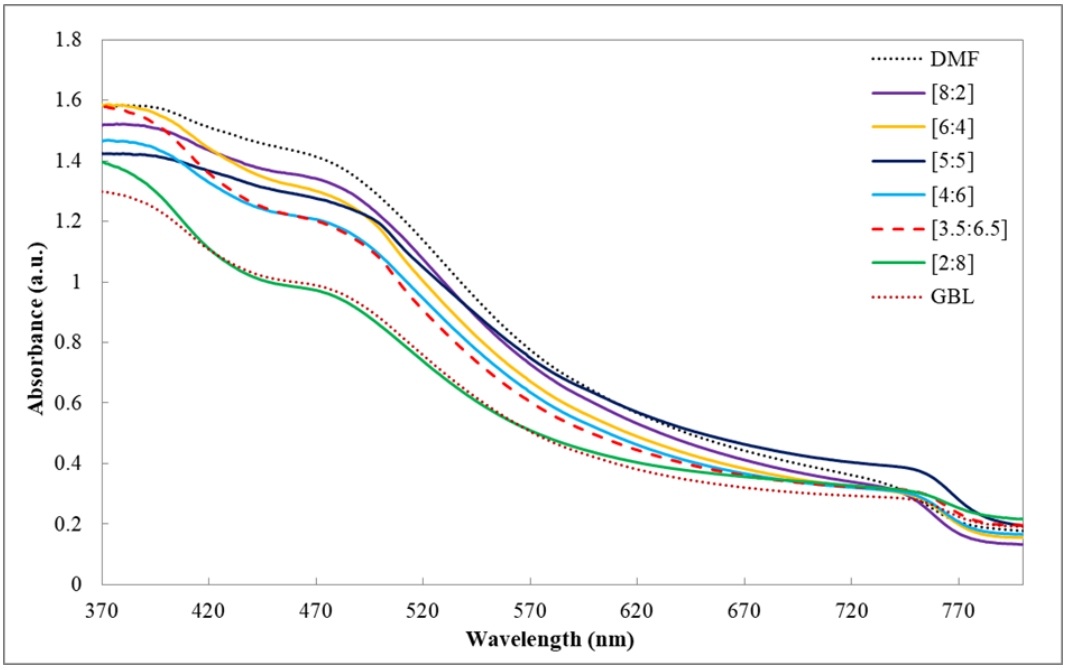

Figure 3.2.3. UV-Vis absorption spectra of perovskite films from different solvent combinations. The samples are labeled as [DMF:GBL(v/v)].

Figure 3.2.3 showed the UV-Vis absorption spectra of perovskite films from different solvent-combinations. All the samples displayed absorption onsets at ~800 nm and a sharp rise at ~780 nm, characteristic of the band-gap absorption of tetragonal $MAPbI_3$.[76] The absorption peaks at 370 and 480 nm belonged to the crystalline MA cations and Pb-I inorganic frameworks, respectively.[103] Obviously, with the solvent changed from pure GBL to pure DMF, the absorption intensities at lower energy area (490 - 800 nm) gradually increased, which was caused by increase of the thickness of the perovskite films.[94, 101, 102] In addition, when the precursors changed from pure GBL to DMF : GBL = 4:6 (v:v), the absorptions became much stronger at higher energy area (370-490 nm). Furthermore, the peak intensities of DMF : GBL = 3.5:6.5 and DMF : GBL = 6:4 (v:v) at 370nm were significantly high, which reached to the absorptions of 1.6. However, the ratio of peak intensities of DMF : GBL = 6:4 (v:v) at 370 and 480 nm was not as high as that of DMF : GBL = 3.5:6.5 (v:v). Based on previous studies,[102] it can be concluded that the perovskite film of DMF:GBL = 3.5:6.5 (v:v) contained good morphology, such as high surface coverage and large

crystal grains. However, when the solvent changed from DMF : GBL = 6:4 (v:v) to pure DMF, the absorption peaks at 370 nm began to turn flat. This phenomenon should be explained by the complex scattering effect, which was essentially caused by the poor morphologies of perovskite films.[94, 101, 102] Therefore, we can conclude that UV-Vis spectroscopy analysis results are in good consistence with the results from device performance data and the SEM images.

3.2.4 XRD study of the PSC thin films

The X-ray diffraction was used to determine the purities and crystallinities of perovskite films after. The XRD patterns of the perovskite films from different solvent-combinations were shown in Figure 3.3.4. Obviously, all the samples exhibited two diffraction peaks at 14.1^{o} and 28.5^{o}, which were assigned to the (110) and (220) lattice planes of $MAPbI_3$.[4] Thus, after annealing all the perovskite films exhibited the pure iodic perovskite phase. In addition, when the solvent changed gradually from pure GBL to pure DMF, the peak intensities increased accordingly, which indicated the enhancement of both crystallinity and the thickness of the perovskite films. The results agreed well with the results from device performance test, SEM and UV-Vis spectroscopic analyses.

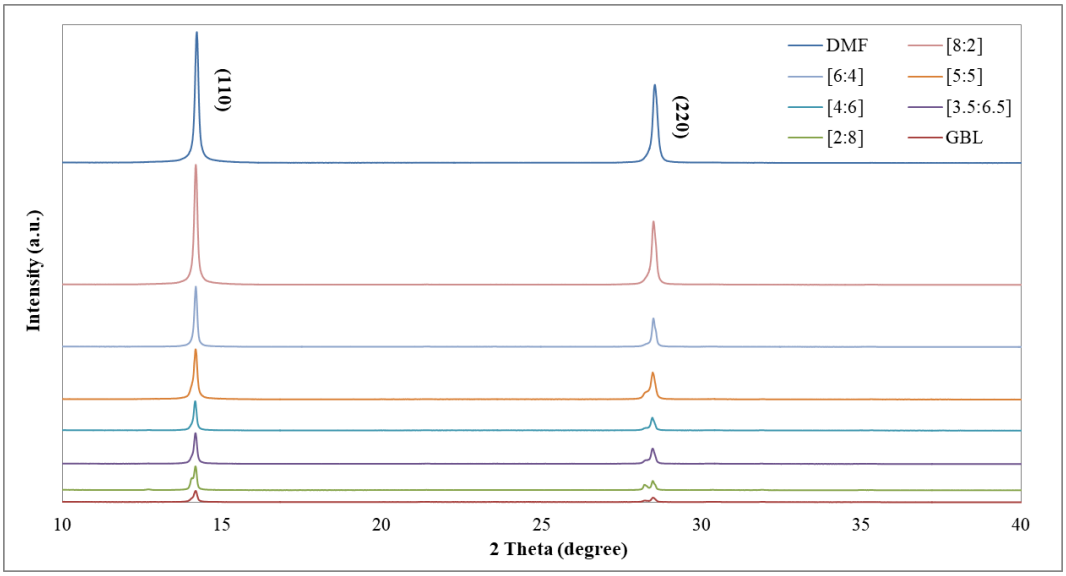

Figure 3.2.4. XRD patterns of the perovskite films from different solvent-combinations. The samples are labeled as [DMF:GBL(v/v)].

Table 3.2.4. The calculated average grain sizes of perovskite films based on the Scherer equation (D = K λ / B cos θ, where K here is 0.943, λ = 1.54056Å, B = FWHW × π / 180^o).

Sample	FWHW	Average grain sizes
DMF	0.0703 ^{o}	164.5 nm
[8:2]	0.1027 ^{o}	112.6 nm
[6:4]	0.1537 ^{o}	75.25 nm
[5:5]	0.2356 ^{o}	49.09 nm
[4:6]	0.1332 ^{o}	86.83 nm
[3.5:6.5]	0.1126 ^{o}	102.7 nm
[2:8]	0.1331 ^{o}	86.90 nm
GBL	0.1424 ^{o}	81.22 nm

3.2.5 Study of dual solvent effect and the film formation mechanism

To understand the effect of solvent engineering, we did some research on the perovskite film formation mechanism based on our observations and previous studies. We firstly examined the formation process of perovskite films from different solvents (DMF : GBL = 10 : 0, 3.5 : 6.5 and 0 : 10, v : v) using XRD. The XRD patterns of the wet films were recorded (Figure 3.2.5-1) immediately after the spin-coating was completed. Plastic bags were used to minimize the influence of moisture and air during the XRD pattern recording process. The diffraction patterns of ITO substrates in plastic bags were used as background.

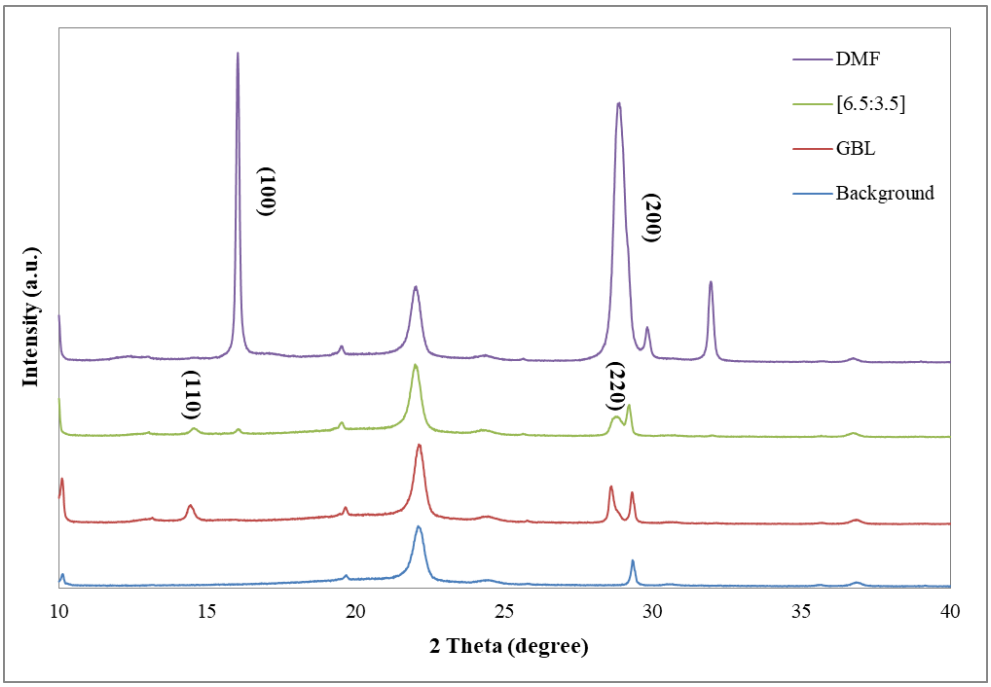

Figure 3.2.5-1. XRD patterns of the fresh perovskite films after spin-coating. The samples are labeled as [DMF:GBL(v/v)].

It can be seen that the wet film from pure DMF showed three strong diffraction peaks at 15.7, 28.7 and 31.5°. Among them, the two peaks at 15.7° and 31.5° were assigned to the (100) and (200) planes of $MAPbCl_3$ phase for the first time by Liu *et al.*[19] However, according to the study of Zhao *et al.*, the two peaks should be originated from a chloride-rich intermediate phase ($MA_{x+y}PbI_{2+x}Cl_y$), and the peak at 28.7° was attributed to perovskite.[94] For the wet film from pure GBL-based precursor, two much weaker diffraction peaks appeared at 14.1 and 28.5°, which belonged to $MAPbI_3$. Hence, the pure GBL-based precursor directly produced perovskite seeds in the wet film during spin-coating without forming any intermediate phase, which agreed with the mechanism proposed by Cui *et al.*[101] It was interesting to see that the wet film of DMF:GBL = 3.5:6.5 (v:v) exhibited diffraction peaks of both perovskite and the intermediate phase, which indicated the wet film contained both perovskite seeds and the intermediate phase ($MA_{x+y}PbI_{2+x}Cl_y$).

To discovery possible solvent effects in perovskite formation process, we used FT-IR to monitor the conversion processes of wet films from different precursors under vacuum at room temperature, which aimed to remove the excess free solvents in the wet films. The FT-IR spectra were shown in Figure 3.3.5-3, and the main vibration bands with their assignments of DMF, GBL, and MA cation were listed in Table 3.2.5. For the pure DMF-based precursor, after 10 minutes' vacuum treatment the vibration bands of DMF at 653 cm^{-1} and 1373 cm^{-1} red-shifted obviously, which indicated the DMF molecules coordinated with Pb(II) ions as electron donors.[104] In addition, the vibration bands of MA cation at 923 cm^{-1} also red-shifted, which proved the existence of MA cations in the intermediate compounds. Therefore, the strong coordination solvent DMF-based precursor tended to form an intermediate phase $MA_{x+y}PbI_{2+x}Cl_y \cdot m$DMF with other materials in the wet film. On the other hand, for the pure GBL-based precursor, all the vibration bands of GBL and MA cation did not shift during the whole process, which showed GBL acted as a non-coordination solvent in the precursor.[104] For the mixed solvent-based precursor, the shift of DMF's vibration bands were not clear due to the limited amount of $MA_{x+y}PbI_{2+x}Cl_y \cdot m$DMF, but the XRD patterns (Figure 3.2.5-1) proved the existence of $MA_{x+y}PbI_{2+x}Cl_y \cdot m$DMF in the wet film.

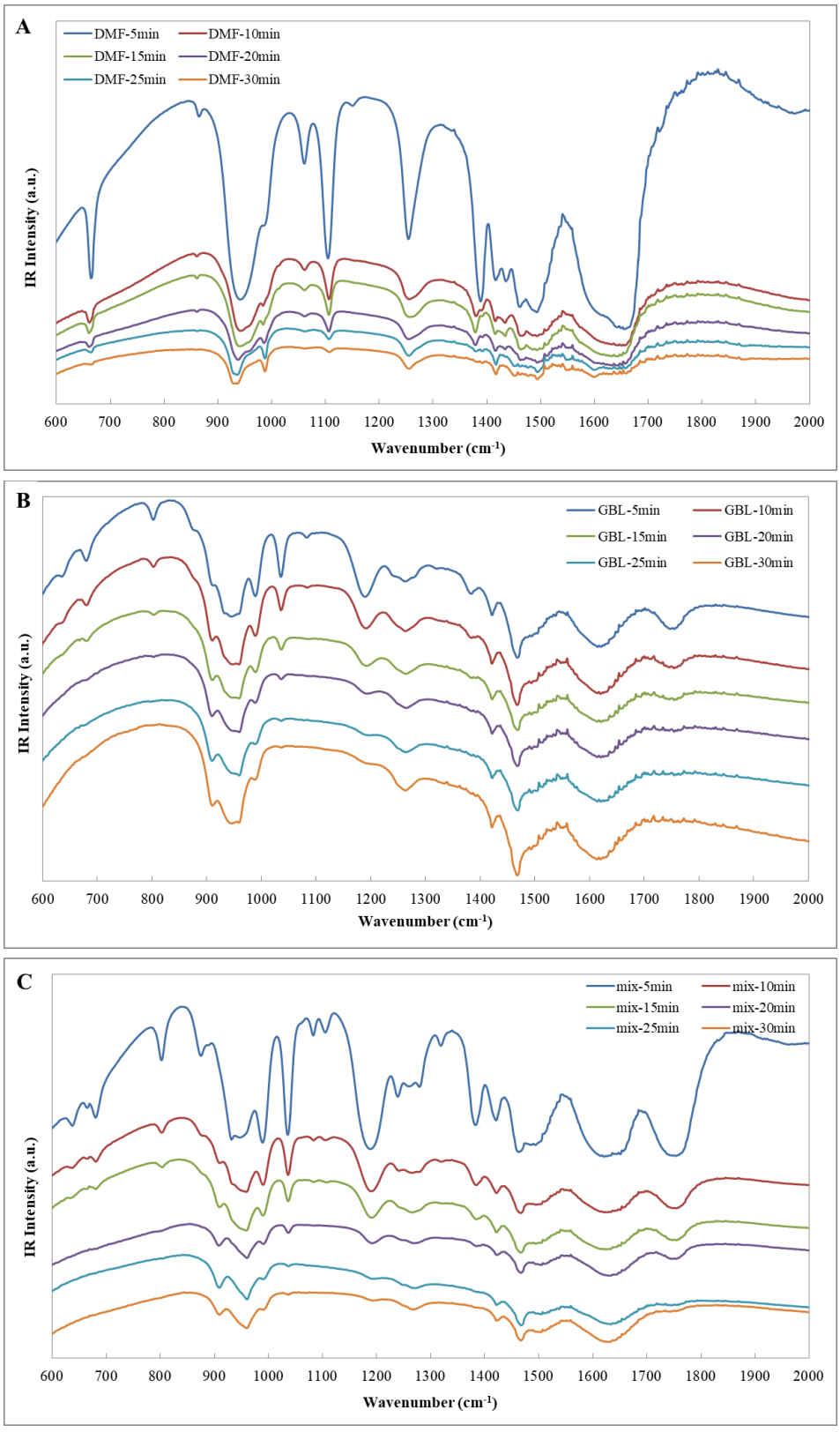

Figure 3.2.5-3. Time-dependent FT-IR spectra of wet films from (**A.** DMF-based precursor; **B.** GBL-based precursor; **C.** mixed-solvent based precursor) under vacuum.

Table 3.2.5 FT-IR vibration bands and assignments of DMF, GBL, and MA cation.

DMF	
Bands	Assignments
653 cm^{-1}	N-C=O bending $[\delta(N\text{-}C{=}O)]_{DMF}$
1091 cm^{-1}	methyl rocking $[\rho(CH_3)]_{DMF}$
1238 cm^{-1}	asymmetric C-N stretching $[\nu_a(C\text{-}N)]_{DMF}$
1373 cm^{-1}	combination of N-C-H bending $[\delta(N\text{-}C\text{-}H)]_{DMF}$ and C-N stretching $[\nu(C\text{-}N)]_{DMF}$
1641 cm^{-1}	carbonyl stretching $[\nu(C{=}O)]_{DMF}$
GBL	
Bands	Assignments
1037 cm^{-1}	symmetric C-O stretching $[\nu_s(C\text{-}O)]_{GBL}$
1170 cm^{-1}	asymmetric C-O stretching $[\nu_a(C\text{-}O)]_{GBL}$
1771 cm^{-1}	carbonyl stretching $[\nu(C{=}O)]_{GBL}$
MA^+ ion	
Bands	Assignments
923 cm^{-1}	$CH_3\text{-}NH_3^+$ rocking $[\rho(CH_3\text{-}NH_3^+)]_{MA^+}$
970 cm^{-1}	C-N stretching $[\nu(C\text{-}N)]_{MA}+$
1420 cm^{-1}	asymmetric CH_3 bending $[\delta_a(CH_3)]_{MA^+}$
1479 cm^{-1}	symmetric NH_3^+ bending $[\delta_s(NH_3^+)]_{MA^+}$

Based on the mechanisms proposed by Cui, Zhao and Amassian and our results, [94, 101, 105] for the precursors of different solvents, we proposed the formation mechanisms as shown in Figure 3.2.5-4.

i) In the pure DMF-based precursor, due to the strong coordination effect of DMF, limited number of $MA_{x+y}PbI_{2+x}Cl_y{\cdot}m$DMF crystals firstly form in the wet film during the spin coating. Because the $MA_{x+y}PbI_{2+x}Cl_y{\cdot}m$DMF crystals tend to grow at plain direction, the intermediate film grows based on the limited number of crystal seeds during the annealing process, and has large grains but poor morphology. Then the perovskite crystals form from the slow conversion of intermediate crystals, which finally results in the perovskite film with large grain sizes but poor morphology.

ii) In the pure GBL-based precursor, due to the limited coordination ability of GBL, precursor starts to produce perovskite seeds with the fast evaporation of GBL during the spin-coating process. Then the perovskite continues to crystallize or

grows around the preformed seeds during annealing, and eventually form the whole perovskite film. Therefore, the perovskite film from pure GBL has high coverage but small grain sizes.

iii) When the mixed solvent DMF : GBL = 3.5:6.5(v/v) is used, the wet film after spin-coating will contain both the intermediate ($MA_{x+y}PbI_{2+x}Cl_y \cdot mDMF$) and crystal seeds of perovskite. The crystal seeds of perovskite and intermediate will be evenly distributed in the wet film and serve as nucleus for the further crystallization of perovskite during the annealing process. It is the fast nucleation of $MAPbI_3$ and the slow conversion of $MA_{x+y}PbI_{2+x}Cl_y \cdot mDMF$ to perovskites that leads to the perovskite films with high coverage and large grains.

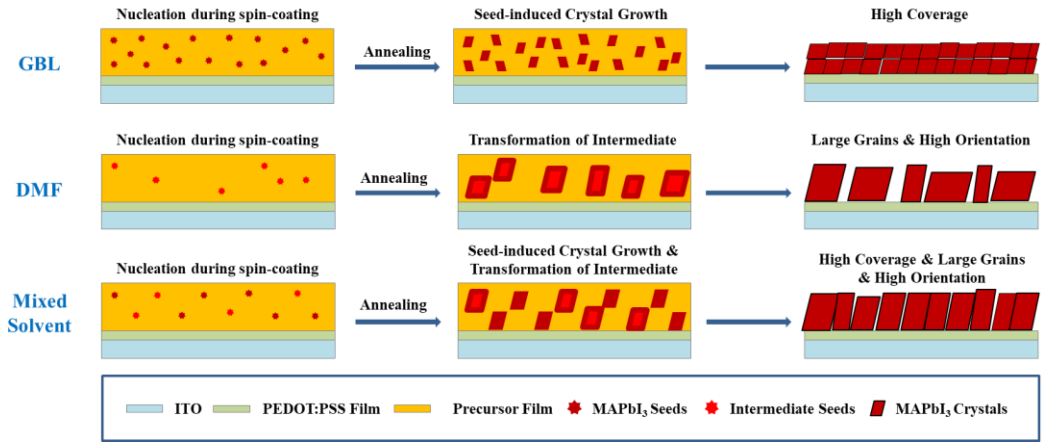

Figure 3.2.5-4. Formation mechanisms of perovskite films from different precursors.

3.3 Conclusion

By using solvent engineering strategy, we have successfully fabricated a series of PSCs with inverted structure from the chloric precursors in the solvents with DMF:GBL = 0:10, 1:9, 2:8, 2.5:7.5, 3:7, 3.5:6.5, 4:6, 5:5, 6:4, 7:3, 8:2, 9:1 and 0:10 (v:v). The photovoltaic performance of the devices was studied. While the average PCEs for the devices from precursors with pure GBL and DMF as the solvent are 8.600 % and 8.082 %, respectively, the highest average PCE of 11.556 % was achieved when the solvent with DMF : GBL = 3.5:6.5 (v:v) was used as the solvent. The largest J_{SC} and V_{OC} were obtained from the solvents with DMF : GBL = 9:1 and 0:10 (v:v), respectively. Generally speaking, solvent engineering produced perovskite films that contained advantageous properties like high crystallinity, good uniformity and high coverage, although the lowest PCEs (an average of 6.944%) was recorded for the PSCs obtained for the solvent with DMF : GBL = 5:5 (v:v). The techniques, such as SEM, XRD and UV-Vis were used to characterize the perovskite films obtained from different solvent combinations.

Meanwhile, the film formation process of perovskite layer from chloric precursor was studied. The film formation mechanisms were proposed for the films from the precursors with different solvent combinations, i.e., pure GBL, pure DMF and the mixtures of GBL and DMF. The high crystallinity films with large grains from pure DMF solvent were originated from the slow conversion of the intermediate phase, $MA_{x+y}PbI_{2+x}Cl_y \cdot m$DMF, to perovskites during the annealing. The smooth films from pure GBL were due to the quick formation the perovskite crystal seeds during the spin coating process due to the limited coordination ability, and the formation of the best performance films from DMF : GBL = 3.5:6.5 was a result of the quick formation of the perovskite crystal seeds during the spin coating process and the slow conversion of the intermediate phase, $MA_{x+y}PbI_{2+x}Cl_y \cdot m$DMF, to perovskites during the annealing, which lead to good morphology and high crystallinity.

4 Identification of two crystalline chloride-containing intermediates and their importance to perovskite film formation

4.1 Introduction

It is undeniable that the accomplishment of perovskite solar cells in photovoltaic performance is based on the experiences from numbers of trials and errors.[105-108] The apparently high PCE of perovskite solar cells cannot hide the objectively existed deficiencies of limited active area, low stability and poor reproducibility.[14, 85, 109-111] If the research of perovskite solar cells lacks a durative safeguard of essential mechanisms, the development would eventually get confine. Therefore, there have been various indications that the research trends gradually shifted to the formation mechanism study.[105, 112-120]

To date, $MAPbI_3$ and $MAPbI_{3-x}Cl_x$ were the most studied perovskites, and their formation processes were also research hotspots.[113, 119, 121-123] For the pure iodide perovskite $MAPbI_3$, as early as 2014, Kanatzidis *et al.* has found two intermediates, $MAPbI_3 \cdot DMF$ and $MAPbI_3 \cdot H_2O$, appeared in the conventional solution approach, and indicated it was the needle-shaped $MAPbI_3 \cdot DMF$ intermediate crystals that leaded to the low coverage and poor morphology of perovskite films formed from precursor (1:1 PbI_2:MAI).[53] However, no further research based on those intermediate crystal structures or the detailed mechanisms of perovskite formation was continued. In the same year, Wiesner and co-workers used *in situ* grazing incidence wide-angle X-ray scattering (GIWAXS) to study the thermal annealing process of $MAPbI_{3-x}Cl_x$,[124] and found three distinct structures dominated the formation of $MAPbI_{3-x}Cl_x$, which included a crystalline precursor structure, a 3D perovskite structure and a degradation mixture. Among them, the crystalline precursor structure had a GIWAXS pattern at $q = 11\ nm^{-1}$ which equals to a diffraction peak at $2\theta = 15.7^o$, which only appeared at the

early stage of annealing. A similar crystalline precursor structure was also found by Zhao's group,[94] which was showed as an intermediate phase with formula $MA_{x+y}PbI_{2+x}Cl_y$ that formed during spin-coating or at the beginning of thermal annealing. The intermediate phase $MA_{x+y}PbI_{2+x}Cl_y$ had two diffraction peaks at 2θ = 15.7 and 31.5°, and gradually transformed to pure iodide perovskite phase during annealing. In 2015, Snaith and co-workers used *in situ* WAXS to study the annealing for perovskite films produced from PbI_2 and $PbCl_2$, and the results showed that the intermediates which appeared from the two precursors were different.[125]

In 2016, the mechanism study has attracted more attention, several significant studies appeared to consummate the research. Cao *et al.* proved $MAPbI_2Cl$ was one intermediate formed during the annealing process from chloride precursor by XRD and UV-Vis methods.[117] Lidzey *et al.* determined the activation energy E_A for the formation of $MAPbI_{3-x}Cl_x$ from chloride precursor, which equals to 85 ± 9 kJ mol^{-1}.[115] Su and co-workers thought that the intermediates that appeared during annealing from chloride precursor are $MAPbCl_3$ and a PbI_2-solvent complex, and the mechanisms of perovskite formation changed at different temperatures.[116] In detail, when the annealing temperature was lower than 100°C, the perovskite formed from intermediates, while when the temperature was above 100°C, the perovskite would directly form from precursor. Furthermore, Luther *et al.* used *in situ* XRD to do the mechanism study and divided the formation processes of perovskite from iodide and chloride precursors into clear steps.[126] They found that in the whole formation processes the iodide one had one intermediate phase, while the chloride one had two. In 2017, Amassian *et al.* systematically researched the spin-coating processes of iodide, bromide and chloride precursors, and supposed that the three precursors produced wet films contained: crystalline $MAPbI_3 \cdot DMF$ and PbI_2; amorphous $MAPbI_{3-x}Br_x \cdot DMF$ and crystalline $MAPbI_{3-x}Br_x$; amorphous $MAPbI_{3-x}Cl_x \cdot DMF$, crystalline $MAPbI_{3-x}Cl_x$ and PbI_2, respectively.[105] Recently, Tassone *et al.* showed the crystalline intermediate appeared in the as-cast film from chloride precursor solution was a compound with formula of MA_2PbI_3Cl.[82] However, this result was inconsistent

with Amassian's that the intermediate contained crystalline DMF.[105]

Obviously, the *in situ* GIWAXS and XRD have become the most prevalent techniques that studied the formation mechanisms of perovskite films.[82, 105, 115, 116] Various works indicated that particular intermediates crystallized from iodide, chloride, and bromide precursors during spin coating, respectively, and proved the perovskites were transformed from such intermediates under thermal annealing. [82, 105, 115, 116] However, no matter the crystal structures of the chloride intermediates, the solidification details of precursor, or the crystallization mechanism of perovskite still remained large uncertainties.

In this chapter, we mainly used microscope and XRD to monitor the perovskite film formation from the chloride precursor solution (1:3 $PbCl_2$:MAI), and studied the mechanisms by dividing the whole process into steps. To break through the bottleneck, we adopted the single crystal X-ray techniques to identify the crystalline intermediates. For the first time, the single crystals of precursor were successfully grown from the precursor solution through the liquid-liquid diffusion method. The single crystal X-ray diffraction showed the crystal structure of the crystalline precursor was $MAPbI_2Cl \cdot DMF$, the layered-structure of which was consisted of lead-halide chains and organic fillers. The results from powder XRD and HR-TEM further proved $MAPbI_2Cl \cdot DMF$ crystals existed in the as-cast film and the recrystallization process of them also played an important role in producing high quality and orientation perovskite films. The identification of $MAPbI_2Cl \cdot DMF$ indicates that the most important missing link in the formation mechanism of perovskite from the chloride precursor solution is found. In addition, we suppose a series of chemical reactions to clarify the whole process. We hope our work can provide an effective approach for perovskite formation study, and help to create a new chapter for fabricating perovskite solar cells.

4.2 Results and discussion

4.2.1 Optical microscope and UV-Vis spectroscopic study of film formation

To study the perovskite film formation mechanism from chloride precursor solution, we firstly monitored the film morphology change at 80 ^{o}C by using optical microscope. The microscope images taken at different times are shown in Figure 4.2.1-1. The color change of film represents chemical reactions happen on the film. We put the whole process roughly into 3 stages (**S1** - **S3**) according to the morphology and the colors of the film. The first stage (**S1**) (0 - 2 min) represented the formation of a light-yellow crystalline intermediate phase **X1** from the precursor solution, where the intermediate crystallizes as small leaf-shaped crystals. The film has a high degree of coverage and a good morphology. The second stage (**S2**) of film formation happened at the time 5 to 25 min, where the transformation of the yellow-colored intermediate **X1** to red-brown intermediate **X2**. At the beginning of **S2**, the formation of **X2** happens randomly and slowly on the film, but accelerates as time goes till the whole film completely changed to **X2** in red-brown. In the last stage (**S3**), the film changes from red-brown to black gradually, indicating that the formation of perovskite is completed.

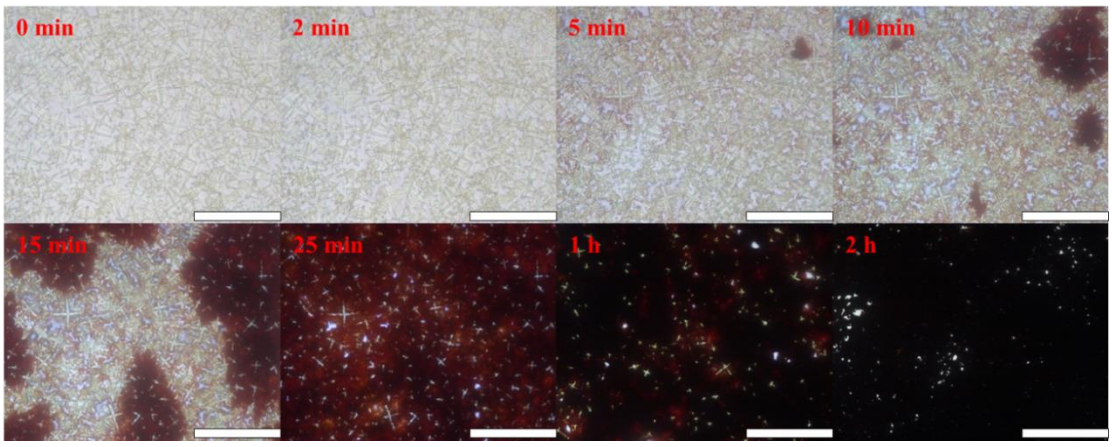

Figure 4.2.1-1. The microscope images of perovskite formation process at 80 ^{o}C. The scale bars correspond to 100 μm in length.

The annealing process was also examined by UV-Vis spectra (Figure 4.2.1-2). From **X1** to **X2** to perovskite, the absorption ranges of the film change from < 465 nm to < 645 nm to < 800 nm, which is consistent with the color change observed under optical microscope (Figure 4.2.1-1).

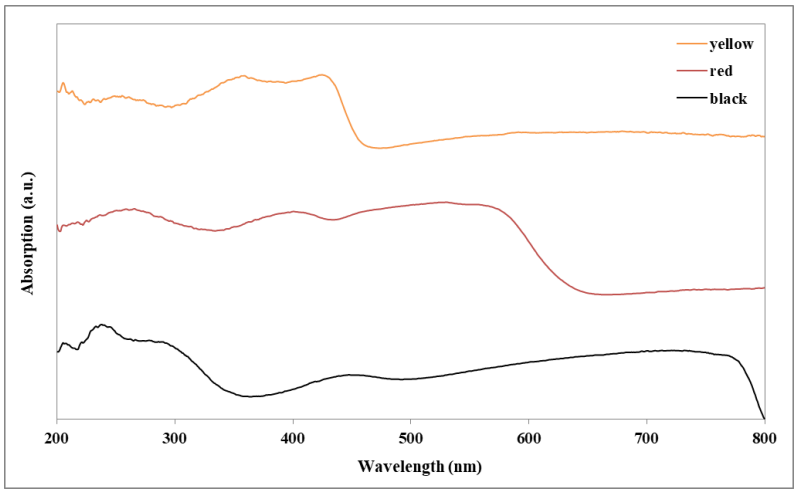

Figure 4.2.1-2. The UV-Vis spectra of perovskite film corresponding to its colors.

4.2.2 Electronic and coordination environment of Pb(II) in precursor and structural analysis of $MAPbI_2Cl \cdot DMF$

Up to now, numerous studies have shown the existence of intermediates **X1** and **X2** using different techniques, but their chemical compositions and the crystal structures were not assigned yet.[82, 94, 105, 115, 116, 121, 125, 126] Apparently, the chemical and structural information of the intermediates are the missing keys for fully understanding the film formation process. We believe the spin-coating and the film formation process is a process combining crystallizations with chemical reactions.

X-ray absorption spectroscopy (XAS) has been utilized to probe the electronic and coordination environment of lead in prepared aqueous solution. Figure 4.23.2-1 compares the X-ray absorption near edge structure (XANES) profile for PbI_2, $PbCl_2$,

and $CH_3NH_3PbI_3$ solution along with their corresponding Pb foil reference. Significant differences have been observed for all Pb samples, and this indicates the apparent disparities among the solid PbI_2, $PbCl_2$ and aqueous Pb-MAI solution. It should be noteworthy that the absorption edge energy E_0 of Pb-MAI solution (13035.0 eV) is same as in solid lead salt, indicating that it is in the +2 state similar to PbI_2.

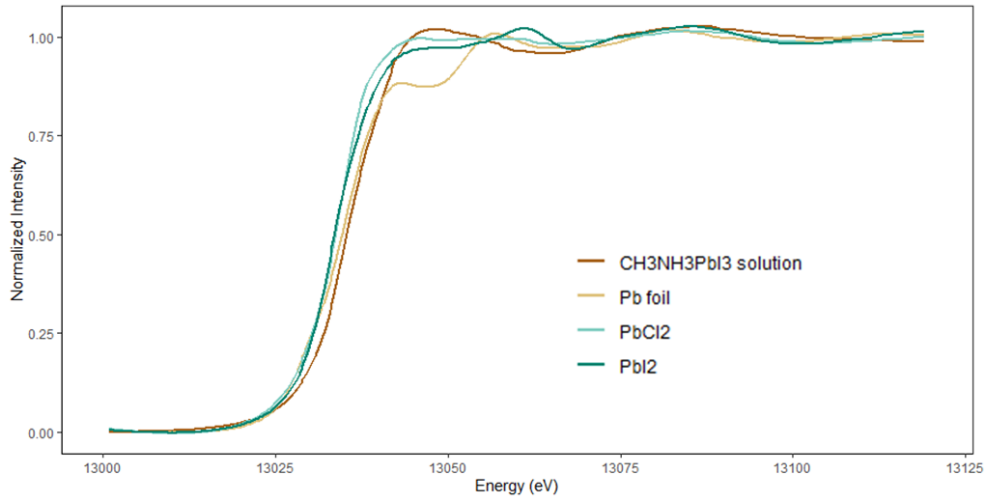

Figure 4.2.2-1. Pb L_3 edge XANES spectra for PbI_2 (powder), $PbCl_2$(powder), Pb foil and $CH_3NH_3PbI_3$ solution prepared by dissolving $PbCl_2$ (80 mM) and MAI (240 mM) in DMF.

We continued our path towards resolving the local structures around Pb atoms by Pb L3 extended X-ray absorption fine structure (EXAFS) spectroscopy. The fourier-transformed (FT) EXAFS (Figure 4.2.2-2) reveal a distinct growth of the primary peak (at around 2.5 Å, after phase-shift correction) when PbCl2 is mixed with MAI in DMF solution, suggesting that oxygen coordination to Pb center. This is in accordance with the Pb-O distance (2.53 Å) in the Pb-DMF complex reported by Pang. By comparison, the FT for lead salt exhibits strong features at 3.05 Å and 3.21 Å (after phase-shift correction), which corresponds to Pb-Cl bond Pb-I bond respectively. The evidence strongly suggested that the Pb was coordinated by DMF molecules, rather than Cl or I when it is mixed with MAI in DMF solutions.

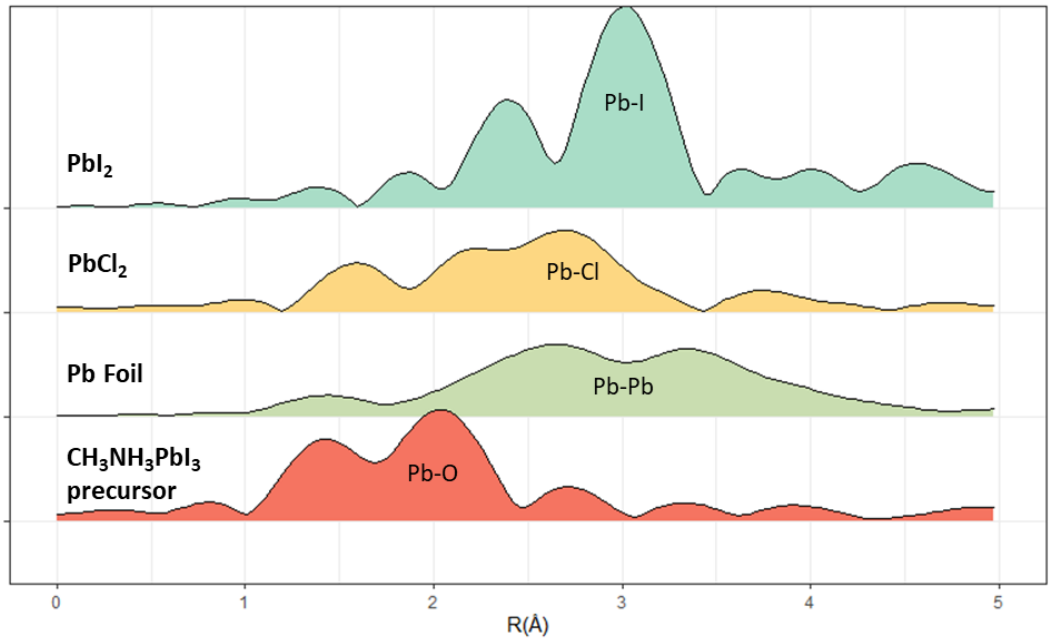

Figure 4.2.2-2. Fourier-transformed EXAFS spectra of PbI_2 (powder), $PbCl_2$(powder), Pb foil and $CH_3NH_3PbI_3$ solution prepared by dissolving $PbCl_2$ (80 mM) and MAI (240 mM) in DMF.

According to the XAS data, we believe **X1** forms in the precursor solution before the spin-coating process starts and crystallizes during the spin-coating process as a result of solvent evaporation or expulsion. As the spin-coating process goes, the excess free DMF solvent is evaporated and the precursor on the substrate changes from unsaturated to ultra-saturated, which results in the crystallization of **X1**. This process can be mimicked by adding an anti-solvent to the precursor solution, which has less solubility for **X1** than DMF. Light-yellow needle-shaped crystals were obtained by using isopropanol (IPA) as the anti-solvent. Single crystal X-ray diffraction analysis showed that the crystals have a formula of $MAPbI_2Cl \cdot DMF$. To explore if any new structures or intermediates can be got by adding different amounts of MACl in the precursor solution, attempts were made to grow crystals from the precursors with $PbCl_2$:MAI as 1:2 and 1:1 by using IPA as the anti-solvent. However, only $MAPbI_2Cl \cdot DMF$ was obtainable, which also proved that $MAPbI_2Cl \cdot DMF$ is quite stable.

The crystal structure of $MAPbI_2Cl \cdot DMF$ is shown in Figure 4.2.2-3. In the structure, each Pb^{II} center coordinates with five I^- and one Cl^- to form an octahedral geometry.

The octahedrons connect with each other by sharing μ-I^- and μ_3-I^- ligands to construct a 1-D $[PbI_2Cl]_n^{n-}$ chain along the crystallographic *a*-axis, while the Cl^- ligands are terminal and locate on two flanks of the chain. The chains interact with each other through Cl···Cl and Cl···H-N-H···Cl interactions to form a layered structure, paralleling *ac*-plane. In between the layers are the solvent DMF molecules, which interact to the two neighboring layers through C-H···I, O···H-N and O···H-C interactions, to stabilize the structure.

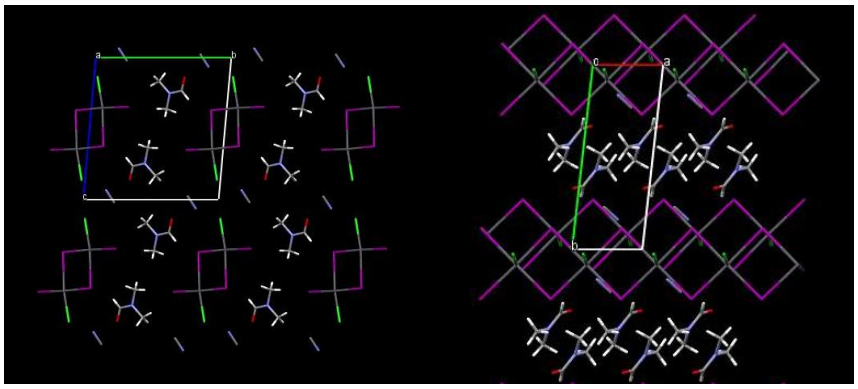

Figure 4.2.2-3. Crystal structure of $MAPbI_2Cl$ ·DMF.

As reported, in the organo-lead-halogen complexes, Pb(II) can coordinate with 4, 5, or 6 atoms to form tetrahedral, square pyramidal, or octahedral coordination geometries，[127-135] and, such Pb(II) coordination units can exist individually, or connect together by sharing ligands to form 1-D chains or 2-D networks, depending on the properties of the ligands and organic cations inside the structures.[53, 127-133, 135] Recently, structures of numerous of Pb-based crystals that relate with perovskite construction have been reported, like PbI_2·DMF, $MAPbI_3$·DMF, $MAPbI_3$·DMSO, and $MAPbI_3$·H_2O, in which all the Pb(II) centers adopt 6-coordinated octahedral geometries.[53, 135] In PbI_2·DMF, the DMF occupies one coordination site, while the Pb(II) centers in all of the other structures are coordinated by six I^- anions to form 1-D $[PbI_3]^-$ chains, which is very similar to the structure of $MAPbI_2Cl$·DMF.

4.2.3 Certification of $MAPbI_2Cl$ ĐMF is the intermediate X1

The calculated XRD patterns from the single crystal structural analysis and the experimental XRD patterns of $MAPbI_2Cl$ ĐMF were firstly compared (Figure 4.2.3-1). Due to the crystallization orientation preference, the experimental XRD patterns of $MAPbI_2Cl$ ĐMF shows fewer peaks than the calculated one. But it is still clear that the calculated and the experimental patterns of $MAPbI_2Cl$ ĐMF are perfectly matched, which can indicate that the $MAPbI_2Cl$ ĐMF powder for further measurement is phase-pure. In fact, by using GIWAXS several groups have shown the crystalline precursor phase of 1:3 $PbCl_2$:MAI that appeared during spin-coating or at the early state of annealing had scattering vector at q = 5, 10, 11 and 12 nm^{-1}. [105, 115, 116, 124] The scattering vector $q = 4\pi \sin\theta/\lambda$, where θ is half of the total scattering angle, and λ is the wavelength of X-ray (0.1161 nm).[124] Therefore, the q values can be equivalent to the XRD diffraction peaks at 2θ = 7.2, 14.4, 15.4 and 17.2°, which highly match those of $MAPbI_2Cl$ ĐMF at 2θ = 7.19-7.53°, 14.35°, 15.61° and 16.81°.

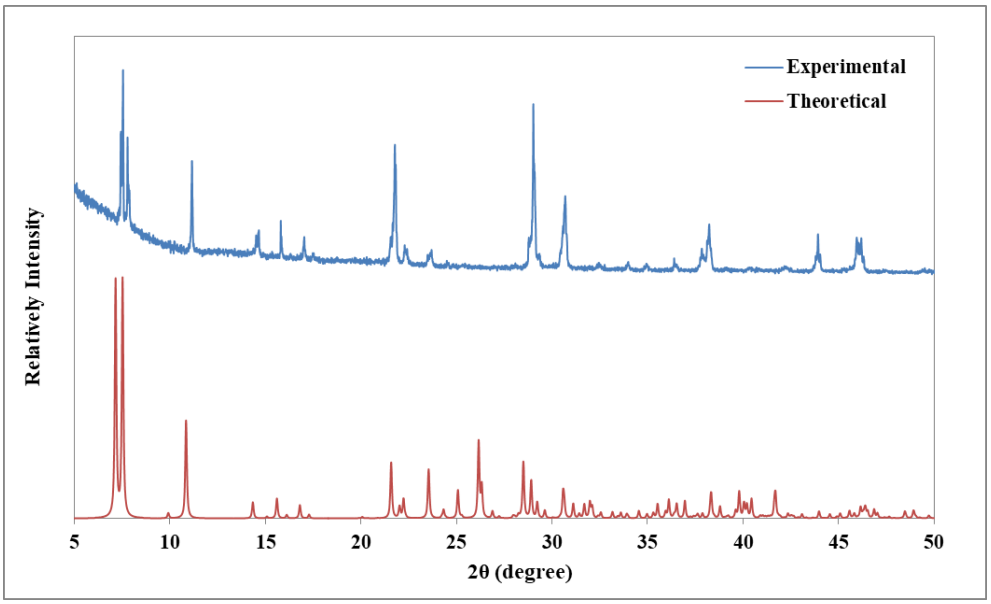

Figure 4.2.3-1. The experimental and calculated X-ray diffraction patterns of $MAPbI_2Cl$ ĐMF.

To further confirm the assumption that $MAPbI_2Cl \cdot DMF$ is probably the crystalline precursor phase **X1**, we then recorded the time dependent X-ray diffraction patterns of the chloride precursor (3:1 $PbCl_2$:MAI) in dry N_2/air and $MAPbI_2Cl \cdot DMF$ crystal powder under thermal annealing at 85 ^oC. Since the as-cast film of chloride precursor changes color very quickly in the air, and is very easy to transform to **X2** and/or perovskite when the solvent is evaporated, attempts to collect the pure sample of **X1** from the substrate failed. In addition, we found the XRD patterns of chloride precursor annealing processes were same no matter in dry N_2 or air (Figure 4.3.3-2). Thus, the XRD patterns of **X1** were recorded directly from the as-cast film on glass substrates in air.

At the early annealing process (0-40 min), the crystalline phase **X1** in chloride precursor film appears and exhibits three strong diffraction peaks at 15.6, 28.7 and 31.6^o, with three weak ones at 16.1, 16.8 and 29.1^o (Figure 4.2.3-2 (A)). Meanwhile, the diffraction peaks at 17.4 and 29.3^o of MACl were observed.[94, 136] The peaks fit very well with the calculated XRD patterns of $MAPbI_2Cl \cdot DMF$ crystals at 15.6, 28.7, 31.6, 16.1, 16.7 and 29.1^o, which belong to the lattice planes $(01\bar{2})$, $(1\bar{3}0)$, (103), $(02\bar{1})$, (012) and $(1\bar{3}\bar{1})$, respectively (Figure 4.2.3-3 (A)). In addition, the phenomena of $MAPbI_2Cl \cdot DMF$ crystals annealing are also similar to those of chloride precursor film, which changes from colorless to red, yellow and dark brown (Figure 4.2.3-3 (B)). Furthermore, we notice that a same phase appears in both XRD patterns of the chloride precursor and the $MAPbI_2Cl \cdot DMF$ powder during thermal annealing. The new phase which has two significant diffraction peaks at 11.2 and 12.0^o should be a decomposition intermediate of $MAPbI_2Cl \cdot DMF$, possibly a low-dimensional iodide-rich perovskite phase.

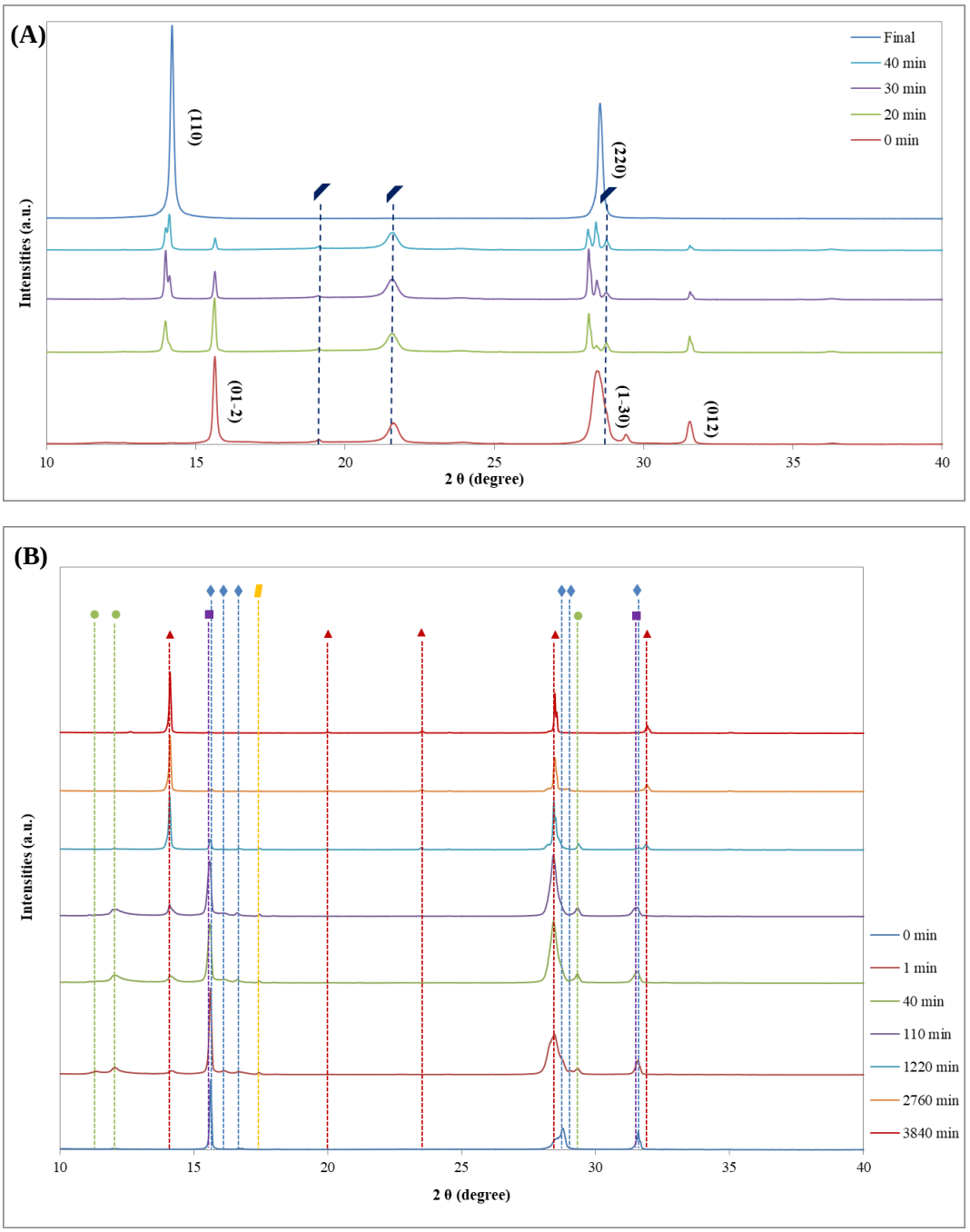

Figure 4.2.3-2. Time dependent X-ray diffraction patterns of (A) the chloride precursor (3:1 $PbCl_2$:MAI) under thermal annealing at 85 ^oC in dry N_2 (deep blue trapeziums are backgrounds), (B) the chloride precursor (3:1 $PbCl_2$:MAI) under thermal annealing at 85 ^oC in air. Key reflections attributed to the intermediate **X1** (blue diamonds), intermediate (green circles), MACl (yellow parallelograms), $MAPbCl_3$ (purple squares), and perovskite (red triangles) phases are indicated.

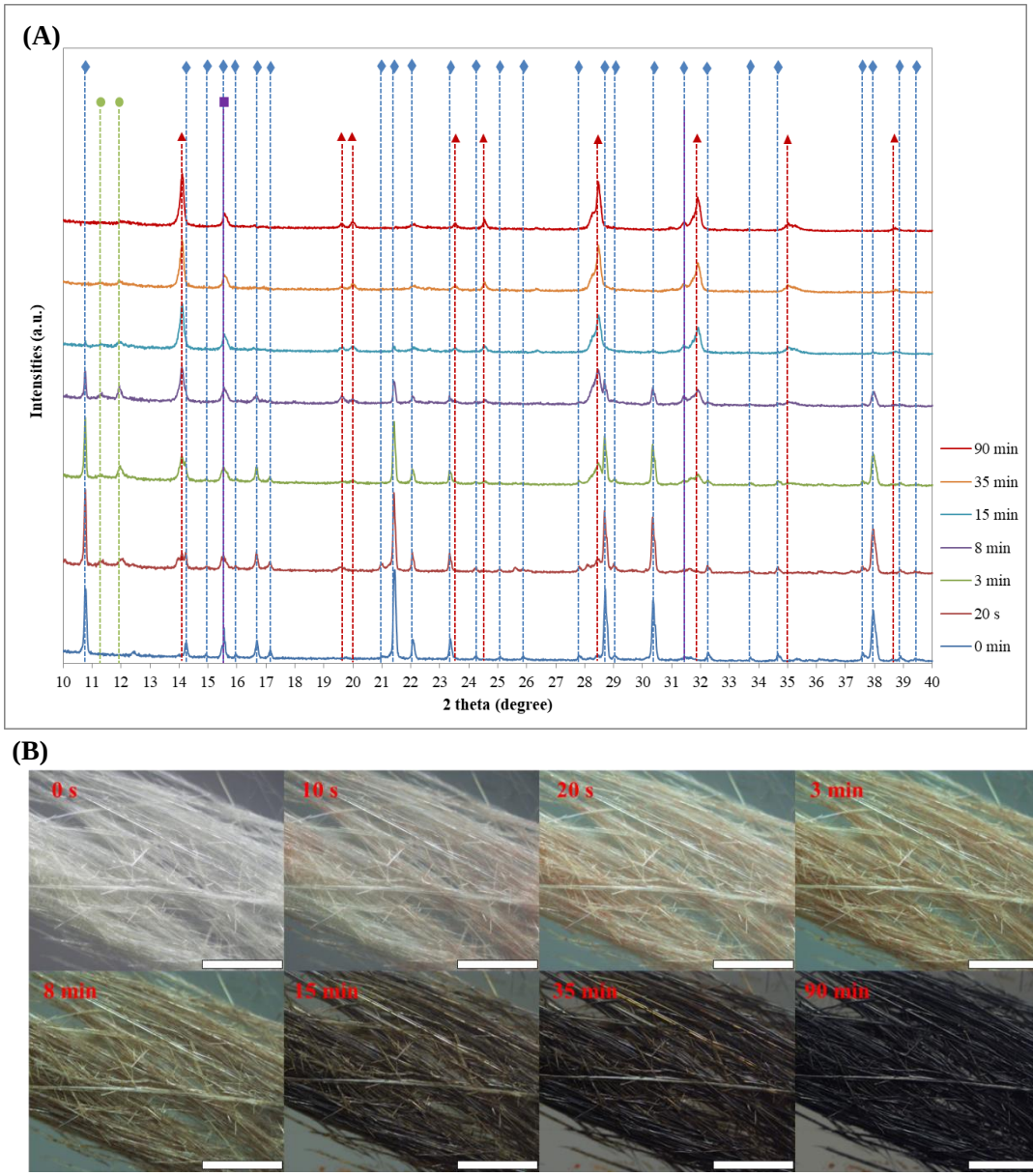

Figure 4.2.3-3. (A) $MAPbI_2Cl$ ĐMF crystal powder under thermal annealing at 85 ^oC. Key reflections attributed to the $MAPbI_2Cl$ ĐMF (blue diamonds), intermediate (green circles), $MAPbCl_3$ (purple squares), and perovskite (red triangles) phases are indicated. (B) The microscope images of $MAPbI_2Cl$ ĐMF annealing process at 85 ^oC. The scale bars correspond to 100 μm in length.

The less number of XRD peaks on the diffraction patterns of **X1** can be considered as a result of the preferred crystallographic orientation of the film. We observed that during spin-coating and at the early state of annealing the precursor film was firstly turn to bright yellow and then brown, thus we supposed the intermediate **X1**

underwent a recrystallization process. To prove our supposition, we heated the $MAPbI_2Cl \cdot DMF$ crystals with mother solution at a low temperature at 65 ^oC, the results are shown in Figure 4.2.3-4.

Obviously, the $MAPbI_2Cl \cdot DMF$ crystals dissolve in the mother solution firstly under annealing, and then recrystallize to form some tiny grains (Figure4.2.3-4 (B)). According to the XRD patterns (Figure4.2.3-4 (A)), this process produces a highly crystallized phase which has same XRD peaks with those of the as-cast precursor film. In addition, under microscope we find the tiny grains have same geometry shape with the crystals on the as-cast precursor film (Figure 4.2.3-4 (C)). In the same time, we also notice some other bulk crystals appear, and single-crystal X-ray diffraction shows they are $MAPbCl_3$. Considering the $MAPbCl_3$ crystals have high orientation, they may play roles of template for the tiny grains to grow. In addition, the FT-IR spectra of $MAPbI_2Cl \cdot DMF$ crystals before and after recrystallization are same, which indicates the coordination environment of Pb^{2+} has no change (Figure 4.2.3-5). Thus, we believe the tiny grains are some recrystallized $MAPbI_2Cl \cdot DMF$ crystals with high orientation, and the high orientation of perovskite film fabricated from chloride precursor is also caused by the $MAPbCl_3$ templates which is formed from the recrystallization process of $MAPbI_2Cl \cdot DMF$ crystals.

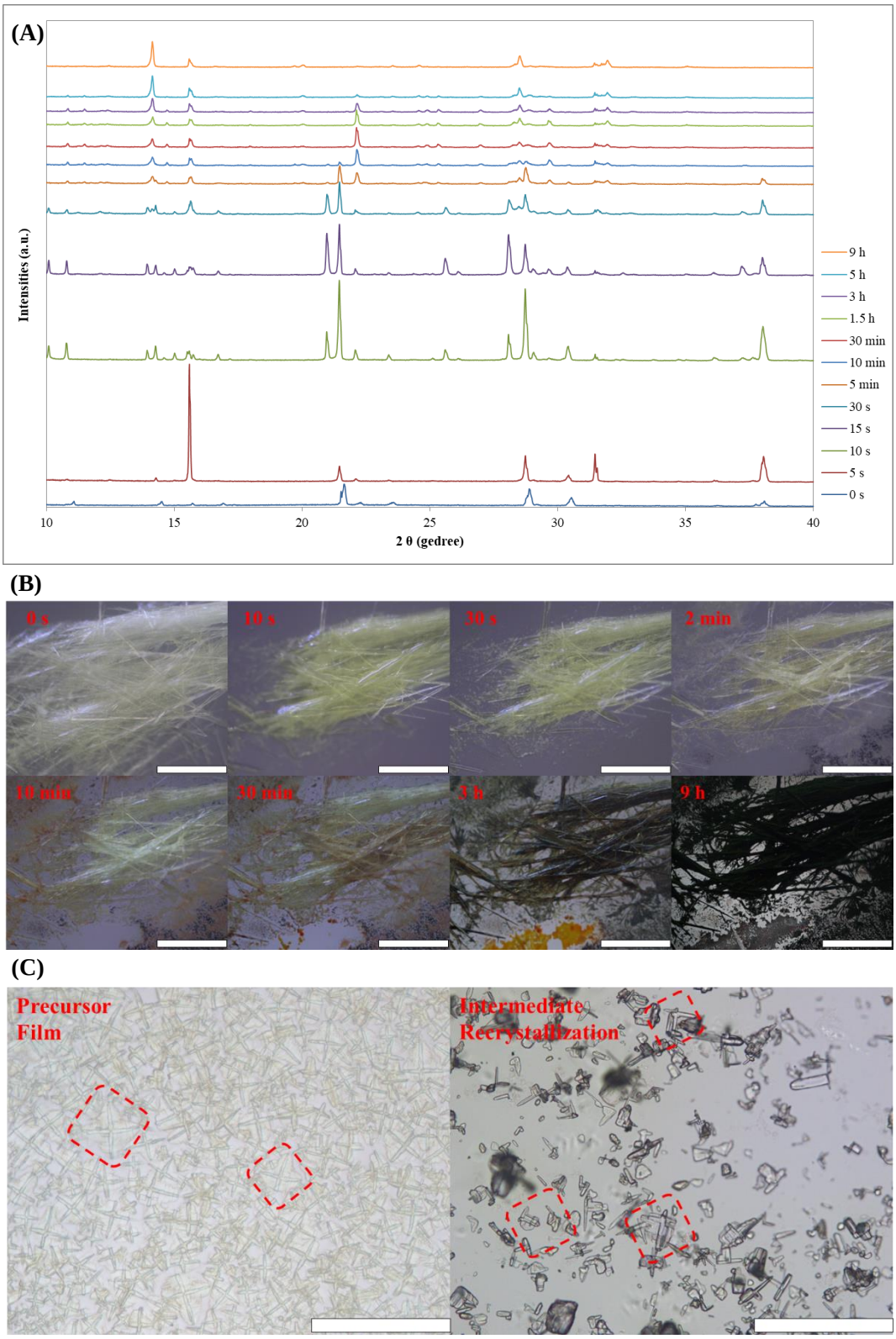

Figure 4.2.3-4. (A) The XRD patterns and (B) microscope images of $MAPbI_2Cl$ ·DMF recrystallization process at 65 °C. (C) The microscope images of precursor film and $MAPbI_2Cl$ ·DMF crystals after recrystallization. The scale bars correspond to 100 μm in length.

HR-TEM is another efficient instrument to identify the crystalline components in the precursor film. By calculating the d-spacing values of crystals on the precursor film, we observed several lattice plains of $MAPbI_2Cl \cdot DMF$, which contain (0-41), (024), (0-33) and (2-12) (Figure 4.2.3-6 and Table 4.2.3). According to discussed above, here we prove that the crystalline precursor phase **X1** is $MAPbI_2Cl \cdot DMF$, and we can continue to discovery the structure of **X2** based on $MAPbI_2Cl \cdot DMF$.

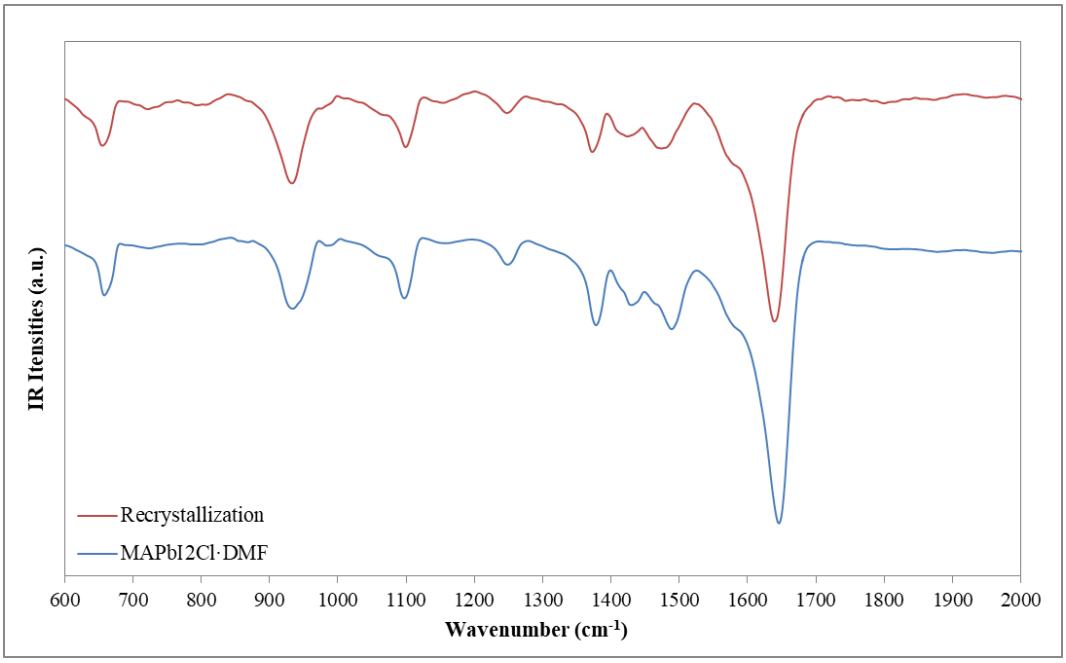

Figure 4.2.3-5. FT-IR spectra of $MAPbI_2Cl \cdot DMF$ crystals before and after recrystallization.

Table 4.2.3 d-spacing and lattice plains in HR-TEM images of as-cast chloride precursor film before annealing.

d-spacing	**Lattice plain**
2.03 Å	$MAPbI_2Cl \cdot DMF$ (2-12)
2.63 Å	$MAPbI_2Cl \cdot DMF$ (024)
2.91 Å	$MAPbI_2Cl \cdot DMF$ (0-41)
2.97 Å	$MAPbI_2Cl \cdot DMF$ (0-33)
4.49 Å	MAI (002)

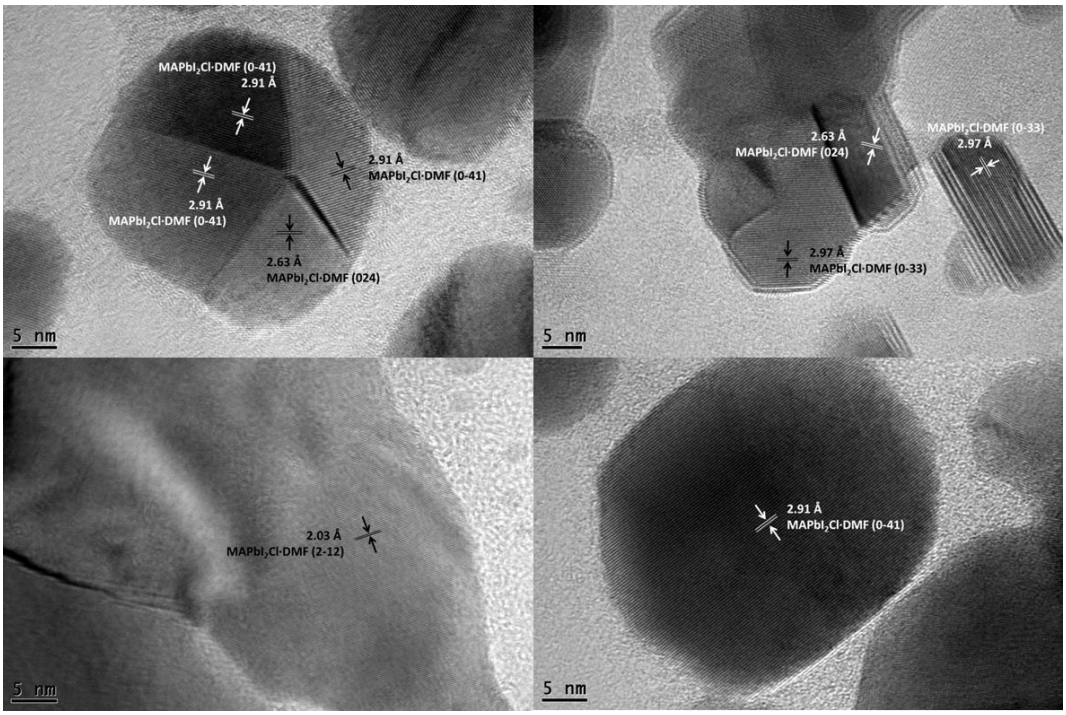

Figure 4.2.3-6. HR-TEM images of as-cast chloride precursor film before annealing. The d-spacing and lattice plains were assigned in the figures.

4.2.4 Identification of X2 using techniques of XRD, HR-TEM, IR and Raman spectroscopies

To identify the **X2**, we underwent the thermal decomposition process of $MAPbI_2Cl$·DMF crystals with mother solution at 65°C. Usually, for precursor $PbCl_2$/MAI (1:3), the thermal annealing temperature adopted is 95°C.[64, 94, 137, 138] The temperature of 65°C was chosen for the experiment because we want the process to be slow enough to be monitored by lab techniques. Our experiment showed that, at 65°C, the colorless crystals of $MAPbI_2Cl$·DMF became red color immediately, which is stable up to t = ~ 5 min (Figure 4.3.3-4 (A and B)). The elemental analysis of the new phase indicated that it has a formula of $MAPbI_2Cl$ with 2% of remained crytsalline DMF, with calculated values (%) as C: 2.400, N: 2.694, H: 1.159; and the found values (%) as C: 2.490, N: 2.596, H: 1.099. The experimental C amount was found slightly higher than the theoretical one, while the N and H amount was found slightly lower. This should be caused by the remained crystalline DMF in sample after the short time annealing, which was used to prevent the further decomposition of the unstable intermediate **X2**. The organic component of $MAPbI_2Cl$ has a formula of CH_3NH_3, and the formula of DMF was C_3H_7NO. Thus, the higher C percentage in the mixture of $MAPbI_2Cl$ and $MAPbI_2Cl$·DMF should lead the elemental analysis show the experimental data with higher C percentage but lower N or H percentage. In addition, as previously reported, the perovskite-solvent complexes preferred to disconnect the solvent molecules during annealing, like $MAPbI_3$·DMF decomposed to $MAPbI_3$ and DMF at the first step of annealing.[53] Therefore, the second intermediate X2 should be the decomposition product of $MAPbI_2Cl$·DMF, which had the formula of $MAPbI_2Cl$.

Subsequently, to show the phase is not a mixture of $MAPbI_3$ and $MAPbCl_3$, it was characterized by FT-IR, Raman and UV-Vis spectroscopies (Figure 4.2.4-1). In FT-IR spectra, the peaks at about 970 cm^{-1} and 910 cm^{-1} belong to C-N stretching and rocking modes, respectively.[139] Obviously, the C-N stretching of $MAPbI_2Cl$ had only

one peak and located between the other two perovskites. The appeared two rocking peaks should be caused by iodide and chloride ions inside compound. For the Raman spectra, though the absorptions are not clear so far, the peak positions and curve shape of $MAPbI_2Cl$ was totally different from the other two.[140] According to the UV-Vis spectra, the absorption edge of $MAPbI_2Cl$ was a little shorter than $MAPbI_3$, and in the low-energy area all the three samples were different. Therefore, the results indicated that $MAPbI_2Cl$ was not a mixture of $MAPbI_3$ and $MAPbCl_3$. In addition, Cao *et al.* used UV-Vis and XRD to monitor the annealing process of chloride precursor, and they also proved the existence of $MAPbI_2Cl$.[117]

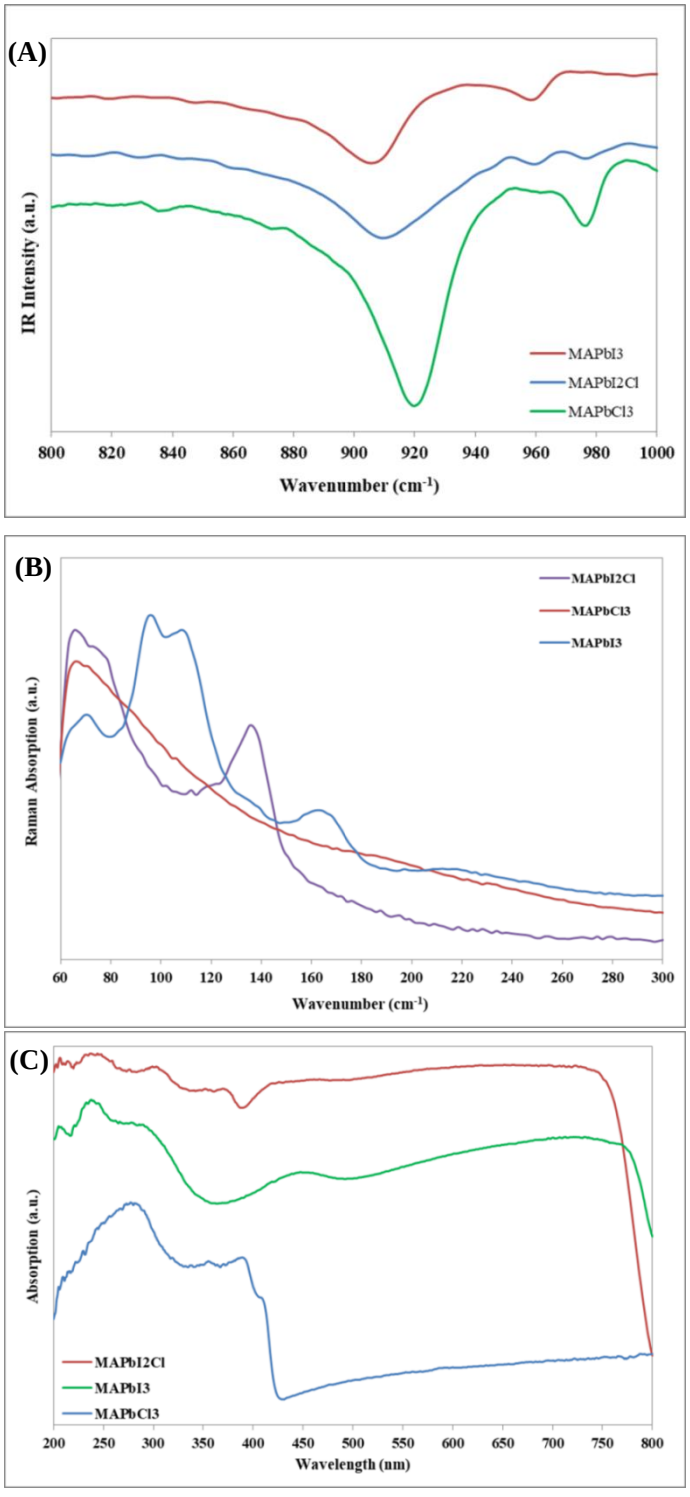

Figure 4.2.4-1. (A) FT-IR, (B) Raman, and (C) UV-Vis spectra of $MAPbI_2Cl$, $MAPbI_3$ and $MAPbCl_3$.

We then simulate and optimize the structure of $MAPbI_2Cl$ by removing crystalline DMF from $MAPbI_2Cl \cdot DMF$, the theoretical XRD patterns is shown in Figure 4.2.4-2. Surprisingly, all the new peaks appear in the XRD patterns of $MAPbI_2Cl \cdot DMF$ annealing process at 65°C, which locate at 14.0, 21.1, 25.2, 26.3, 28.2, 29.9, 32.7 and 37.7°, can be found in that of $MAPbI_2Cl$. In addition, according to the HR-TEM images (Figure 4.2.4-3 and Table 4.2.4), we truly observed the lattice plains of $MAPbI_2Cl$, also with other decomposition compounds like $MAPbI_3$ and $MAPbCl_3$. Now all the analyses prove the second intermediate phase **X2** is a mixed-halide perovskite $MAPbI_2Cl$.

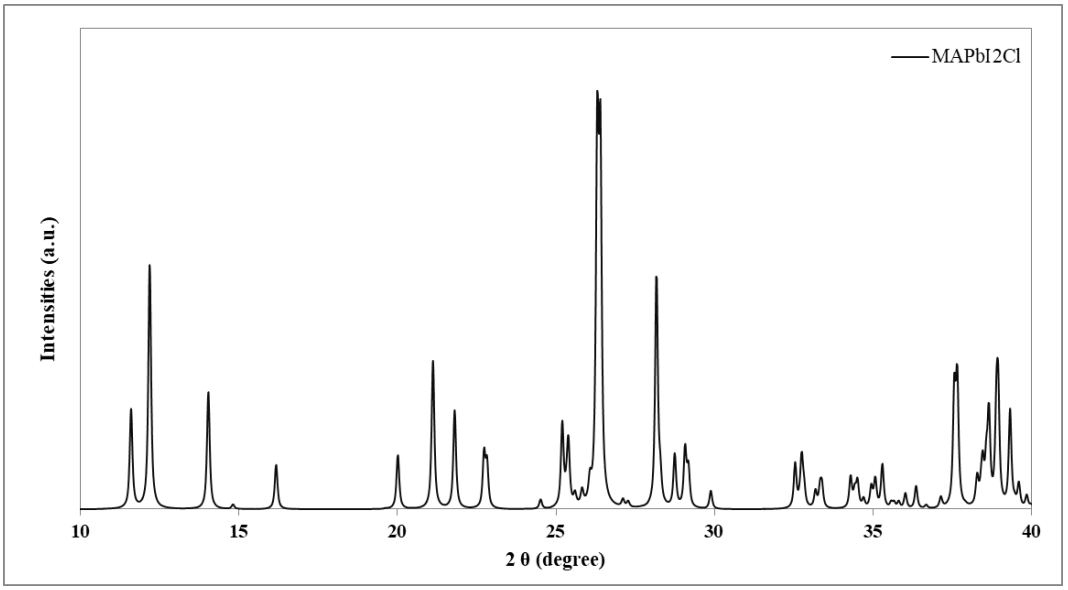

Figure 4.2.4-2. Calculated XRD patterns of $MAPbI_2Cl$ at the range from 10° to 40°.

Table 4.2.4 d-spacing and lattice plains in HR-TEM images of as-cast chloride precursor film during annealing.

d-spacing	**Lattice plane**
2.12 Å	$MAPbI_3$ (233)
2.37 Å	$MAPbI_2Cl$ (114)
2.63 Å	$MAPbI_2Cl$ ĐMF (024)
2.91 Å	$MAPbI_2Cl$ ĐMF (0-41)
3.15 Å	$MAPbI_2Cl$ (004)
3.41 Å	$MAPbI_2Cl$ (111)
3.97 Å	$MAPbCl_3$ (202)

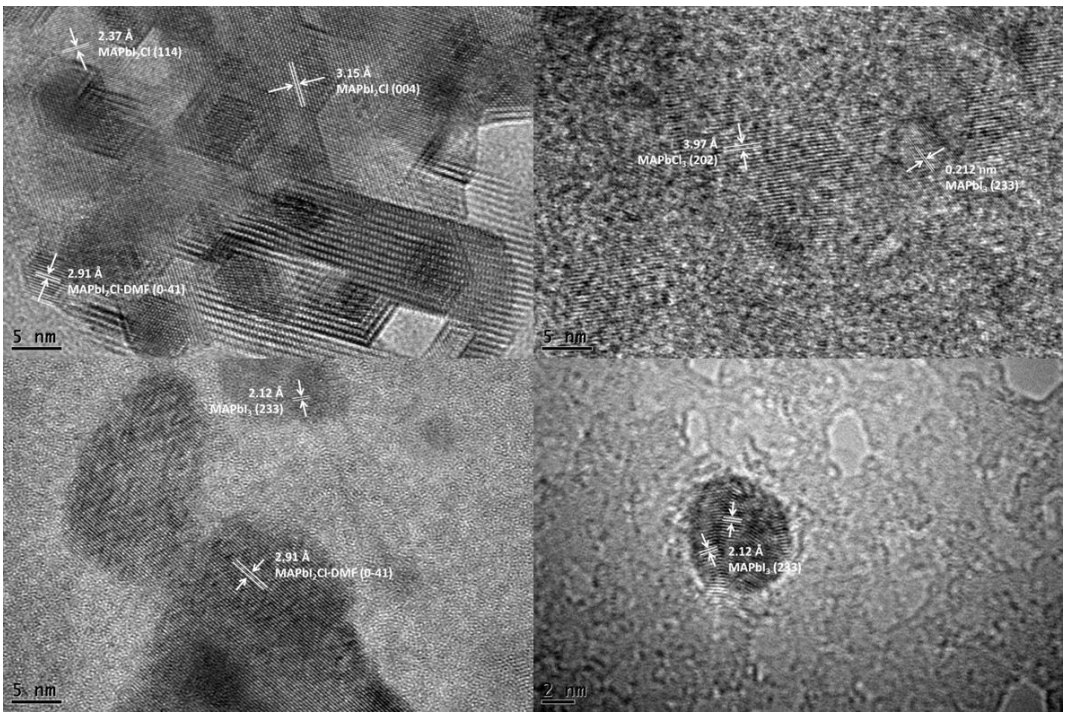

Figure 4.2.4-3. HR-TEM images of as-cast chloride precursor film during annealing. The d-spacing and lattice plains were assigned in the figures.

4.2.5 Perovskite film formation mechanism from precursor $PbCl_2$/MAI (1:3)

To deeply understand the transformation from $MAPbI_2Cl$ to $MAPbI_3$, we then studied the thermal behavior of $MAPbI_2Cl \cdot DMF$ at temperature from 25 to 300 ^oC. Because the $MAPbI_2Cl \cdot DMF$ sample contains large numbers of tiny villous crystals. Although the sample is dried after being washed with DMF/IPA mixture, some solvent still remains inside. Therefore, the first step of mass loss for $MAPbI_2Cl \cdot DMF$ is the evaporation of mixed solvent DMF/IPA and crystalline DMF, and the remained mass of 38.9% belongs to $MAPbI_2Cl$. When the temperature keeps at 100 ^oC, the mass does not change. The second step of decomposition starts from 180^oC and loses mass of 9.2%, which occupies 23.6% of $MAPbI_2Cl$ and equals to the mass of 2/3 MAI and 1/3 MACl (cal. 24.3%). This phenomenon can be explained by that the $MAPbI_2Cl$ is not stable at 100 ^oC, but transforms to $MAPbI_3$ and $MAPbCl_3$. The same result can be obtained according to the XRD patterns of $MAPbI_2Cl \cdot DMF$ crystal powder under thermal annealing (Figure 4.2.3-3 (A)), where at the final stage of the annealing process the diffraction peaks of $MAPbI_3$ and $MAPbCl_3$ coexist. Furthermore, if the temperature is up to 300 ^oC, $MAPbI_3$ and $MAPbCl_3$ will decompose to PbI_2 and $PbCl_2$, respectively.

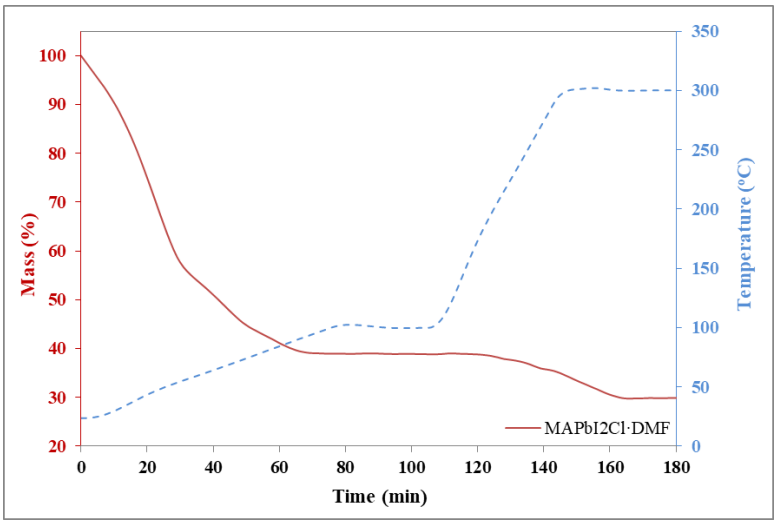

Figure 4.2.5-1. Time dependent TGA curve of $MAPbI_2Cl \cdot DMF$ powder.

Considering the common annealing temperature (95 ^{o}C) for the chloride precursor is much lower than the decomposition temperatures of $MAPbI_3$ (240 ^{o}C) and $MAPbCl_3$ (214 ^{o}C), $MAPbCl_3$ will instead to react with remained MAI to form $MAPbI_3$, while MACl will escape as gas form.[136] This result is consistent with the XRD patterns of the chloride precursor (Figure 4.2.3-2 (A)), that during the annealing process no diffraction peak of PbI_2 or $PbCl_2$ is observed. Zhao *et al.* also found that if the as-cast film was covered with PMMA, the perovskite phase would not completely form, which indicates the leaving of MACl was an important driving force for $MAPbI_3$ formation.[94] Therefore, the transformation from $MAPbI_2Cl$ to $MAPbI_3$ is not a single step reaction, but contains the decomposition of $MAPbI_2Cl$ and the reaction between $MAPbCl_3$ and MAI. It is the reaction between $MAPbCl_3$ and MAI that significantly retard the crystallization rate of perovskite, which is the reason of producing the perovskite film with high quality.

In conclude, the formation of perovskite from precursor (1:3 $PbCl_2$:MAI) should contain reaction equations shown below:

(1) *Spin-coating*: $PbCl_2 + 3MAI + DMF \rightarrow MAPbI_2Cl \cdot DMF + MACl + MAI$
(2) *Recrystallization*: $MAPbI_2Cl \cdot DMF \rightarrow (1\text{-}x)\ MAPbI_2Cl \cdot DMF + x\ MAPbCl_3$
(3) *Annealing*: $MAPbI_2Cl \cdot DMF \rightarrow MAPbI_2Cl$ (intermediate) + DMF (g)
(4) *Annealing*: $MAPbI_2Cl \rightarrow 2/3\ MAPbI_3 + 1/3\ MAPbCl_3$
(5) *Annealing*: $1/3\ MAPbCl_3 + MAI \rightarrow 1/3\ MAPbI_3 + MACl$ (g)

The reaction equations (1) to (5) represent the formation of $MAPbI_2Cl \cdot DMF$ intermediate in as-cast film, the recrystallization of intermediate during spin-coating and annealing, the evaporation of crystalline DMF from intermediate, the decomposition of $MAPbI_2Cl$ to perovskite and $MAPbCl_3$, and the reaction between $MAPbCl_3$ and MAI to form perovskite, respectively.

In addition, the activation energy E_a of perovskite formation from chloride precursor was calculated according to Avrami-Erofeev analysis (1), the Sharp-Hancock presentation (2), and Arrhenius relation (3), where $\alpha(t)$ represents the ratio of diffraction peak intensities at time t to initial time t_0; k represents the rate constant; n is the Avrami exponent; and R is the gas constant.

(1) $\alpha(t) = 1 - \exp\{-[k(t-t_0)]n\}$

(2) $\ln\{-\ln[1 - \alpha(t)]\} = n \ln(t - t_0) + n \ln k$

(3) $\ln(k(T)) = -E_a/(RT) + \text{constant}$

XRD was used to monitor the perovskite formation process, and the time-dependent diffraction intensities of perovskite (110) lattice plain were used to calculate $\alpha(t)$ and $k(T)$ according to the Sharp-Hancock presentation. The same calculations were done at three temperatures of 80°C, 90°C and 100°C to build the Arrhenius relation. The original data and calculation processes were shown in Table 4.2.5 and Figure 4.2.5-2, respectively. The calculated activation energy E_a equals to 71.546 kJ/mol, which is closed to the reported value of 72 ± 11 kJ/mol.[99]

Table 4.2.5 Time-dependent diffraction intensities of perovskite (110) plane at different temperatures

80 °C		**90 °C**		**100 °C**	
t (s)	Intensity (a.u.)	t (s)	Intensity (a.u.)	t (s)	Intensity (a.u.)
0	176	0	200	0	200
60	881	30	1745	10	936
180	873	60	2538	25	1920
780	1042	90	3047	60	2560
2400	1874	180	3623	120	2677
6600	3009	480	3930	300	2766
55200	12632	1080	4132	900	3767
73200	13151	2880	5071	2700	4842
82200	13734	6480	5933	14700	5873
230400	14769	13680	8664	68700	15702
		64080	11169	90300	15871
		83880	11715		
		147480	11987		

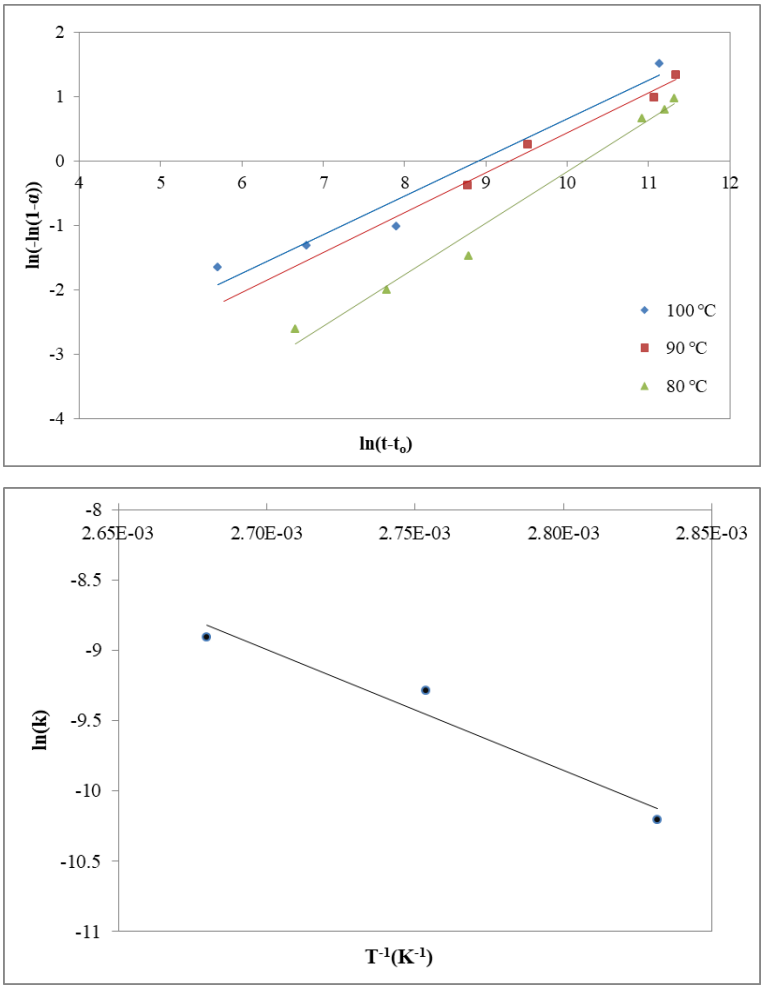

Figure 4.2.5-2. Avrami-Erofeev analysis and Arrhenius relation

4.2.6 Mechanism of perovskite formation from iodide precursors

The precursor PbI_2/MAI (1:1) was the most initial precursor used for perovskite fabrication, while precursor PbI_2/MAI (1:3) was developed later on to improve the morphology of perovskite film and efficiency of perovskite solar cells.[108, 109, 141-143] To understand the differences between the two precursors, we continued using *in situ* microscope to monitor the crystallization of precursors on substrates under thermal annealing. The formation processes of perovskite from precursors PbI_2/MAI (1:1) and PbI_2/MAI (1:3) are shown in Figure 4.2.6-1.

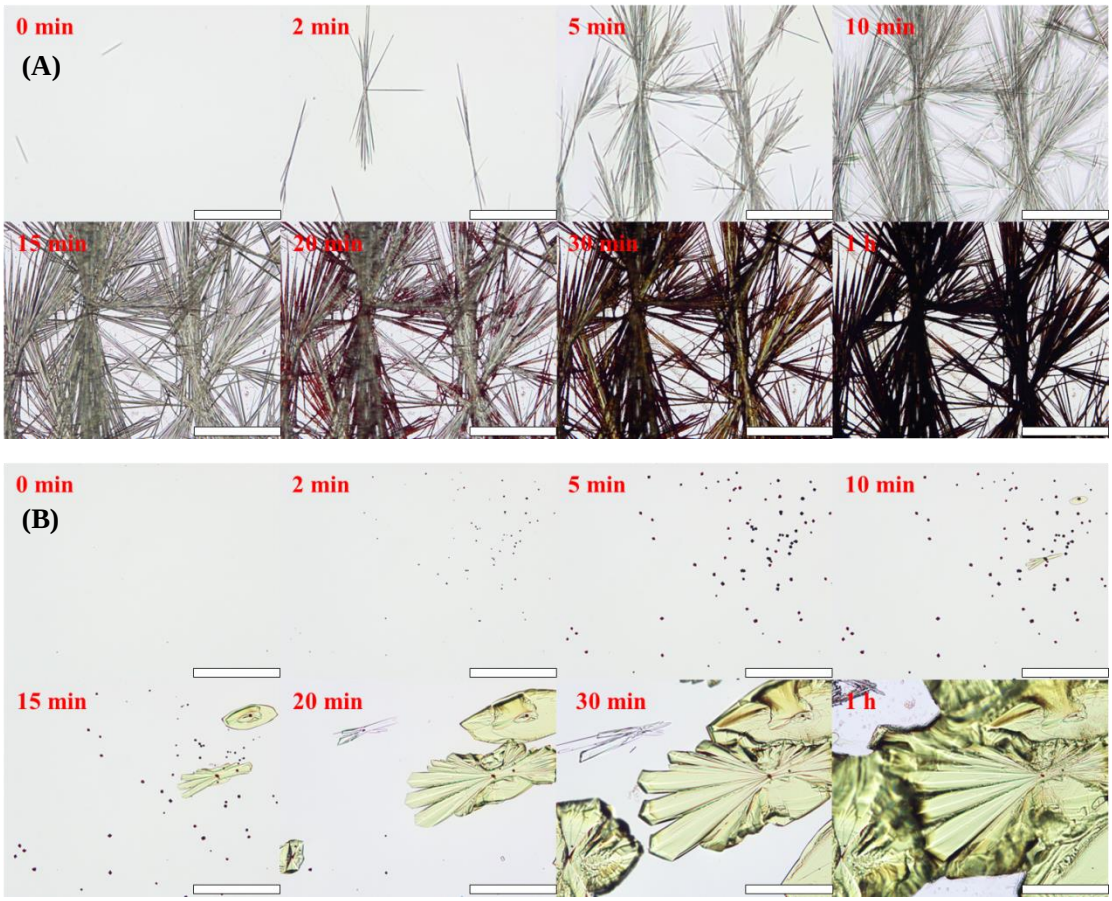

Figure 4.2.6-1. The *in situ* microscope images of perovskite formation process. The scale bars correspond to 100 μm in length.

For PbI_2/MAI (1:1) (Figure 4.2.6-1 (A)), clearly, the whole process can be separated into three stages (**S1** - **S3**). The first stage **S1** (1 - 15 min) is the crystallization of intermediate **Y1** from liquid phase, where light-yellow needle-shaped crystals appear and grow around several "nuclei". For the **S2** (15 - 20 min), some parts of the needle-shaped crystals started to change from yellow to purple-red. Then at **S3** all the crystals gradually transform to black color, which indicates the formation of perovskite $MAPbI_3$ is complete. Therefore, for the conventional one-step method, during spin-coating the solvent rapidly evaporates from liquid film, while the intermediate **Y1** crystallizes to form a wet as-cast film. During thermal annealing, the free DMF solvent evaporate from the wet film, and the intermediate decomposes to

form perovskite. For precursor PbI_2/MAI (1:3), as shown in Figure 4.3.6-1 (B), the crystallization process was completely different. We can see that some dark-brown crystals showed up at t = 2 min, and became bigger by t = 5 min, but stop growing at t = 5 to 10 min, with the appearance of a few leaf-shaped crystals of intermediate **Z1** around some of the dark-brown crystals formed earlier. From t = 15 to 60 min, the dark-brown crystals started to disappear and the leaf-shaped **Z1** grew very fast to become big blocks. At last, the substrate is covered by the light-yellow highly crystalline intermediate **Z1**.

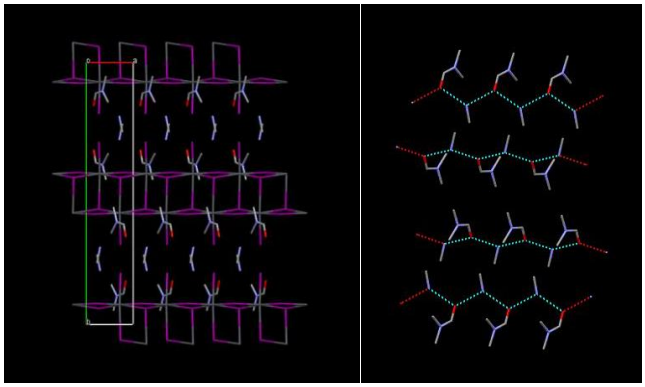

Figure 4.2.6-2. Crystal structure of $MAPbI_3$·DMF.

X-ray crystal structural analysis showed that **Y1** and **Z1** are $MAPbI_3$·DMF and MA_3PbI_5·DMF, which is consistent with the results reported by Kanatzidis and Tarasov, respectively.[53, 143] $MAPbI_3$·DMF (Figure 4.2.6-2) is the first identified intermediate in perovskite formation process, which exists in precursor as micelles and crystallizes during spin-coating.[144] Obviously, the two precursors underwent different routes to form perovskite, the improved coverage of MA_3PbI_5·DMF film was the key that led to the better performance of devices.[145]

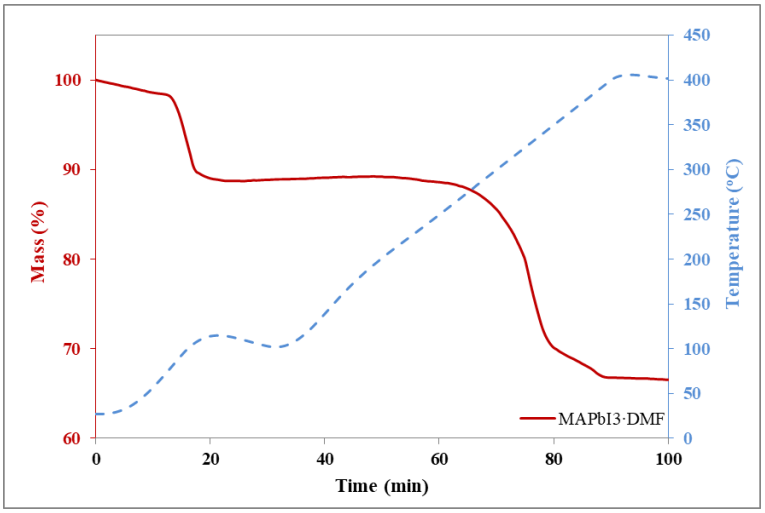

Figure 4.2.6-3. TGA of crystalline $MAPbI_3$·DMF.

As shown in Figure 4.2.6-3, clearly, the intermediate $MAPbI_3$·DMF firstly undergoes a fast decomposition starting from 65°C with a mass loss of 11%, which should be the evaporation process of crystalline DMF from $MAPbI_3$·DMF (cal. 10.55%). The second step of decomposition happens at 244°C, which is followed by the third step happening at 334°C. The mass loss of the two steps is 18% and 4.3%, respectively, which equals to the mass of HI (cal. 18.5%) and MA (cal. 4.6%). This behavior has been explained by Liu *et al*., which is caused by the incorporation of MA^+ cations in the crystal.[136]

Therefore, based on the microscope images, XRD patterns, and TGA analysis discussed above, the formation process of perovskite from precursor PbI_2/MAI(1:1) is now clear. It is crystallization and transformation process of intermediate, and the reaction equations should be:

(2-1) PbI_2 + MAI + DMF → $MAPbI_3$ DMF (solvate)

(2-2) $MAPbI_3$ DMF (solvate) → $MAPbI_3$ DMF (s)

(2-3) $MAPbI_3$ DMF (s) → $MAPbI_3$ (s) + DMF (g)

The reaction equations (2-1), (2-2) and (2-3) represent the formation of intermediate in precursor, the crystallization of intermediate during spin-coating, and the transformation of intermediate to perovskite under thermal annealing, respectively.

4.2.7 The comparison of intermediates containing different halide ions

Similarly, single crystals were grown from the precursor [$PbBr_2$ + 3MAI], which has formula of $MAPb_{1.5}I_3Br \cdot DMF$. According to Figure 4.2.7-1, the framework of $MAPb_{1.5}I_3Br \cdot DMF$ is still constructed of inorganic chains, however, the chains here is triple-chains. The triple-chains are formed of two types of Pb^{II} octahedrons, one is [PbI_6] and the other is [PbI_5Br]. In detail, the octahedrons [PbI_5Br] and [PbI_6] connect with each other with μ-I and μ_3-I ligands to form 1-D $[Pb_3I_6Br_2]^{2-}$ triple-chains, while the Br^- ligands are terminal just like Cl^- ligands in $MAPbI_2Cl \cdot DMF$. In addition, the chains also grow through the crystallographic c-axis and crosswise arrange like $MAPbI_3 \cdot DMF$, and MA^+ cations with DMF molecules stay around the chains. Similarly, MA^+ cations neutralize the negative charges of the $[Pb_3I_6Br_2]^{2-}$ chains, and form H-bonds [N-H---O] with DMF to provide extra stability to the crystal structure.

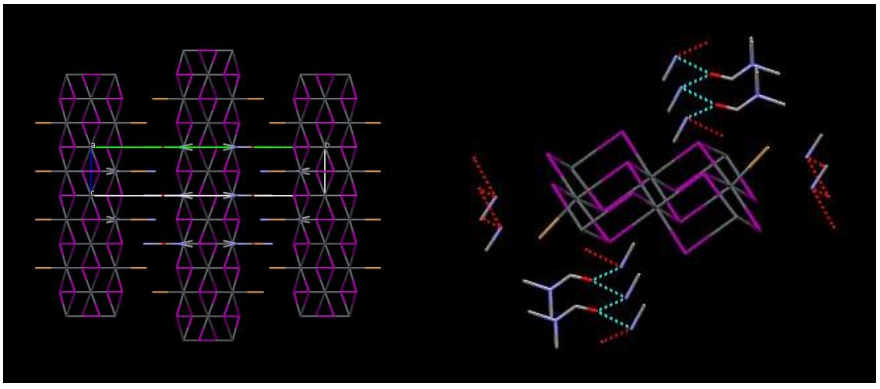

Figure 4.2.7-1. The crystal structure of $MAPb_{1.5}I_3Br \cdot DMF$.

As same as $MAPbI_2Cl \cdot DMF$, the sample of $MAPb_{1.5}I_3Br \cdot DMF$ also contains lots of solvent inside, so the first decomposition process should be separated into the evaporation of solvent and crystalline DMF. According to the slope change in TGA

and the peak position in DTA, the mass loss of solvent should be 32.34% and the mass of remained $MAPb_{1.5}I_3Br \cdot DMF$ is 67.66%. Therefore, the escape of DMF happens at 103°C, and the mass loss is 5.61%, which occupies 8.3% of $MAPb_{1.5}I_3Br \cdot DMF$ (cal. 8.33%). In addition, the third step of decomposition should belong to MABr, which has a mass loss of 10.2% and occupies 14.8% of $MAPb_{1.5}I_3Br \cdot DMF$ (cal. 12.8%).

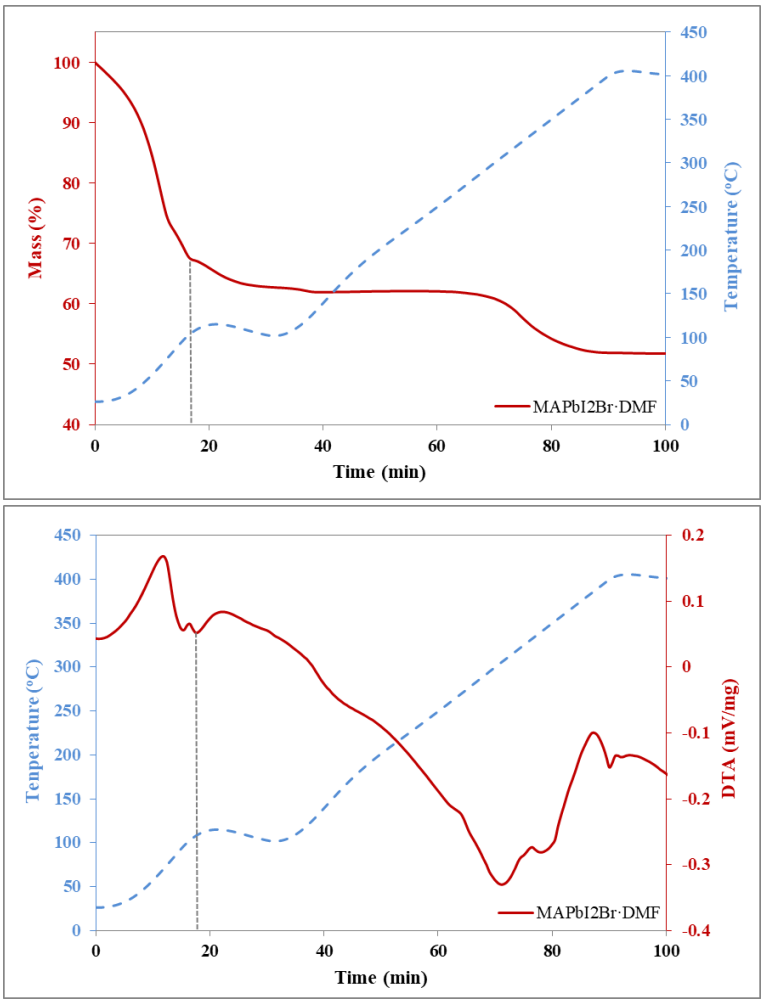

Figure 4.2.7-2. TGA and DTA of $MAPb_{1.5}I_3Br \cdot DMF$.

The UV-Vis spectra are used to determine the absorption properties of the three intermediates, and the results are shown in Figure 4.2.7-3. Obviously, the absorptions of all the three intermediates are only limited at short-wavelength range, which is consistent with their light yellow color. In detail, the absorption range of

$MAPbI_3$·DMF starts from about 470 nm, while the other two start from about 460 nm. In addition, the absorption peak of $MAPbI_3$·DMF appears at 379 nm, which is higher than that of $MAPbI_2Cl$·DMF (353 nm) and $MAPb_{1.5}I_3Br$·DMF (355 nm). This observation should be caused by the coordinated chloride and bromide anions in the intermediates, which produce influence on the band structures.

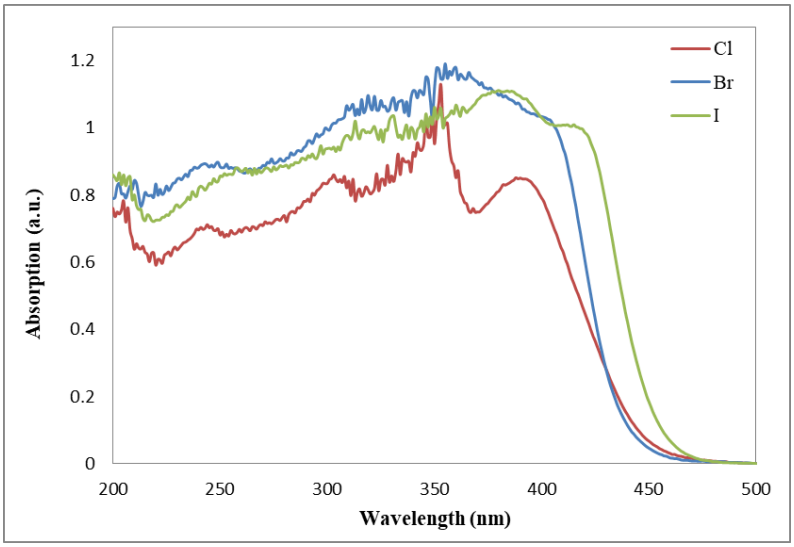

Figure 4.2.7-3. UV-Vis spectra of $MAPbI_3$·DMF, $MAPbI_2Cl$·DMF, and $MAPb_{1.5}I_3Br$·DMF.

The FTIR spectra of DMF solvent and three intermediates are shown in Figure 4.2.7-4. Clearly, the characteristic absorption bands that belong to DMF are located at 661 cm^{-1}, 1099 cm^{-1}, 1255 cm^{-1}, 1390 cm^{-1}, and 1668 cm^{-1}, which can be assigned to N-C=O benidng [δ(N-C=O)], methyl rocking [ρ(CH_3)], asymmetric C-N stretching [ν_a(C-N)], combination of N-C-H bending [δ(N-C-H)] and C-N stretching [ν(C-N)], and carbonyl stretching [ν(C=O)] vibrational modes, respectively.[105, 146] In the FTIR spectra, the absorption bands belonged to DMF are identified in all the three intermediates but shift from their original positions, which indicates the DMF molecules exist in the intermediates as crystalline form. Among them, [δ(C=O)] and [ρ(CH_3)] blue-shift, while the other three, [ν_a(C-N)], combination [δ(N-C-H)] and [ν(C-N)], and [ν(C=O)] red-shift. Commonly, the shifts of vibrational bands could be caused by intramolecular or intermolecular interactions.[105] According to the special

crystal structures of intermediates, this phenomenon can be reasonably explained by the influences of intermolecular forces on crystalline DMF molecules, which include the H-bonds between DMF and MA^+ [O---H-N] and the van der Waals forces between DMF and inorganic chains [C-H---I]. The identification and shifts of absorption bands assigned to DMF in intermediates which are observed in FTIR spectra strongly agree the structure information gained from single crystal X-ray diffraction.

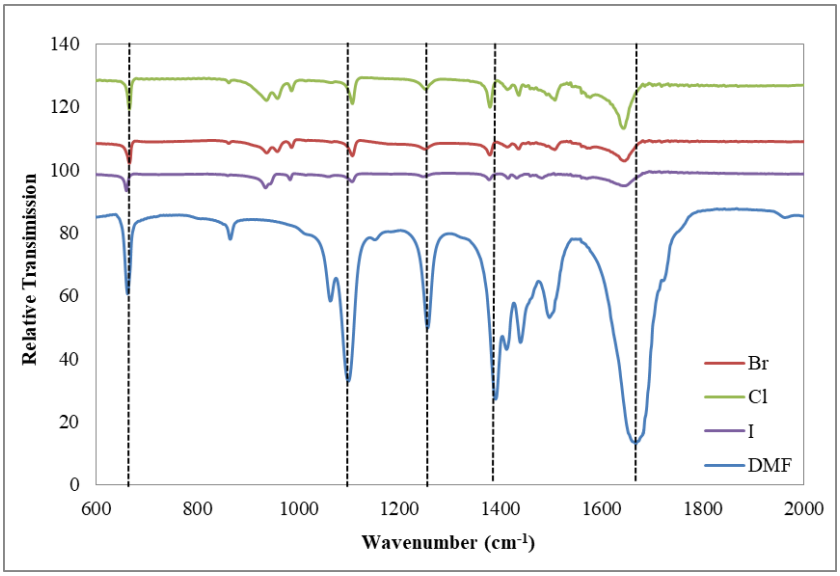

Figure 4.2.7-4. FTIR spectra of DMF solvent, $MAPbI_3 \cdot DMF$, $MAPbI_2Cl \cdot DMF$, and $MAPb_{1.5}I_3Br \cdot DMF$.

4.3 Conclusion

In this chapter, we monitored the film formation processes from chloride precursor by using optical microscope, TEM, powder and single crystal XRD, UV-Vis, FT-IR, elemental analysis and TGA. According to the results, we identified two intermediates and found the recrystallization process of one intermediate that happened before spin-coating or at the early stage of annealing was the key to produce the perovskite film with high crystallinity and orientation. In addition, we also suggested a set of chemical reactions to describe the whole formation process of the perovskite film. This work is for the first time that studying the formation mechanism of perovskite based on single crystals, which reasonably indicates the chemical reactions happened during the formation process on molecular level. We hope our research can provide helpful information and suggestions on the improvement of perovskite solar cells in terms of precursor formulations, additive selections, and fabrication techniques.

Furthermore, we successfully get the single crystals of intermediates from three precursors [PbI_2 + MAI], [$PbCl_2$ + 3MAI] and [$PbBr_2$ + MAI], which have formulas of $MAPbI_3 \cdot DMF$, $MAPbI_2Cl \cdot DMF$ and $MAPb_{1.5}I_3Br \cdot DMF$, respectively. The structures of both $MAPbI_2Cl \cdot DMF$ and $MAPb_{1.5}I_3Br \cdot DMF$ are identified for the first time. The crystal structures of them are similar, which contain 1-D lead-halogen chains and crystalline organic species. We found the structures of intermediates play important roles in the perovskite formation processes through influencing the evaporation temperatures of crystalline DMF molecules and MAX gases. Therefore, the halogen species in precursor have significant influence on the crystal structures of intermediates, and further determine the formation mechanisms of perovskite films.

5 Improving the performance of perovskite solar cells from lead acetate-based precursors

5.1 Introduction

So far, many lead salts, such as PbI_2, $PbCl_2$, and $Pb(OAc)_2$, etc. have been used as lead sources for preparing the precursors of perovskite solar cells, and each lead source has its unique impact on the perovskite films formation processes.[67, 72, 125, 147, 148] Now, $Pb(OAc)_2$ has become a burgeoning lead source, which has good solubility in a variety of solvents and can lead to a ultra-fast crystallization process.[90] As a result, the perovskite films formed from $Pb(OAc)_2$-based precursor were usually ultra-smooth and pinhole-free. Recently, Zhang *et al.* used $Pb(OAc)_2$ prepare precursors to fabricate smooth perovskite thin films through one-step coating method.[149] Zhu *et al.* used MABr as additive in the $Pb(OAc)_2$-based precursor solutions and enabled the controllable fabrication of ultra-smooth perovskite films and devices with PCE of exceeding 18 %.[67, 150] Snaith's group reported a new precursor combining $Pb(OAc)_2{\cdot}3H_2O$ and $PbCl_2$ together, which can produce perovskite films with large grains, high crystallinity, good smoothness and no pinholes.[67, 72, 91, 150] Zheng *et al.* also used $Pb(OAc)_2{\cdot}3H_2O$ as lead source and produced perovskite solar cells with the highest PCE of 12.3 %. They found when the content of hydration water in the perovskite precursor solutions gradually decreased to 0, the PCE of devices became to only 9.3 %.[147]

In this chapter, we mainly focused on improving the performance of PSCs from $Pb(OAc)_2$-based precursors by changing hydrate number, using pre-heated coating method, and applying DMSO as additive. In detail, we prepared two types of precursors by selecting $Pb(OAc)_2$ and $Pb(OAc)_2{\cdot}3H_2O$ as lead sources and DMF as solvent. Conventional one-step coating method and pre-heating coating method were used for the fabrication of perovskite thin films. In addition, DMSO was added in

precursors as additive to modifying the crystallization process of perovskite thin films. The perovskite thin films from different deposition methods were characterized by UV-Vis, XRD and SEM. The highest PCE of 15.714 % was achieved by the processing approach that used $Pb(OAc)_2$ $3H_2O$ as lead source, 5 % of DMSO as additive in precursor, and pre-heating coating as deposition method.

5.2 Results and discussion

5.2.1 Photovoltaic performances of PSCs

To study the influence of different methods on PSC performances, the PSCs with the inverted planar structure of ITO / PEDOT : PSS / PVSK / $PC_{61}BM$ / Al were adopted. The results of current density-voltage measurement of PSCs from different fabrication methods were shown in Table 5.2.1, the related PSC devices were labeled as A. hydrate precursor by conventional method; B. anhydrate precursor by pre-heating method; C. hydrate precursor by pre-heating method; D. hydrate precursor with 5% DMSO by pre-heating method.

Table 5.2.1 Photovoltaic performances of PSCs from different precursors. The average data of PCE is taken from 8 individual devices. The devices are labeled as (A. hydrate precursor by conventional method; B. anhydrate precursor by pre-heating method; C. hydrate precursor by pre-heating method; D. hydrate precursor with 5% DMSO by pre-heating method.)

Note	V_{OC} (V)	J_{SC} (mA/cm^2)	FF	PCE (%)	PCE_{MAX} (%)
A	0.975±0.007	17.767±0.425	0.687±0.011	10.636±0.324	11.901
B	0.646±0.047	18.673±0.644	0.522±0.012	5.187±0.775	6.297
C	1.013±0.043	22.446±0.723	0.675±0.020	14.071±0.621	15.348
D	1.021±0.012	22.210±0.346	0.693±0.007	14.816±0.347	15.714

Clearly, the devices that used hydrate precursors (A, C and D) had much better performance than that used anhydrate one (B) which had low V_{OC} of only 0.646 V and FF of 0.522. Compared with the conventional coating method (A), the pre-heating coating method (C and D) can obviously improve the device performances by boosting the nucleation and crystallization speeds of perovskite thin films, which obviously increased the J_{SC} values. However, we found that the pre-heating method was hard to repeat due to the uneven temperature distribution on substrates which was caused by handling difference. The uneven temperature distribution on substrates can strongly influence the nucleation process of perovskite thin films by changing the solvent evaporation and solute ultra-saturation speeds of precursor solutions. To

improve the reproducibility of device fabrication, we selected the strong coordination solvent DMSO as additive, which aimed to uniform the nucleation process of perovskite thin films. 5 % was found as the best ratio of adding DMSO in precursor (D), which further improved both the performance and the reproducibility of PSCs, which gave the best PSCs with a high PCE of 15.714 %.

5.2.2 Characterizations of perovskite thin films

As shown in Figure 5.2.2-1 and Table 5.2.2, the perovskite film of A had a smooth and pinhole-free surface, where the grains with sizes of 52.26 nm tightly packed. The perovskite film of B showed a morphology with very low coverage, where the perovskite crystals with sizes ranging from 98.85 nm unregularly arranged. Interestingly, C had a perovskite film with much higher coverage and bigger grain sizes of 114.07 nm, but some pinholes and cracks existed. Obviously, D had a better morphology than C, where the perovskite grains with sizes of 179.32 nm tightly packed with no pinholes or cracks. Thus, the perovskite film from conventional method had smooth and pinhole-free produced the devices with high V_{OC}, but the small crystal grains with uncountable crystal boundaries accelerated the carrier recombination and limited the J_{SC} value. One the other side, the full-coverage and big grain sizes of the perovskite film from D ensured the efficient light absorption and carrier transportation, which led to the higher J_{SC} and V_{OC} values of devices.[100]

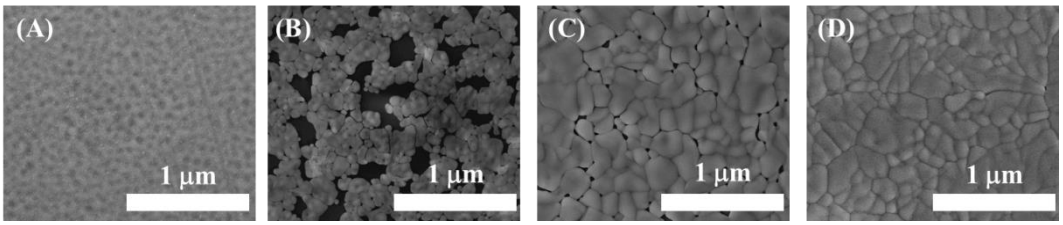

Figure 5.2.2-1. SEM images of perovskite thin films. The samples are labeled as (A. hydrate precursor by conventional method; B. anhydrate precursor by pre-heating method; C. hydrate precursor by pre-heating method; D. hydrate precursor with 5% DMSO by pre-heating method.)

Figure 5.2.2-2 showed the UV-Vis absorption spectra of perovskite films from

different methods. Obviously, from A to D, the absorption intensities at lower energy area (490 - 800 nm) clearly increased, which indicated the thickness and crytsallinity of the perovskite films increased.[94, 101, 102] In addition, the strong absorption of C and D at higher energy area (370 - 490 nm) ensured the efficient light harvesting of perovskite thin films, which also ensured the high J_{SC} of devices. Furthermore, the absorption curve of B at lower energy area (490 - 800 nm) turned flat and decreased, which was essentially caused by the low coverage of perovskite film.[94, 101, 102]

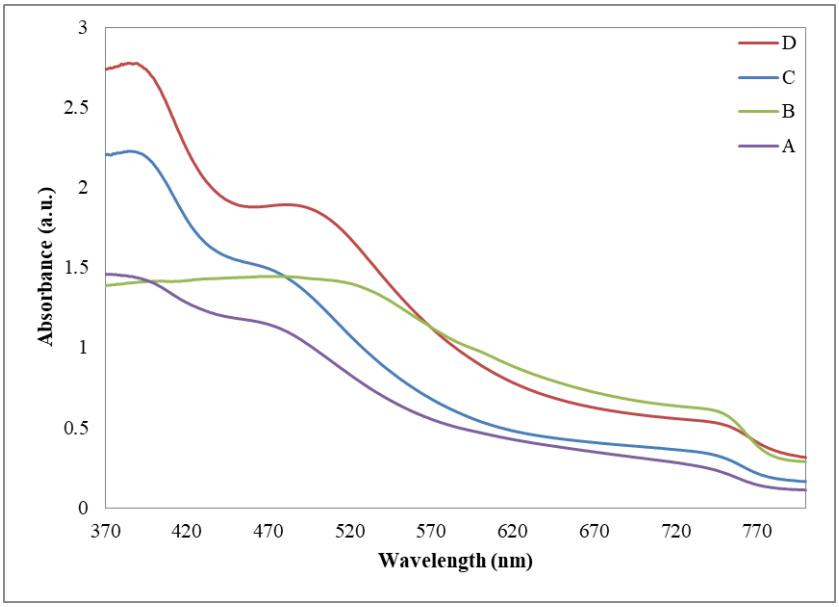

Figure 5.2.2-2. UV-Vis spectra of perovskite thin films. The samples are labeled as (A. hydrate precursor by conventional method; B. anhydrate precursor by pre-heating method; C. hydrate precursor by pre-heating method; D. hydrate precursor with 5% DMSO by pre-heating method.)

The XRD patterns of perovskite thin films from different methods were shown in Figure 5.2.2-3. The diffraction intensity of A was extremely weak. This phenomenon should be caused by the tiny crystal sizes of perovskite film, which made the sample more amorphous but not crystalline. During spin-coating or annealing of the anhydrate $Pb(OAc)_2$-based precursor, the MAOAc with low decomposition temperature (85 - 97 ^oC) fast escaped from the wet film, which made the formation process of perovskite thin film was ultra-fast and hard to control.[67] So the

conventional method cannot ensure the resulted perovskite film with both high coverage and big grain sizes in the same time.

The pre-heating coating method accelerated the solvent evaporation and advanced the annealing process, which ensured the nucleation and crystallization of perovskite film happen at the same time.[151] In other words, the perovskite crystals can grow around the pre-formed seeds to a much bigger size and further enhanced the cystallinity of perovskite films. Therefore, the pre-heating method avoided the low crystallinity caused by the excessive nucleation of perovskite seeds when ensured the high coverage of perovskite thin films. As a result, the diffraction intensities from A to B, C, D significantly increased, which indicated the cystallinities of perovskite films produced from the pre-heating coating method was much stronger than the conventional one.

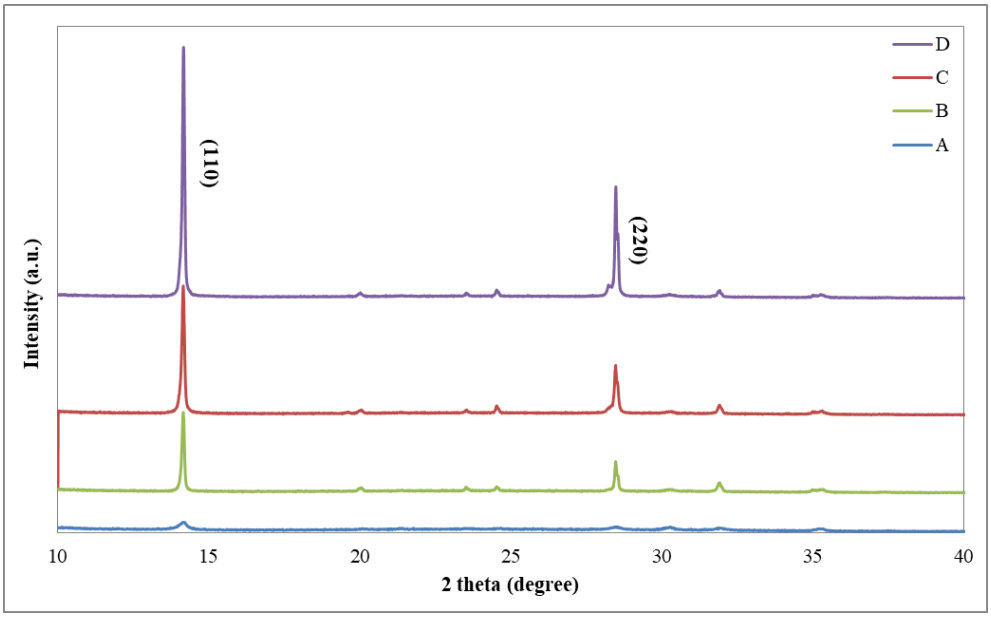

Figure 5.2.2-3. XRD patterns of perovskite thin films. The samples are labeled as (A. hydrate precursor by conventional method; B. anhydrate precursor by pre-heating method; C. hydrate precursor by pre-heating method; D. hydrate precursor with 5% DMSO by pre-heating method.)

Table 5.2.2. The calculated average grain sizes of perovskite films based on the Scherer equation ($D = K\lambda / B\cos\theta$, where K here is 0.943, λ = 1.54056Å, B = FWHW × π / 180°).

Sample	FWHW	Average grain sizes
A	0.2213 °	52.26 nm
B	0.1170 °	98.85 nm
C	0.1016 °	114.07 nm
D	0.0645°	179.32 nm

As reported, the crystalline H_2O in $Pb(OAc)_2 \cdot 3H_2O$ can form an intermediate phase $MAPbI_3 \cdot xH_2O$ ($0 \leq x \leq 1.5$) after the reaction between MAI and $Pb(OAc)_2 \cdot 3H_2O$.[150] Thus, the transformation from the intermediate phase $MAPbI_3 \cdot xH_2O$ to $MAPbI_3$ by releasing remained crystalline water can produce the high-quality perovskite film with better orientation and crystallinity, which caused the higher XRD intensity of C. In addition, we directly used the $Pb(OAc)_2 \cdot 3H_2O$ as material to increase the ratio of water in precursor. As an anti-solvent of perovskite, the H_2O molecules can also accelerated the formation process, especially the nucleation process of perovskite film, which further improved the film coverage.

Adding DMSO as additive in precursor solutions resulted in the formation of the other two intermediates, $PbI_2 \cdot DMSO$ and $Pb(OAc)_2 \cdot DMSO$, in the wet films during perovskite formation.[118, 138, 152] Because the coordination ability of DMSO is much stronger than H_2O,[118] the DMSO would replace some H_2O to form stable intermediates with Pb(II) ions. Due to the high viscosity of DMSO, over 10 % was added can significantly influence the spin-coating process of precursor solution, which always produced perovskite films with rough surface and low coverage. 5% was found as the most suitable amount of DMSO in precursor. Compared with the $MAPbI_3 \cdot xH_2O$, the much slower decomposition of $PbI_2 \cdot DMSO$ and the multi-step reactions between $Pb(OAc)_2 \cdot DMSO$ and MAI can retard the perovskite formation and further improve the crystallinity of perovskite thin films, which led to the best crystallinity of D.

5.3 Conclusion

We constructed several groups of PSCs from $Pb(OAc)_2$-based precursors by changing hydrate number, changing spin-coating method, and applying DMSO as additive. The perovskite thin films from different deposition methods were characterized by UV-Vis, XRD and SEM. The H_2O molecules in precursors were found to improve the film coverage and the crystallinity. The pre-heating method avoided the low crystallinity when ensured the high coverage of perovskite thin films. In addition, the adding of DMSO as additive influenced the formation kinetics of perovskite films and improved the reproducibility of devices. As a result, the highest PCE of 15.714 % was achieved by the processing approach that used $Pb(OAc)_2$ $3H_2O$ as lead source, 5 % of DMSO as additive in precursor, and pre-heating coating as deposition method.

6 Experimental

6.1 Materials

Methylamine alcohol solution (AR, 32 wt. %), hydroiodic acid (AR, 45 wt. % in H2O), diethyl ether (AR, 99.5 %) were purchased from Sinopharm Chemical Reagent Co., Ltd. Lead (II) chloride (PbCl2, 99.999 %), lead (II) bromide (99.999 %, metals basis), lead (II) iodide (99.999 %, metals basis), lead (II) acetate trihydrate ($Pb(OAc)_2 \cdot 3H_2O$, 99.999 %) GBL (GC, 99.9 %), DMF (HPLC, 99.8 %), and [6,6]-phenyl-C61-butyric acid methyl ester (PCBM) (99.9 %) were purchased from Aladdin Industrial Corporation. Ethanol (HPLC) and 2-propanol (HPLC) were purchased from Fisher Scientific. PEDOT : PSS solution (Clevios PVP Al 4083) was purchased from Heraeus Precious Metals GmbH & Co. KG. Patterned ITO/glass substrates were purchased from Jiajing Photoelectricity Co., Ltd.

6.2 Synthesis of methylamine iodide (MAI)

Methylamine iodide was synthesized according to the reported procedure.[92, 153] In a typical synthesis, 15 mL of methylamine solution (0.066 mol), 10 mL of hydroiodic acid (0.053 mol), and 100 mL of ethanol were mixed in a 250 mL round-bottomed flask under ice bath for 2 hours with stirring. The white solid was collected by removing solvent on a rotary evaporator at 55 ^{o}C carefully. Then the raw product was dissolved in 30 mL of hot ethanol and recrystallized by adding diethyl ether dropwise. The white crystal was filtered and washed with diethyl ether for three times. Finally the MAI powder was collected and dried in a vacuum oven at room temperature overnight.

6.3 Preparation of precursor solutions

The dual-solvent method

$PbCl_2$ and MAI were mixed with a molar ratio of 1:3 in GBL/DMF mixtures (GBL:DMF (v:v) = 10:0, 9:1, 8:2, 7.5:2.5, 7:3, 6.5:3.5, 6:4, 5:5, 6:4, 7:3, 8:2, 9:1 and 0:10) to give solutions with the concentration of $PbCl_2$ as 0.8M. The precursor solutions were kept at 60 ^oC under stirring overnight.

The mechanism study

Iodide precursor PbI_2/MAI(1:1): PbI_2 and MAI were mixed with a molar ratio of 1:1 in DMF to give solutions with the concentration of Pb (II) as 0.8 M. The precursor solutions were kept at 60 ^oC under stirring overnight. Chloride precursor $PbCl_2$/MAI(1:3): $PbCl_2$ and MAI were mixed with a molar ratio of 1:3 in DMF to give solutions with the concentration of Pb (II) as 0.8 M. The precursor solutions were kept at 60 ^oC under stirring overnight. Bromide precursor $PbBr_2$/MAI(1:3): $PbBr_2$ and MAI were mixed with a molar ratio of 1:3 in DMF to give solutions with the concentration of Pb (II) as 0.8 M. The precursor solutions were kept at 60 ^oC under stirring overnight.

The pre-heating assisted method

Anhydrous $Pb(OAc)_2$ was prepared by heating $Pb(OAc)_2 \cdot 3H_2O$ at 110 ^oC under vacuum overnight. $Pb(OAc)_2$ / $Pb(OAc)_2 \cdot 3H_2O$ and MAI were mixed with a molar ratio of 1:3 in DMF to prepare anhydrate / hydrate precursor solutions with concentration of 1.0 M, respectively. The precursor solutions were kept at room temperature for 2 hours.

6.4 Fabrication of devices

ITO glass substrates were cleaned with detergent, deionized water, acetone, and 2-propanol under ultrasonic each for 10 min sequentially. Then the ITO substrates were stored in 2-propanol. Before spin-coating, the substrates were firstly dried in an oven at 120 ^{o}C, and then cleaned by oxygen plasma cleaner under vacuum for 5 minutes. The PEDOT : PSS solution was spin-coated onto the freshly prepared clean ITO glass substrate at 3500 rpm for 60s and then annealed at 125 ^{o}C for 25 min. The spin-coating and annealing processes were operated in air. Then the ITO glass substrate with the PEDOT : PSS layer was transferred into a glovebox filled with dry N_2 to avoid the contacting with moisture and oxygen.

For the dual-solvent method, the perovskite film was then deposited onto the substrate by spin-coating the precursor solutions at 6000 rpm for 60 s, and annealed at 95 ^{o}C for 30-120 min (from [GBL] to [DMF]) inside the glovebox.

For the pre-heating assisted method, the perovskite films were spin-coated from the pre-heated precursor solutions with temperature of 95 ℃ at 4000 rpm for 50 s, and annealed on a hot plate at 90 ℃ for 10 min.

For the conventional one-step spin-coating method, the perovskite precursor solvent was spin-coated on substrates whose temperature were kept at room temperature at 4000 rpm for 60 s, and annealed on the hot plate at 90 ℃ for 20 min.

After the construction of perovskite layer was complete, 50 μL of PCBM solution (20 mg/mL in chlorobenzene) was spin-coated at 1000 rpm for 60 s onto it. Finally, a layer of aluminum electrode (100 nm thickness) was deposited onto the PCBM layer by thermal evaporation under a high vacuum evaporator at 10^{-5} Pa.

6.5 Single crystal growth of $MAPbI_3$·DMF, $MAPbI_2Cl$·DMF, and $MAPbI_2Br$·DMF

All the single crystals were gown through the same method. The three precursor solutions were diluted to 0.4 M and filtered, then for each precursor, 1 mL of the diluted solution was added into a clean 10 mL vials, which was layered carefully with ~7 mL of IPA, and was carefully stored away from light to allow slow diffusion. After 2-3 days, light-yellow needle-shaped crystals appeared.

6.6 Instruments

The main instruments used for PSCs fabrication: plasma cleaner (HARRICK PPC-002), oven (Senxin DGG-9030 AD), vacuum spin coater (MTI Corporation VTC-100), and glovebox with high vacuum evaporator (Vigor). The current density-voltage (*J-V*) measurements were carried out in a N_2-filled glovebox with a Keithley 2400 source meter under simulated AM 1.5G solar illumination (100mW/cm^2).

Single crystal X-ray diffraction: Single crystal structure analysis was performed on a Bruker D8 Venture X-ray diffractometer. Single crystals were mounted on a glass fiber with grease. Data collection was performed at 180 K with graphite-monochromated Mo K_α radiation (λ = 0.71073 Å), operating at 50 kV and 30 mA. No significant decay was observed during the data collections. Reflection data were processed on a PC using the Bruker AXS Crystal Structure Analysis Package: Data collection: APEX2 (Bruker, 2006); cell refinement: SAINT (Bruker, 2005); data reduction: SAINT (Bruker, 2005); structure solution: XPREP (Bruker, 2005) and SHELXTL (Bruker, 2000); structure refinement: SHELXTL; molecular graphics: SHELXTL; publication materials: SHELXTL. Neutral atom scattering factors were taken from Cromer and Waber. The structures were all solved by direct methods. Full-matrix least-square refinements minimizing the function $\sum_w (F_o^2 - F_c^2)^2$ were applied to the compounds.

X-ray absorption spectroscopy: All the X-ray absorption spectroscopy (XAS) measurements were conducted in Stanford Synchrotron Radiation Lightsource (SSRL). Pb L_3-edge XANES and EXAFS were acquired at beamline 7-3, which is equipped with a Si(220) $\emptyset$=90^o double crystal monochromator, a 9 keV cutoff mirror, and an He cryostat (at 12 K). Data were collected using a Canberra 30-element Ge solid state detector.[1] Pb foil was utilized as reference for Pb L_3-edge. The powder

samples were grinded and sandwiched between two Kepton tapes, and the solution samples were placed in 3D printed liquid cell with about 0.2 ml. During data collection the samples were maintained at 10 K using an Oxford instruments liquid helium flow cryostat. All EXAFS spectra were measured for 10-12 scans and averaged to improve the signal-to-noise ratio. Athena software with IFEFFIT package was carried out for data averaging, energy calibration, and normalization. Shell-model was applied to extract structural parameters by fitting experimental EXAFS spectra with Artemis program.

FT-IR: The intermediate crystals were washed with DMF/IPA mixture and grated in an agate mortar firstly. Then the wet mixture was speared on a NaCl carrier and dried before measurement. The wet films were prepared by spreading precursors onto glass substrates and drying on hotplate. The FT-IR spectra were measured by Agilent Technologies Cary 660 FTIR.

UV-Vis: The intermediate crystals was washed with DMF/IPA mixture and grated in an agate mortar firstly. The paste mixture was then speared on a slide for solid-state measurement. The wet films were prepared by spreading precursors onto glass substrates and drying on hotplate. The UV-Vis absorption spectra were analyzed by Agilent Technologies Cary 300 UV-Vis.

Optical microscope: The precursors were coated on slides and heated on hotplate in air. An OLYMPUS DP26 optical microscope was used to obtain the optical microscope images.

Thermogravimetric analysis: About 10 mg of the intermediate crystals were preliminarily dried on weighing paper then placed in an alumina crucible. A Netzsch thermogravimetric analyzer (STA 449 F3) was used to measure the mass loss of the intermediates. The whole analysis was protected by a constant nitrogen flow.

XRD: The intermediate crystals was washed with DMF/IPA mixture and grated in an agate mortar firstly. The paste mixture was then speared on a slide for measurement. The wet films were prepared by spreading precursors onto glass substrates and drying on hotplate. The powder X-ray diffraction patterns were obtained by a powder X-ray diffractometer (Bruker D8 Advance), using Cu tube with λ=1.54Å, instrument voltage of 40kV, and current of 40mA.

HR-TEM: The HR-TEM images were taken on a FEI TENCNAI G2 20 200KV high resolution transition electron microscopy. The d-spacing in HR-TEM images were calculated through the Digital micrograph program. All the samples were prepared by dropping precursor onto copper nets under annealing at 65 ^{o}C in an oven for different time.

Elemental analysis: The elemental analysis was collected on an elemental analyzer (Elementar Vario Macro).

NMR: The nuclear magnetic resonance (NMR) spectra were obtained by a NMR spectrometer (Bruker Ascend^{TM} 400).

7 Conclusion and outlook

In section 3, by using the solvent engineering strategy, we have successfully fabricated a series of inverted PSCs by using simple one-step method from the chloric precursors that were prepared from solvents of DMF:GBL = 0:10, 1:9, 2:8, 2.5:7.5, 3:7, 3.5:6.5, 4:6, 5:5, 6:4, 7:3, 8:2, 9:1 and 0:10 (v:v). The highest device PCE of 11.556 % was achieved by using the solvent DMF:GBL = 3.5:6.5 (v:v). Meanwhile, the formation mechanisms of perovskite films from different solvents were also proposed. Briefly, the pure DMF-based perovskite film with high crystallinity and large grains was originated from the limited nucleation and slow conversion of the intermediate phase $MA_{x+y}PbI_{2+x}Cl_y \cdot m$DMF. The pure GBL-based perovskite film with high coverage was produced by the fast nucleation of the perovskite crystals. The formation of the best performance films from DMF:GBL = 3.5:6.5 was a result of the fast nucleation of the perovskite crystals and the slow conversion of the intermediate phase to perovskites, which lead to good morphology and large grain sizes. Obviously, solvent engineering provided a simple approach to improve the qualities of perovskite films by combining the advantageous properties like high crystallinity, large grain sizes, and high coverage.

In section 4, single crystals of $MAPbI_3 \cdot$DMF, $MAPbI_2Cl \cdot$DMF and $MAPb_{1.5}I_3Br \cdot$DMF were successfully prepared, and their structures of both were identified for the first time using single crystal X-ray diffraction technique. The crystal structures of the three compounds were quite similar, which contained 1-D lead-halogen chains and crystalline organic species. We found the structures of intermediates play important roles in the perovskite formation processes through influencing the evaporation temperatures of crystalline DMF molecules and MAX gases. Therefore, the halogen species in precursor have significant influence on the crystal structures of intermediates, and further determine the formation mechanisms of perovskite films. Furthermore, by using optical microscope, TEM, powder and

single crystal XRD, UV-Vis, FT-IR, elemental analysis and TGA, we found the recrystallization process of $MAPbI_2Cl \cdot DMF$ that happened before spin-coating or at the early stage of annealing was the key to produce the perovskite film with high crystallinity and orientation. In addition, a set of chemical reactions to describe the whole formation process of the perovskite film were proposed. To the best of our knowledge, this work is very first one in the area that studying the formation mechanism of perovskite based on single crystals and at molecular level. The work provided helpful information and suggestions on the improvement of perovskite solar cells in terms of precursor formulations, additive selections, and fabrication techniques.

In section 5, several groups of PSCs from $Pb(OAc)_2$-based precursors were fabricated by varying the hydrate number, finely tuning the spin-coating method, and applying DMSO as additive. The perovskite thin films from different deposition methods were characterized by UV-Vis, XRD and SEM. The H_2O molecules in precursors were found to improve the film coverage. The pre-heating method avoided the low crystallinity when ensured the high coverage of perovskite thin films. In addition, the adding of DMSO as additive influenced the formation kinetics of perovskite films and improved the reproducibility of devices. As a result, the PCE as high as 15.714 % was achieved with $Pb(OAc)_2 \cdot 3H_2O$ as lead source, 5 % of DMSO as additive in precursor, and pre-heating coating as deposition method.

8 References

1. Jena, A. K.; Kulkarni, A.; Miyasaka, T., Halide Perovskite Photovoltaics: Background, Status, and Future Prospects. *Chem Rev* 2019, 119, 3036-3103.
2. Qiu, L.; He, S.; Ono, L. K.; Liu, S.; Qi, Y., Scalable Fabrication of Metal Halide Perovskite Solar Cells and Modules. *ACS Energy Lett.* 2019, 4, 2147-2167.
3. Galagan, Y., Perovskite Solar Cells: Toward Industrial-Scale Methods. *J Phys Chem Lett* 2018, 9, 4326-4335.
4. Kazim, S.; Nazeeruddin, M. K.; Gratzel, M.; Ahmad, S., Perovskite as light harvester: a game changer in photovoltaics. *Angewandte Chemie* 2014, 53, 2812-24.
5. Lotsch, B. V., New light on an old story: perovskites go solar. *Angewandte Chemie* 2014, 53, 635-7.
6. Hu, Y.; Song, L.; Chen, Y.; Huang, W., Two-Terminal Perovskites Tandem Solar Cells: Recent Advances and Perspectives. *Solar RRL* 2019, 3, 1900080.
7. Sum, T. C.; Mathews, N., Advancements in perovskite solar cells: photophysics behind the photovoltaics. *Energy Environ. Sci.* 2014, 7, 2518-2534.
8. Jung, H. S.; Park, N. G., Perovskite solar cells: from materials to devices. *Small* 2015, 11, 10-25.
9. Zhang, T.; Lin, W., Metal-organic frameworks for artificial photosynthesis and photocatalysis. *Chem Soc Rev* 2014, 43, 5982-93.
10. Tong, X.; Lin, F.; Wu, J.; Wang, Z. M., High Performance Perovskite Solar Cells. *Advanced science* 2016, 3, 1500201.
11. Sherkar, T. Device physics of hybrid perovskite solar cells. University of Groningen, Groningen, 2018.
12. Liu, T.; Chen, K.; Hu, Q.; Zhu, R.; Gong, Q., Inverted Perovskite Solar Cells: Progresses and Perspectives. *Advanced Energy Materials* 2016, 6, 1600457.
13. Park, N.-G., Crystal growth engineering for high efficiency perovskite solar cells. *CrystEngComm* 2016, 18, 5977-5985.
14. Park, N. G., Methodologies for high efficiency perovskite solar cells. *Nano convergence* 2016, 3, 15.
15. Kojima, A.; Teshima, K.; Shirai, Y.; Miyasaka, T., Organometal halide perovskites as visible-light sensitizers for photovoltaic cells. *Journal of the American Chemical Society* 2009, 131, 6050-1.
16. Sahli, F.; Werner, J.; Kamino, B. A.; Bräuninger, M.; Monnard, R.; Paviet-Salomon, B.; Barraud, L.; Ding, L.; Diaz Leon, J. J.; Sacchetto, D.; Cattaneo, G.; Despeisse, M.; Boccard, M.; Nicolay, S.; Jeangros, Q.; Niesen, B.; Ballif, C., Fully textured monolithic perovskite/silicon tandem solar cells with 25.2% power conversion efficiency. *Nature materials* 2018, 17, 820-826.
17. Song, T.-B.; Chen, Q.; Zhou, H.; Jiang, C.; Wang, H.-H.; Yang, Y.; Liu, Y.; You, J.; Yang, Y., Perovskite solar cells: film formation and properties. *J. Mater. Chem. A* 2015, 3, 9032-9050.
18. Liu, M.; Johnston, M. B.; Snaith, H. J., Efficient planar heterojunction perovskite solar cells by vapour deposition. *Nature* 2013, 501, 395-8.
19. Chen, Q.; Zhou, H.; Hong, Z.; Luo, S.; Duan, H. S.; Wang, H. H.; Liu, Y.; Li, G.; Yang, Y., Planar heterojunction perovskite solar cells via vapor-assisted solution process. *Journal of the American Chemical Society* 2014, 136, 622-5.

20. Tavakoli, M. M.; Gu, L.; Gao, Y.; Reckmeier, C.; He, J.; Rogach, A. L.; Yao, Y.; Fan, Z., Fabrication of efficient planar perovskite solar cells using a one-step chemical vapor deposition method. *Scientific reports* 2015, 5, 14083.
21. Stranks, S. D.; Eperon, G. E.; Grancini, G.; Menelaou, C.; Alcocer, M. J. P.; Leijtens, T.; Laura, M.; Herz, M.; Petrozza, A.; Snaith, H. J., Electron-hole diffusion lengths exceeding 1 micrometer in an organometal trihalide perovskite absorber. *Science* 2013, 342.
22. Xing, G.; Mathews, N.; Sun, S.; Lim, S. S.; Lam, Y. M.; Grätzel, M.; Mhaisalkar, S.; Sum, T. C., Long-Range Balanced Electron- and Hole-Transport Lengths in Organic-Inorganic CH3NH3PbI3. *Science* 2013, 342, 344-347.
23. Yin, W.-J.; Shi, T.; Yan, Y., Unique Properties of Halide Perovskites as Possible Origins of the Superior Solar Cell Performance. *Adv. Mater.* 2014, 26, 4653-4658.
24. Yin, W.-J.; Yang, J.-H.; Kang, J.; Yan, Y.; Wei, S.-H., Halide perovskite materials for solar cells: a theoretical review. *J. Mater. Chem. A* 2015, 3, 8926-8942.
25. Egger, D. A.; Bera, A.; Cahen, D.; Hodes, G.; Kirchartz, T.; Kronik, L.; Lovrincic, R.; Rappe, A. M.; Reichman, D. R.; Yaffe, O., What Remains Unexplained about the Properties of Halide Perovskites? *Adv. Mater.* 2018, 30, 1800691.
26. <08219420.pdf>.
27. Rong, Y.; Hu, Y.; Mei, A.; Tan, H.; Saidaminov, M. I.; Seok, S. I.; McGehee, M. D.; Sargent, E. H.; Han, H., Challenges for commercializing perovskite solar cells. *Science* 2018, 361, eaat8235.
28. Zhang, J.; Zhang, W.; Cheng, H.-M.; Silva, S. R. P., Critical review of recent progress of flexible perovskite solar cells. *Mater. Today* 2020.
29. Chondroudis, K.; Mitzi, D. B., Electroluminescence from an Organic−Inorganic Perovskite Incorporating a Quaterthiophene Dye within Lead Halide Perovskite Layers. *Chem. Mater.* 1999, 11, 3028-3030.
30. Cho, H.; Jeong, S.-H.; Park, M.-H.; Kim, Y.-H.; Wolf, C.; Lee, C.-L.; Heo, J. H.; Sadhanala, A.; Myoung, N.; Yoo, S.; Im, S. H.; Friend, R. H.; Lee, T.-W., Overcoming the electroluminescence efficiency limitations of perovskite light-emitting diodes. *Science* 2015, 350, 1222-1225.
31. Lin, K.; Xing, J.; Quan, L. N.; de Arquer, F. P. G.; Gong, X.; Lu, J.; Xie, L.; Zhao, W.; Zhang, D.; Yan, C.; Li, W.; Liu, X.; Lu, Y.; Kirman, J.; Sargent, E. H.; Xiong, Q.; Wei, Z., Perovskite light-emitting diodes with external quantum efficiency exceeding 20 per cent. *Nature* 2018, 562, 245-248.
32. Na, G.; Zhang, L., Stable and luminescent halide perovskite fabricated in water. *Light: Science & Applications* 2020, 9, 106.
33. Wang, H.; Kosasih, F. U.; Yu, H.; Zheng, G.; Zhang, J.; Pozina, G.; Liu, Y.; Bao, C.; Hu, Z.; Liu, X.; Kobera, L.; Abbrent, S.; Brus, J.; Jin, Y.; Fahlman, M.; Friend, R. H.; Ducati, C.; Liu, X.-K.; Gao, F., Perovskite-molecule composite thin films for efficient and stable light-emitting diodes. *Nat. Comm.* 2020, 11, 891.
34. Dou, L.; Yang, Y.; You, J.; Hong, Z.; Chang, W.-H.; Li, G.; Yang, Y., Solution-processed hybrid perovskite photodetectors with high detectivity. *Nat. Comm.* 2014, 5, 5404.
35. Yakunin, S.; Sytnyk, M.; Kriegner, D.; Shrestha, S.; Richter, M.; Matt, G. J.; Azimi, H.; Brabec, C. J.; Stangl, J.; Kovalenko, M. V.; Heiss, W., Detection of X-ray photons by solution-processed lead halide perovskites. *Nat. Photonics* 2015, 9, 444-449.
36. Wang, H.; Kim, D. H., Perovskite-based photodetectors: materials and devices. *Chem. Soc. Rev.* 2017, 46, 5204-5236.
37. Gao, L.; Yan, Q., Recent Advances in Lead Halide Perovskites for Radiation Detectors. *Solar RRL*

2020, 4, 1900210.
38. Liu, P.; He, X.; Ren, J.; Liao, Q.; Yao, J.; Fu, H., Organic–Inorganic Hybrid Perovskite Nanowire Laser Arrays. *ACS Nano* 2017, 11, 5766-5773.
39. Dong, H.; Zhang, C.; Liu, X.; Yao, J.; Zhao, Y. S., Materials chemistry and engineering in metal halide perovskite lasers. *Chem. Soc. Rev.* 2020, 49, 951-982.
40. Kagan, C. R.; Mitzi, D. B.; Dimitrakopoulos, C. D., Organic-Inorganic Hybrid Materials as Semiconducting Channels in Thin-Film Field-Effect Transistors. *Science* 1999, 286, 945.
41. Lin, Y.-H.; Pattanasattayavong, P.; Anthopoulos, T. D., Metal-Halide Perovskite Transistors for Printed Electronics: Challenges and Opportunities. *Adv. Mater.* 2017, 29, 1702838.
42. Yi, J.; Miao, L.; Li, J.; Hu, W.; Zhao, C.; Wen, S., Third-order nonlinear optical response of CH3NH3PbI3 perovskite in the mid-infrared regime. *Opt. Mater. Express* 2017, 7, 3894-3901.
43. Ferrando, A.; Martínez Pastor, J. P.; Suárez, I., Toward Metal Halide Perovskite Nonlinear Photonics. *J. Phys. Chem. Lett.* 2018, 9, 5612-5623.
44. Boyd, C. C.; Cheacharoen, R.; Leijtens, T.; McGehee, M. D., Understanding Degradation Mechanisms and Improving Stability of Perovskite Photovoltaics. *Chem Rev* 2019, 119, 3418-3451.
45. Pellet, N.; Gao, P.; Gregori, G.; Yang, T. Y.; Nazeeruddin, M. K.; Maier, J.; Gratzel, M., Mixed-organic-cation perovskite photovoltaics for enhanced solar-light harvesting. *Angew. Chem. Int. Ed.* 2014, 53, 3151-7.
46. Lotsch, B. V., New Light on an Old Story: Perovskites Go Solar. *Angew. Chem. Int. Ed.* 2014, 53, 635-637.
47. Cao, X.; Zhi, L.; Jia, Y.; Li, Y.; Zhao, K.; Cui, X.; Ci, L.; Zhuang, D.; Wei, J., A Review of the Role of Solvents in Formation of High-Quality Solution-Processed Perovskite Films. *ACS Appl. Mater. Interfaces* 2019, 11, 7639-7654.
48. Jeon, N. J.; Na, H.; Jung, E. H.; Yang, T.-Y.; Lee, Y. G.; Kim, G.; Shin, H.-W.; Il Seok, S.; Lee, J.; Seo, J., A fluorene-terminated hole-transporting material for highly efficient and stable perovskite solar cells. *Nat. Energy* 2018, 3, 682-689.
49. Park, N.-G., Research Direction toward Scalable, Stable, and High Efficiency Perovskite Solar Cells. *Adv. Energy Mater.* 2020, 10, 1903106.
50. Ma, C.; Park, N.-G., A Realistic Methodology for 30% Efficient Perovskite Solar Cells. *Chem* 2020.
51. Kim, H.-S.; Hagfeldt, A.; Park, N.-G., Morphological and compositional progress in halide perovskite solar cells. *Chem. Commun.* 2019, 55, 1192-1200.
52. Pellet, N.; Gao, P.; Gregori, G.; Yang, T. Y.; Nazeeruddin, M. K.; Maier, J.; Gratzel, M., Mixed-organic-cation perovskite photovoltaics for enhanced solar-light harvesting. *Angewandte Chemie* 2014, 53, 3151-7.
53. Hao, F.; Stoumpos, C. C.; Liu, Z.; Chang, R. P.; Kanatzidis, M. G., Controllable perovskite crystallization at a gas-solid interface for hole conductor-free solar cells with steady power conversion efficiency over 10%. *Journal of the American Chemical Society* 2014, 136, 16411-9.
54. Umebayashi, T.; Asai, K.; Kondo, T.; Nakao, A., Electronic structures of lead iodide based low-dimensional crystals. *Physical Review B* 2003, 67, 155405.
55. De Wolf, S.; Holovsky, J.; Moon, S.-J.; Löper, P.; Niesen, B.; Ledinsky, M.; Haug, F.-J.; Yum, J.-H.; Ballif, C., Organometallic Halide Perovskites: Sharp Optical Absorption Edge and Its Relation to Photovoltaic Performance. *The journal of physical chemistry letters* 2014, 5, 1035-1039.
56. Kojima, A.; Ikegami, M.; Teshima, K.; Miyasaka, T., Highly Luminescent Lead Bromide Perovskite Nanoparticles Synthesized with Porous Alumina Media. *Chemistry Letters* 2012, 41, 397-399.

57. Wehrenfennig, C.; Eperon, G. E.; Johnston, M. B.; Snaith, H. J.; Herz, L. M., High charge carrier mobilities and lifetimes in organolead trihalide perovskites. *Advanced materials* 2014, 26, 1584-9.
58. Colella, S.; Mosconi, E.; Fedeli, P.; Listorti, A.; Gazza, F.; Orlandi, F.; Ferro, P.; Besagni, T.; Rizzo, A.; Calestani, G.; Gigli, G.; De Angelis, F.; Mosca, R., MAPbI3-xClxMixed Halide Perovskite for Hybrid Solar Cells: The Role of Chloride as Dopant on the Transport and Structural Properties. *Chemistry of Materials* 2013, 25, 4613-4618.
59. Heo, J. H.; Im, S. H.; Noh, J. H.; Mandal, T. N.; Lim, C.-S.; Chang, J. A.; Lee, Y. H.; Kim, H.-j.; Sarkar, A.; Nazeeruddin, M. K.; Grätzel, M.; Seok, S. I., Efficient inorganic–organic hybrid heterojunction solar cells containing perovskite compound and polymeric hole conductors. *Nature Photonics* 2013, 7, 486-491.
60. Lee, M. M.; Teuscher, J.; Miyasaka, T.; Murakami, T. N.; Snaith, H. J., Efficient Hybrid Solar Cells Based on Meso-Superstructured Organometal Halide Perovskites. *Science* 2012, 338, 643-647.
61. Meng, L.; You, J.; Guo, T. F.; Yang, Y., Recent Advances in the Inverted Planar Structure of Perovskite Solar Cells. *Acc Chem Res* 2016, 49, 155-65.
62. Xiao, M.; Huang, F.; Huang, W.; Dkhissi, Y.; Zhu, Y.; Etheridge, J.; Gray-Weale, A.; Bach, U.; Cheng, Y. B.; Spiccia, L., A fast deposition-crystallization procedure for highly efficient lead iodide perovskite thin-film solar cells. *Angewandte Chemie* 2014, 53, 9898-903.
63. Liang, P. W.; Liao, C. Y.; Chueh, C. C.; Zuo, F.; Williams, S. T.; Xin, X. K.; Lin, J.; Jen, A. K., Additive enhanced crystallization of solution-processed perovskite for highly efficient planar-heterojunction solar cells. *Advanced materials* 2014, 26, 3748-54.
64. Zuo, C.; Ding, L., An 80.11% FF record achieved for perovskite solar cells by using the NH4Cl additive. *Nanoscale* 2014, 6, 9935-8.
65. Zhu, T.; Yang, Y.; Gong, X., Recent Advancements and Challenges for Low-Toxicity Perovskite Materials. *ACS applied materials & interfaces* 2020.
66. Yang, W. S.; Noh, J. H.; Jeon, N. J.; Kim, Y. C.; Ryu, S.; Seo, J.; Seok, S. I., High-performance photovoltaic perovskite layers fabricated through intramolecular exchange. *Science* 2015, 348, 1234-1237.
67. Xiao, Y.; Yang, L.; Han, G.; Li, Y.; Li, M.; Li, H., Effects of methylammonium acetate on the perovskite film quality for the perovskite solar cell. *Org. Electron.* 2019, 65, 201-206.
68. Wojciechowski, K.; Saliba, M.; Leijtens, T.; Abate, A.; Snaith, H. J., Sub-150 °C processed meso-superstructured perovskite solar cells with enhanced efficiency. *Energy Environ. Sci.* 2014, 7, 1142-1147.
69. Jeng, J. Y.; Chiang, Y. F.; Lee, M. H.; Peng, S. R.; Guo, T. F.; Chen, P.; Wen, T. C., CH3NH3PbI3 perovskite/fullerene planar-heterojunction hybrid solar cells. *Advanced materials* 2013, 25, 3727-32.
70. Docampo, P.; Ball, J. M.; Darwich, M.; Eperon, G. E.; Snaith, H. J., Efficient organometal trihalide perovskite planar-heterojunction solar cells on flexible polymer substrates. *Nat Commun* 2013, 4, 2761.
71. Shao, Y.; Yuan, Y.; Huang, J., Correlation of energy disorder and open-circuit voltage in hybrid perovskite solar cells. *Nat. Energy* 2016, 1, 15001.
72. Chen, Y.; Li, L.; Yerramilli, A. S.; Qu, W.; Song, Y.; Li, N.; Shen, Y.; Alford, T. L., Introduction of nitrogen gas flow and precursor aging process to improve the efficiency of the lead acetate derived CH3NH3PbI3 perovskite solar cells. *Sol. Energy Mater. Sol. Cells* 2019, 190, 49-56.
73. Xia, F.; Xu, Y.; Li, B.; Hui, W.; Zhang, S.; Zhu, L.; Xia, Y.; Chen, Y.; Huang, W., Improved Performance of CH3NH3PbI3-xClx Resistive Switching Memory by Assembling 2D/3D Perovskite Heterostructures.

ACS Appl. Mater. Interfaces 2020, 12, 15439-15445.

74. Salim, T.; Sun, S.; Abe, Y.; Krishna, A.; Grimsdale, A. C.; Lam, Y. M., Perovskite-based solar cells: impact of morphology and device architecture on device performance. *J. Mater. Chem. A* 2015, 3, 8943-8969.

75. Mateen, M.; Arain, Z.; Yang, Y.; Liu, X.; Ma, S.; Liu, C.; Ding, Y.; Ding, X.; Cai, M.; Dai, S., MACl-Induced Intermediate Engineering for High-Performance Mixed-Cation Perovskite Solar Cells. *ACS Appl. Mater. Interfaces* 2020, 12, 10535-10543.

76. Cai, B.; Zhang, W.-H.; Qiu, J., Solvent engineering of spin-coating solutions for planar-structured high-efficiency perovskite solar cells. *Chinese Journal of Catalysis* 2015, 36, 1183-1190.

77. Chueh, C.-C.; Liao, C.-Y.; Zuo, F.; Williams, S. T.; Liang, P.-W.; Jen, A. K. Y., The roles of alkyl halide additives in enhancing perovskite solar cell performance. *J. Mater. Chem. A* 2015, 3, 9058-9062.

78. Xue, Q.; Hu, Z.; Sun, C.; Chen, Z.; Huang, F.; Yip, H.-L.; Cao, Y., Metallohalide perovskite–polymer composite film for hybrid planar heterojunction solar cells. *RSC Advances* 2015, 5, 775-783.

79. Jeon, N. J.; Noh, J. H.; Kim, Y. C.; Yang, W. S.; Ryu, S.; Seok, S. I., Solvent engineering for high-performance inorganic-organic hybrid perovskite solar cells. *Nature materials* 2014, 13, 897-903.

80. Kim, M.; Kim, G.-H.; Lee, T. K.; Choi, I. W.; Choi, H. W.; Jo, Y.; Yoon, Y. J.; Kim, J. W.; Lee, J.; Huh, D.; Lee, H.; Kwak, S. K.; Kim, J. Y.; Kim, D. S., Methylammonium Chloride Induces Intermediate Phase Stabilization for Efficient Perovskite Solar Cells. *Joule* 2019, 3, 2179-2192.

81. Chen, H.; Xia, Y.; Wu, B.; Liu, F.; Niu, T.; Chao, L.; Xing, G.; Sum, T.; Chen, Y.; Huang, W., Critical role of chloride in organic ammonium spacer on the performance of Low-dimensional Ruddlesden-Popper perovskite solar cells. *Nano Energy* 2019, 56, 373-381.

82. Stone, K. H.; Gold-Parker, A.; Pool, V. L.; Unger, E. L.; Bowring, A. R.; McGehee, M. D.; Toney, M. F.; Tassone, C. J., Transformation from crystalline precursor to perovskite in PbCl2-derived MAPbI3. *Nature communications* 2018, 9, 3458.

83. Liao, H.-C.; Guo, P.; Hsu, C.-P.; Lin, M.; Wang, B.; Zeng, L.; Huang, W.; Soe, C. M. M.; Su, W.-F.; Bedzyk, M. J.; Wasielewski, M. R.; Facchetti, A.; Chang, R. P. H.; Kanatzidis, M. G.; Marks, T. J., Enhanced Efficiency of Hot-Cast Large-Area Planar Perovskite Solar Cells/Modules Having Controlled Chloride Incorporation. *Adv. Energy Mater.* 2017, 7, 1601660.

84. Pham, N. D.; Tiong, V. T.; Chen, P.; Wang, L.; Wilson, G. J.; Bell, J.; Wang, H., Enhanced perovskite electronic properties via a modified lead(ii) chloride Lewis acid–base adduct and their effect in high-efficiency perovskite solar cells. *J. Mater. Chem. A* 2017, 5, 5195-5203.

85. Sakai, N.; Wang, Z.; Burlakov, V. M.; Lim, J.; McMeekin, D.; Pathak, S.; Snaith, H. J., Controlling Nucleation and Growth of Metal Halide Perovskite Thin Films for High-Efficiency Perovskite Solar Cells. *Small* 2017, 13.

86. Qing, J.; Chandran, H.-T.; Xue, H.-T.; Guan, Z.-Q.; Liu, T.-L.; Tsang, S.-W.; Lo, M.-F.; Lee, C.-S., Simple fabrication of perovskite solar cells using lead acetate as lead source at low temperature. *Organic Electronics* 2015, 27, 12-17.

87. Seo, J.; Park, S.; Chan Kim, Y.; Jeon, N. J.; Noh, J. H.; Yoon, S. C.; Seok, S. I., Benefits of very thin PCBM and LiF layers for solution-processed p–i–n perovskite solar cells. *Energy Environ. Sci.* 2014, 7, 2642-2646.

88. Jung, J. W.; Williams, S. T.; Jen, A. K. Y., Low-temperature processed high-performance flexible perovskite solar cells via rationally optimized solvent washing treatments. *RSC Adv.* 2014, 4, 62971-62977.

89. Jang, S.-R.; Zhu, K.; Ko, M. J.; Kim, K.; Kim, C.; Park, N. G.; Frank, A. J., Voltage-Enhancement

Mechanisms of an Organic Dye in High Open-Circuit Voltage Solid-State Dye-Sensitized Solar Cells. *ACS NANO* 2011, 5, 8267-8274.

90. Qiu, W.; Merckx, T.; Jaysankar, M.; Masse de la Huerta, C.; Rakocevic, L.; Zhang, W.; Paetzold, U. W.; Gehlhaar, R.; Froyen, L.; Poortmans, J.; Cheyns, D.; Snaith, H. J.; Heremans, P., Pinhole-free perovskite films for efficient solar modules. *Energy Environ. Sci.* 2016, 9, 484-489.

91. Kim, H. B.; Choi, H.; Jeong, J.; Kim, S.; Walker, B.; Song, S.; Kim, J. Y., Mixed solvents for the optimization of morphology in solution-processed, inverted-type perovskite/fullerene hybrid solar cells. *Nanoscale* 2014, 6, 6679-83.

92. Zhou, H.; Nie, Z.; Yin, J.; Sun, Y.; Zhuo, H.; Wang, D.; Li, D.; Dou, J.; Zhang, X.; Ma, T., Antisolvent diffusion-induced growth, equilibrium behaviours in aqueous solution and optical properties of CH3NH3PbI3 single crystals for photovoltaic applications. *RSC Adv.* 2015, 5, 85344-85349.

93. Xie, F. X.; Su, H.; Mao, J.; Wong, K. S.; Choy, W. C. H., Evolution of Diffusion Length and Trap State Induced by Chloride in Perovskite Solar Cell. *The Journal of Physical Chemistry C* 2016, 120, 21248-21253.

94. Yu, H.; Wang, F.; Xie, F.; Li, W.; Chen, J.; Zhao, N., The Role of Chlorine in the Formation Process of "CH3NH3PbI3-xClx" Perovskite. *Advanced Functional Materials* 2014, 24, 7102-7108.

95. Li, X.-Y.; Zhang, L.-P.; Tang, F.; Bao, Z.-M.; Lin, J.; Li, Y.-Q.; Chen, L.; Ma, C.-Q., The solvent treatment effect of the PEDOT:PSS anode interlayer in inverted planar perovskite solar cells. *RSC Adv.* 2016, 6, 24501-24507.

96. Yu, H.; Liu, X.; Xia, Y.; Dong, Q.; Zhang, K.; Wang, Z.; Zhou, Y.; Song, B.; Li, Y., Room-temperature mixed-solvent-vapor annealing for high performance perovskite solar cells. *J. Mater. Chem. A* 2016, 4, 321-326.

97. Liang, P.-W.; Chueh, C.-C.; Xin, X.-K.; Zuo, F.; Williams, S. T.; Liao, C.-Y.; Jen, A. K. Y., High-Performance Planar-Heterojunction Solar Cells Based on Ternary Halide Large-Band-Gap Perovskites. *Advanced Energy Materials* 2015, 5, 1400960.

98. Williams, S. T.; Zuo, F.; Chueh, C. C.; Liao, C. Y.; Liang, P. W.; Jen, A. K. Y., Role of Chloride in the Morphological Evolution of Organo-Lead Halide Perovskite Thin Films. *ACS NANO* 2014, 8, 10640-10654.

99. Chia, H. C.; Sheu, H. S.; Hsiao, Y. Y.; Li, S. S.; Lan, Y. K.; Lin, C. Y.; Chang, J. W.; Kuo, Y. C.; Chen, C. H.; Weng, S. C.; Su, C. J.; Su, A. C.; Chen, C. W.; Jeng, U. S., Critical Intermediate Structure That Directs the Crystalline Texture and Surface Morphology of Organo-Lead Trihalide Perovskite. *ACS applied materials & interfaces* 2017, 9, 36897-36906.

100. Gong, X.; Li, M.; Shi, X.-B.; Ma, H.; Wang, Z.-K.; Liao, L.-S., Controllable Perovskite Crystallization by Water Additive for High-Performance Solar Cells. *Advanced Functional Materials* 2015, 25, 6671-6678.

101. Wang, D.; Zhu, H. M.; Zhou, Z. M.; Wang, Z. W.; Lv, S. L.; Feng, S. P.; Cui, G. L., Effect of solvent on the perovskite thin film morphology and crystallinity. *Acta Phys. Sin.* 2015, 64, 038403.

102. Conings, B.; Baeten, L.; De Dobbelaere, C.; D'Haen, J.; Manca, J.; Boyen, H. G., Perovskite-based hybrid solar cells exceeding 10% efficiency with high reproducibility using a thin film sandwich approach. *Advanced materials* 2014, 26, 2041-6.

103. Zhang, T.; Guo, N.; Li, G.; Qian, X.; Li, L.; Zhao, Y., A general non-CH3NH3X (X = I, Br) one-step deposition of CH3NH3PbX3perovskite for high performance solar cells. *J. Mater. Chem. A* 2016, 4, 3245-3248.

104. Hamill, J. C. J.; Schwartz, J.; Loo, Y.-L., Influence of Solvent Coordination on Hybrid

Organic-Inorganic Perovskite Formation. *ACS Energy Lett.* 2018, 3, 92-97.
105. Munir, R.; Sheikh, A. D.; Abdelsamie, M.; Hu, H.; Yu, L.; Zhao, K.; Kim, T.; Tall, O. E.; Li, R.; Smilgies, D. M.; Amassian, A., Hybrid Perovskite Thin-Film Photovoltaics: In Situ Diagnostics and Importance of the Precursor Solvate Phases. *Advanced materials* 2017, 29, 1604113.
106. Foley, B. J.; Girard, J.; Sorenson, B. A.; Chen, A. Z.; Scott Niezgoda, J.; Alpert, M. R.; Harper, A. F.; Smilgies, D.-M.; Clancy, P.; Saidi, W. A.; Choi, J. J., Controlling nucleation, growth, and orientation of metal halide perovskite thin films with rationally selected additives. *J. Mater. Chem. A* 2017, 5, 113-123.
107. Mu, C.; Pan, J.; Feng, S.; Li, Q.; Xu, D., Quantitative Doping of Chlorine in Formamidinium Lead Trihalide (FAPbI3−xClx) for Planar Heterojunction Perovskite Solar Cells. *Advanced Energy Materials* 2017, 7, 1601297.
108. Zuo, C.; Ding, L., Modified PEDOT Layer Makes a 1.52 VVocfor Perovskite/PCBM Solar Cells. *Advanced Energy Materials* 2017, 7, 1601193.
109. Wu, Y.; Xie, F.; Chen, H.; Yang, X.; Su, H.; Cai, M.; Zhou, Z.; Noda, T.; Han, L., Thermally Stable MAPbI3 Perovskite Solar Cells with Efficiency of 19.19% and Area over 1 cm2 achieved by Additive Engineering. *Advanced materials* 2017, 29.
110. Tiep, N. H.; Ku, Z.; Fan, H. J., Recent Advances in Improving the Stability of Perovskite Solar Cells. *Advanced Energy Materials* 2016, 6, 1501420.
111. Xue, Q.; Sun, C.; Hu, Z.; Huang, F.; Yip, H.-L.; Cao, Y., Recent Advances in Perovskite Solar Cells: Morphology Control and Interfacial Engineering. *Acta Chimica Sinica* 2015, 73, 179.
112. Luo, S.; Daoud, W. A., Recent progress in organic–inorganic halide perovskite solar cells: mechanisms and material design. *J. Mater. Chem. A* 2015, 3, 8992-9010.
113. Zhang, Z. L.; Men, B. Q.; Liu, Y. F.; Gao, H. P.; Mao, Y. L., Effects of precursor solution composition on the performance and I-V hysteresis of perovskite solar cells based on CH3NH3PbI3-xClx. *Nanoscale research letters* 2017, 12, 84.
114. van Franeker, J. J.; Hendriks, K. H.; Bruijnaers, B. J.; Verhoeven, M. W. G. M.; Wienk, M. M.; Janssen, R. A. J., Monitoring Thermal Annealing of Perovskite Solar Cells with In Situ Photoluminescence. *Advanced Energy Materials* 2017, 7, 1601822.
115. Barrows, A. T.; Lilliu, S.; Pearson, A. J.; Babonneau, D.; Dunbar, A. D. F.; Lidzey, D. G., Monitoring the Formation of a CH3NH3PbI3-xClxPerovskite during Thermal Annealing Using X-Ray Scattering. *Advanced Functional Materials* 2016, 26, 4934-4942.
116. Chang, C. Y.; Huang, Y. C.; Tsao, C. S.; Su, W. F., Formation Mechanism and Control of Perovskite Films from Solution to Crystalline Phase Studied by in Situ Synchrotron Scattering. *ACS applied materials & interfaces* 2016, 8, 26712-26721.
117. Fei, C.; Guo, L.; Li, B.; Zhang, R.; Fu, H.; Tian, J.; Cao, G., Controlled growth of textured perovskite films towards high performance solar cells. *Nano Energy* 2016, 27, 17-26.
118. Li, L.; Chen, Y.; Liu, Z.; Chen, Q.; Wang, X.; Zhou, H., The Additive Coordination Effect on Hybrids Perovskite Crystallization and High-Performance Solar Cell. *Advanced materials* 2016, 28, 9862-9868.
119. McLeod, J. A.; Wu, Z.; Sun, B.; Liu, L., The influence of the I/Cl ratio on the performance of CH3NH3PbI(3-x)Cl(x)-based solar cells: why is CH3NH3I : PbCl2 = 3 : 1 the "magic" ratio? *Nanoscale* 2016, 8, 6361-8.
120. Manser, J. S.; Saidaminov, M. I.; Christians, J. A.; Bakr, O. M.; Kamat, P. V., Making and Breaking of Lead Halide Perovskites. *Accounts of chemical research* 2016, 49, 330-8.
121. Chen, A. Z.; Foley, B. J.; Ma, J. H.; Alpert, M. R.; Niezgoda, J. S.; Choi, J. J., Crystallographic

orientation propagation in metal halide perovskite thin films. *J. Mater. Chem. A* 2017, 5, 7796-7800.
122. Jiang, F.; Rong, Y.; Liu, H.; Liu, T.; Mao, L.; Meng, W.; Qin, F.; Jiang, Y.; Luo, B.; Xiong, S.; Tong, J.; Liu, Y.; Li, Z.; Han, H.; Zhou, Y., Synergistic Effect of PbI2Passivation and Chlorine Inclusion Yielding High Open-Circuit Voltage Exceeding 1.15 V in Both Mesoscopic and Inverted Planar CH3NH3PbI3(Cl)-Based Perovskite Solar Cells. *Advanced Functional Materials* 2016, 26, 8119-8127.
123. Zhou, Q.; Jin, Z.; Li, H.; Wang, J., Enhancing performance and uniformity of CH3NH3PbI(3-x)Cl(x) perovskite solar cells by air-heated-oven assisted annealing under various humidities. *Scientific reports* 2016, 6, 21257.
124. Tan, K. W.; Moore, D. T.; Saliba, M.; Sai, H.; Estroff, L. A.; Hanrath, T.; Snaith, H. J.; Wiesner, U., Thermally Induced Structural Evolution and Performance of Mesoporous Block Copolymer- Directed Alumina Perovskite Solar Cells. *ACS NANO* 2014, 8, 4730.
125. Moore, D. T.; Sai, H.; Tan, K. W.; Smilgies, D. M.; Zhang, W.; Snaith, H. J.; Wiesner, U.; Estroff, L. A., Crystallization kinetics of organic-inorganic trihalide perovskites and the role of the lead anion in crystal growth. *Journal of the American Chemical Society* 2015, 137, 2350-8.
126. Nenon, D. P.; Christians, J. A.; Wheeler, L. M.; Blackburn, J. L.; Sanehira, E. M.; Dou, B.; Olsen, M. L.; Zhu, K.; Berry, J. J.; Luther, J. M., Structural and chemical evolution of methylammonium lead halide perovskites during thermal processing from solution. *Energy & Environmental Science* 2016, 9, 2072-2082.
127. Vincent, B. R.; Robertson, K. N.; Cameron, T. S.; Knop, O., <v87-176.pdf>. *Can. J. Chem.* 1987, 65, 1042.
128. Geselle, M.; Fuess, H., Crystal structure of bis(tetrapropylammonium) tetraiodoplumbate(II) $((C_3H_7)_4N)_2PbI_4$. *Zeitschrift fr Kristallographie - New Crystal Structures* 1997, 212, 239.
129. Krautscheid, H.; Vielsack, F.; Klaassen, N., <Krautscheid_et_al-1998-Zeitschrift_f-r_anorganische_und_allgemeine_Chemie.pdf>. *Z. anorg. allg. Chem.* 1998, 624, 807.
130. Krautscheid, H.; Lode, C.; Vielsack, F.; Vollmer, H., Synthesis and crystal structures of iodoplumbate chains, ribbons and rods with new structural types. *Journal of the Chemical Society, Dalton Transactions* 2001, 1099-1104.
131. Billing, D. G.; Lemmerer, A., Synthesis, characterization and phase transitions of the inorganic–organic layered perovskite-type hybrids [(CnH2n+1NH3)2PbI4] (n = 12, 14, 16 and 18). *New Journal of Chemistry* 2008, 32, 1736.
132. Mishra, S.; Jeanneau, E.; Daniele, S.; Ledoux, G.; Swamy, P. N., <ic8010376(1).pdf>. *Inorg. Chem.* 2008, 47, 9333.
133. Lemmerer, A.; Billing, D. G., Effect of heteroatoms in the inorganic–organic layered perovskite-type hybrids [(ZCnH2nNH3)2PbI4], n = 2, 3, 4, 5, 6; Z = OH, Br and I; and [(H3NC2H4S2C2H4NH3)PbI4]. *CrystEngComm* 2010, 12, 1290-1301.
134. Mishra, S.; Jeanneau, E.; Iasco, O.; Ledoux, G.; Luneau, D.; Daniele, S., Heterometallic, Hybrid, Heavy Main-Group Iodometallates Containing Lanthanide Complexes: Template Synthesis, Structures, Thermal, Optical, Luminescent and Magnetic Properties. *European Journal of Inorganic Chemistry* 2012, 2012, 2749-2758.
135. Wakamiya, A.; Endo, M.; Sasamori, T.; Tokitoh, N.; Ogomi, Y.; Hayase, S.; Murata, Y., Reproducible Fabrication of Efficient Perovskite-based Solar Cells: X-ray Crystallographic Studies on the Formation of CH3NH3PbI3Layers. *Chemistry Letters* 2014, 43, 711-713.
136. Liu, Y.; Yang, Z.; Cui, D.; Ren, X.; Sun, J.; Liu, X.; Zhang, J.; Wei, Q.; Fan, H.; Yu, F.; Zhang, X.; Zhao,

C.; Liu, S. F., Two-Inch-Sized Perovskite CH3 NH3 PbX3 (X = Cl, Br, I) Crystals: Growth and Characterization. *Advanced materials* 2015, 27, 5176-83.
137. Xiao, Z.; Dong, Q.; Bi, C.; Shao, Y.; Yuan, Y.; Huang, J., Solvent annealing of perovskite-induced crystal growth for photovoltaic-device efficiency enhancement. *Advanced materials* 2014, 26, 6503-9.
138. Ahn, N.; Son, D. Y.; Jang, I. H.; Kang, S. M.; Choi, M.; Park, N. G., Highly Reproducible Perovskite Solar Cells with Average Efficiency of 18.3% and Best Efficiency of 19.7% Fabricated via Lewis Base Adduct of Lead(II) Iodide. *Journal of the American Chemical Society* 2015, 137, 8696-9.
139. Mosconi, E.; Quarti, C.; Ivanovska, T.; Ruani, G.; De Angelis, F., Structural and electronic properties of organo-halide lead perovskites: a combined IR-spectroscopy and ab initio molecular dynamics investigation. *Physical chemistry chemical physics : PCCP* 2014, 16, 16137-44.
140. Quarti, C.; Grancini, G.; Mosconi, E.; Bruno, P.; Ball, J. M.; Lee, M. M.; Snaith, H. J.; Petrozza, A.; Angelis, F. D., The Raman Spectrum of the CH3NH3PbI3 Hybrid Perovskite: Interplay of Theory and Experiment. *The journal of physical chemistry letters* 2014, 5, 279-84.
141. Singh, R. K.; Kumar, R.; Singh, J., Effect of precursors ratio on crystallinity and thermal stability of CH3NH3PbI3. 2017, 1832, 050056.
142. Ng, A.; Ren, Z.; Hu, H.; Fong, P. W. K.; Shen, Q.; Cheung, S. H.; Qin, P.; Lee, J. W.; Djurisic, A. B.; So, S. K.; Li, G.; Yang, Y.; Surya, C., A Cryogenic Process for Antisolvent-Free High-Performance Perovskite Solar Cells. *Advanced materials* 2018, 30, e1804402.
143. Glaser, T.; Muller, C.; Sendner, M.; Krekeler, C.; Semonin, O. E.; Hull, T. D.; Yaffe, O.; Owen, J. S.; Kowalsky, W.; Pucci, A.; Lovrincic, R., Infrared Spectroscopic Study of Vibrational Modes in Methylammonium Lead Halide Perovskites. *The journal of physical chemistry letters* 2015, 6, 2913-8.
144. Zhang, T.; Yang, M.; Benson, E. E.; Li, Z.; van de Lagemaat, J.; Luther, J. M.; Yan, Y.; Zhu, K.; Zhao, Y., A facile solvothermal growth of single crystal mixed halide perovskite CH3NH3Pb(Br(1-x)Cl(x))3. *Chemical communications* 2015, 51, 7820-3.
145. Li, Y.; Zhao, Z.; Lin, F.; Cao, X.; Cui, X.; Wei, J., In Situ Observation of Crystallization of Methylammonium Lead Iodide Perovskite from Microdroplets. *Small* 2017, 13.
146. Sim, L. N.; Sentanin, F. C.; Pawlicka, A.; Yahya, R.; Arof, A. K., Development of polyacrylonitrile-based polymer electrolytes incorporated with lithium bis(trifluoromethane)sulfonimide for application in electrochromic device. *Electrochimica Acta* 2017, 229, 22-30.
147. Zhao, L.; Luo, D.; Wu, J.; Hu, Q.; Zhang, W.; Chen, K.; Liu, T.; Liu, Y.; Zhang, Y.; Liu, F.; Russell, T. P.; Snaith, H. J.; Zhu, R.; Gong, Q., High-Performance Inverted Planar Heterojunction Perovskite Solar Cells Based on Lead Acetate Precursor with Efficiency Exceeding 18%. *Advanced Functional Materials* 2016, 26, 3508-3514.
148. Forgács, D.; Sessolo, M.; Bolink, H. J., Lead acetate precursor based p-i-n perovskite solar cells with enhanced reproducibility and low hysteresis. *J. Mater. Chem. A* 2015, 3, 14121-14125.
149. Zhang, W.; Saliba, M.; Moore, D. T.; Pathak, S. K.; Horantner, M. T.; Stergiopoulos, T.; Stranks, S. D.; Eperon, G. E.; Alexander-Webber, J. A.; Abate, A.; Sadhanala, A.; Yao, S.; Chen, Y.; Friend, R. H.; Estroff, L. A.; Wiesner, U.; Snaith, H. J., Ultrasmooth organic-inorganic perovskite thin-film formation and crystallization for efficient planar heterojunction solar cells. *Nature communications* 2015, 6, 6142.
150. Li, M.; Zhang, R.; Guo, Y.; Huan, Y.; Xi, J.; Li, Y.; Bai, Z.; Yan, X., Introducing lead acetate into stoichiometric perovskite lewis acid-base precursor for improved solar cell photovoltaic performance. *J. Alloys Compd.* 2018, 767, 829-837.
151. Zhou, X.; Zhang, Y.; Kong, W.; Hu, M.; Zhang, L.; Liu, C.; Li, X.; Pan, C.; Yu, G.; Cheng, C.; Xu, B.,

Crystallization manipulation and morphology evolution for highly efficient perovskite solar cell fabrication via hydration water induced intermediate phase formation under heat assisted spin-coating. *Journal of Materials Chemistry A* 2018, 6, 3012-3021.
152. Liu, Y.; Liu, Z.; Lee, E.-C., Dimethyl-sulfoxide-assisted improvement in the crystallization of lead-acetate-based perovskites for high-performance solar cells. *Journal of Materials Chemistry C* 2018, 6, 6705-6713.
153. Niu, G.; Li, W.; Meng, F.; Wang, L.; Dong, H.; Qiu, Y., Study on the stability of CH3NH3PbI3films and the effect of post-modification by aluminum oxide in all-solid-state hybrid solar cells. *J. Mater. Chem. A* 2014, 2, 705-710.